Finanziato dall'Unione europea NextGenerationEU
Ministero dell'Università e della Ricerca
Italiadomani PIANO NAZIONALE DI RIPRESA E RESILIENZA
UNIVERSITÀ DEGLI STUDI DI BARI ALDO MORO

UNIVERSITÁ DEGLI STUDI DI BARI ALDO MORO

Dipartimento di Farmacia - Scienze del Farmaco

DOTTORATO DI RICERCA IN SCIENZE DEL FARMACO

CICLO XXXVIII

Settore scientifico disciplinare: CHEM-07/A

Allosteric site mapping of human caseinolytic protease P (*h*ClpP): a strategy for the development of piperazines as drug candidates to treat the pediatric diffuse intrinsic pontine glioma.

Dottorando:
Dott. Domenico Armenise

Coordinatore:
Ch.mo Prof. Renzo Luisi

Supervisore (Tutor):
Ch.mo Prof. Antonio Scilimati

Co-Supervisore (Co-tutor):
Chiar.ma Prof.ssa Maria Grazia Perrone
Co-Supervisore (Co-tutor):
Dr. Carmine Talarico

ESAME FINALE 2026

CONTENT

Abbreviation

ACVR1	Activin A Receptor, Type I
ADEPs	Acyldepsipeptides
AML	Acute Myeloid Leukemia
ATF4	Activating Transcription Factor 4
BBB	Blood-Brain Barrier
bFGF	Basic Fibroblast Growth Factor
BSGs	Paediatric Brain Stem Gliomas
CAR-T	Chimeric Antigen Receptor T
CED	Convection-Enhanced Delivery
CETSA	Cellular Thermal Shift Assay
CHOP C/EBP	C/EBP Homologous Protein
CNS	Central Nervous System
DCFH-DA	Dichloro-Dihydro-Fluorescein Diacetate
DIPG	Diffuse Intrinsic Pontine Glioma
DISC	Death-Inducing Signaling Complex
EGFR	Epidermal Growth Factor Receptor
ELOVLs	Very-Long-Chain Fatty Acids Elongase
EMT	Epithelial-Mesenchymal Transition
FDA	Food And Drug Administration
FOX	Forkhead Box
FUS	Focused Ultrasound
GPDH	Glycerol Phosphate Dehydrogenase
HCC	Hepatocellular Carcinoma
*h*ClpP	Human Mitochondrial Protease
HDAC	Histone Deacetylase
h-GG	High-Grade Glioma
HIFU	High-Intensity Focused Ultrasound
ISR	Integrated Stress Response
LIFU	Low-Intensity Focused Ultrasound
LUSC	Lung Squamous Cell Carcinoma

MGMT	O-6-Methylguanine-DNA Methyl-Transferase
MMF	Mycophenolate Mofetil
MRgFUS	Magnetic Resonance-Guided Focused Ultrasound
MRPs	Mitoribosomes Proteins
MUFAs	Monounsaturated Fatty Acids
NASH	Non-Alcoholic Steatohepatitis
NDUFA12	NADH-Ubiquinone Oxidoreductase 1 Alpha Subcomplex 12
NFE2	Nuclear Factor Erythroid 2
NSCLC	Non-Small Cell Lung Cancer
OPCs	Oligodendroglial Progenitor Cells
OXPHOS	Oxidative Phosphorylation
PCR2	Polycomb Repressive Complex 2
PDAC	Pancreatic Ductal Adenocarcinoma
PDGFA	Platelet-Derived Growth Factor A
PDGF-A	Platelet-Derived Growth Factor A
PDGFRβ	Platelet-Derived Growth Factor Receptor B
PDGFα	Platelet-Derived Growth Factor A
PDT-O	Patient-Derived Tumor Organoids
PI3K	Phosphatidylinositol 3 Kinase
PKA	Protein Kinase A
PUFAs	Polyunsaturated Fatty Acids
ROS	Reactive Oxygen Species
RT	Radiotherapy
SCLC	Small Cell Lung Cancer
SFAs	Saturated Fatty Acids
THPPD	Tetrahydropyridopyrimidinone
TRAIL	Tumor-Necrosis Factor-Related Apoptosis-Inducing Ligand Stimulation
VEGF	Vascular Endothelial Growth Factor
WHO	World Health Organization

Abstract

Diffuse intrinsic pontine glioma (DIPG) is one of the most aggressive paediatric tumors of the central nervous system (CNS), characterized by a median survival of less than 12 months and the absence of therapeutic options. Of particular interest is **ONC201**, a compound belonging to the chemical class of imipridone, which has demonstrated clinical activity mediated by the selective activation of human mitochondrial protease (*h*ClpP). Structural analysis of the *h*ClpP:ONC201 complex and other known allosteric activators performed by X-ray crystallography provided key information for the rational optimization of the chemical structure of ONC201. Based on this evidences, in this PhD work, as a result of a significant simplification of the chemical structure of ONC201, a piperazine scaffold was identified. Furthermore, through an in-depth study of structure-activity relationships, the minimum requirements of the allosteric site of ClpP that ensure the increase of its proteolytic action were identified. The use of the piperazine nucleus and the rational design of the chemical structure of the molecules have allowed us to discover the piperazine-2-one scaffold (with an endocyclic carbonyl function) as the most promising. The multifunctional chemotype **26** (DA29) was therefore identified as the compound of greatest biopharmaceutical interest. The crystallographic structure of the *h*ClpP:26 (DA29) complex confirmed the initial hypotheses and highlighted a direct interaction with the hydrophobic pocket of the enzyme's apical allosteric domain, consistent with potent proteolytic activation. Compound **26** (DA29) causes significant thermal stabilization of ClpP in DIPG cell lines, as evidenced by CETSA analysis, suggesting a higher affinity for protease than **ONC201**. Permeability studies conducted under static and dynamic flow conditions demonstrated the compound ability to cross an *in vitro* model of the blood-brain barrier, suggesting potential penetration in the central nervous system. From a mechanistic point of view, **26** (DA29) induces the activation of *h*ClpP, the dissociation of the *h*ClpXP complex, formed by ClpP and AAA+ ATPase unfoldase/chaperone (ClpX), mitochondrial dysfunction, accumulation of reactive oxygen species (ROS), alterations in the lipid profile and

cytotoxicity in patient-derived DIPG cells, with validation extended to DIPG tumor organoids derived from patients with a view to personalized medicine. Unlike **ONC201**, **26** (DA29) shows no interaction with D2/D3 dopaminergic receptors, suggesting a selectively *h*ClpP-mediated mechanism of action. Overall, these findings define a new model for the development of *h*ClpP activators and represent a significant advance toward the realization of targeted and rational therapeutic strategies for the treatment of DIPG. A preclinical *in vivo* study of **26** (DA29) is currently underway in an orthotopic *in vivo* model of DIPG.

Chapter 1. Introduction

1.1. Diffuse Intrinsic Pontine Glioma (DIPG)

Diffuse intrinsic pontine glioma (DIPG) is a paediatric tumor classified by the World Health Organization as a high-grade glioma (h-GG) and belongs to the category of diffuse midline gliomas (DMG)[1]. It is a particularly aggressive form of tumor that originates from glial cells, whose physiological function is to provide support and protection to the brain neural network. The area involved is the pons (Figure 1), an anatomical region crucial for controlling various vital functions, including heartbeat, breathing, and eye movement, which makes its treatment very complex[2]. DIPG also represents 80% of paediatric brainstem tumors and approximately 10-20% of all paediatric brain tumors[3,4]. It affects children in two age groups, 0-4 years and 5-9 years, with girls having a worse prognosis than boys with DMG[5]. 150-400 new cases per year are reported in the United States and a similar percentage in Europe[6], with typical symptoms such as cranial nerve palsy, ataxia, and pyramidal tract abnormalities. In Italy, there are 22-25 new diagnosis per year.

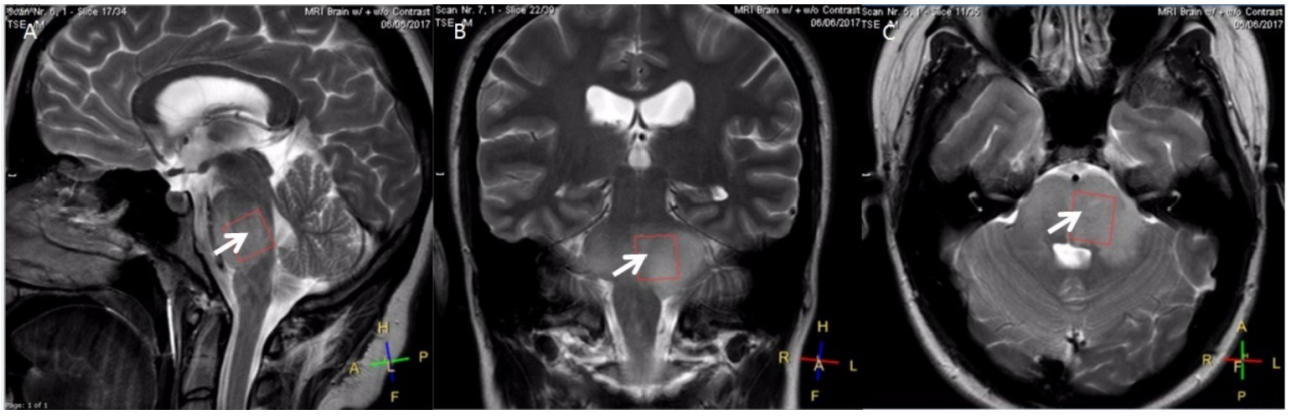

Figure 1. T2-weighted resonance of three sections: sagittal (A), coronal (B), and axial (C) in which the white arrow highlights a diffuse intrinsic hyperintense lesion of the brainstem[7].

Due to the anatomical location of the tumor, DIPG patients present a variety of neurological symptoms. About 50% of patients show cranial nerve palsy (facial asymmetry and diplopia), long

tract signs (i.e., increased tone, hyperreflexia, clonus, Babinski's sign, motor deficit) and cerebellar signs (ataxia, dysmetria, dysarthria)[8,9]. These three manifestations constitute the "classical triad". Cranial nerves VI and VII are the most commonly affected; their dysfunction is characteristic of DIPG since these nerves originate where the tumor usually infiltrates[10]. This event leads to diplopia and conjugate gaze paralysis (abducens palsy) which is a common initial sign and index of poor prognosis[11]. Since the DIPG progression is very rapid, children generally manifest symptoms less than a month before diagnosis[12]. At the time of diagnosis, increased intracranial pressure is observed in less than 10% of patients. This condition is caused by obstructive hydrocephalus, which in turn results from the expansion of the pons. This increased intracranial pressure, however, can be observed in patients in the terminal stage of the disease[13]. Other non-specific symptoms are present both at the time of diagnosis and/or in the disease progression and include sensory abnormalities, behavioural changes, urinary problems, decreased school performance, and respiratory symptoms including sleep apnea[14].The aggressive nature of this tumor, together with its location, means that, to date, the only treatment available is fractionated focal radiotherapy (59 Gray), which, however, has only a partial and temporary effect on symptoms. In fact, the survival rate of 12 months after diagnosis is around 5%. All this has led to increasing attention being paid to DIPG, thanks in part to advances in surgical techniques and genetic and molecular analysis, although there are still no clinical studies that have had a major impact on survival[2,5,15].

1.1.2. H3K27-altered and epigenetic implications in DIPG

One of the main problems related to the study of this paediatric disease is the limited amount of tumor tissue available for genomic analysis. However, thanks to advanced surgical techniques, it became possible to perform biopsies more easily, leading to a significant increase in the molecular information derived from such tissues. Histones represent the fundamental chromatin component.

They associate with DNA to form a structural unit called the nucleosome. These analyses show that approximately 80% of DIPG tumors have an H3K27M mutation, along with other concomitant mutations, and this alteration has been shown to modify the biological and clinical profile of the disease so significantly that it will be reclassified in 2021 by the WHO as "H3K27-altered." This alteration is particularly relevant as it affects the proliferation and spread of cancer cells and, specifically, is a missense mutation of lysine at position 27 with a methionine (K27M) at the level of the genes encoding the two histone isoforms H3.3 and H3.1. This results in abnormal transcription, which induces a structural alteration of histone proteins, compromising their ability to interact with DNA and other proteins. The H3K27M mutation occurs at the H3FA locus, which encodes only the H3.3 isoform, but despite this, approximately 20% of pontine glioma cases have the mutated H3.1 and H3.2 variants at the gene called HIST1H3B[16–20]. The two isoforms H3.1 and H3.3 have different clinical-pathological and radiological features, as the former manifests earlier with a slightly longer survival rate than the other isoform. To date, it is not known when these genetic mutations first occur, but it is thought that they occur during the embryonic development of the brain, as *in silico* studies using RNA-seq analysis have identified the activity of approximately 17 genes encoding H3 histone proteins during this phase[21]. These proteins have different expression patterns. The H3.3 isoform plays a predominant role in the early stages of brain development, as H3F3A, the gene encoding this histone variant, shows a reduction in activity as neuronal maturation progresses. In contrast, the gene encoding the H3.1 variant, HIST1H3B, appears to be almost completely 'inactive' in the mature brain following a rapid decrease in initial activity. These different characteristics explain how mutations of different origins have a variable effect and how they manifest themselves at different ages, making this pathology particularly dynamic[21–23]. In addition to their different dynamics, the two isoforms also have molecular differences that emerged from a sequencing analysis of 25 post-mortem DIPG tumor tissue samples, including 16 H3.3-mutated and 9 H3.1-mutated samples, and 5 rare paediatric pontine tissue samples[24]. H3.1 tissues predominantly exhibit characteristics related to Nuclear Factor Erythroid 2 (NFE2) signalling,

which is involved in all processes that regulate tumor cell resistance to therapy[25]. In contrast, H3.3 tissues show an enrichment of transcription factors associated with early neuronal development, in particular those factors that have a primary effect on the construction of midline brain structures[26]. Histone variants also show distinct localization patterns compared to their canonical forms, with important consequences for the regulation of gene expression in pathology. H3.3 is predominantly associated with transcriptionally active chromatin regions, where it participates in the dynamic modulation of gene expression levels. In contrast, H3.1 has a more uniform distribution across the entire genome, suggesting a more global influence on the regulatory mechanisms of gene expression[27]. Along with this main mutation, there are also several important secondary concomitant mutations involving the TP53 tumor suppressor gene pathway and phosphatidylinositol 3 kinase (PI3K), which regulate cell growth and division, as well as mutations in genes associated with the ACVR1 signalling pathway, which encodes a receptor involved in cell signaling[16,17,19,20].

1.1.3. Epigenetic remodelling and cellular vulnerability in DIPG pathogenesis

The malignancy of this tumor is closely associated with epigenetic dysregulation, and one of the most significant, due to the H3K27M mutation, is the marked reduction in H3K27me3 levels, a post-translational modification of histones that affects gene regulation, involving marked trimethylation of lysine 27 of histone H3. The overall loss of H3K27me3 has been attributed mainly to the functional inhibition of Polycomb Repressive Complex 2 (PCR2) (Figure 2)[28–30], which, in the context of epigenetic regulation, causes the activation and repression of genes without modifying the DNA sequence. Specifically, in DIPG, the impairment of epigenetic mechanisms promotes the aberrant activation of transcriptional programs associated with cell proliferation, differentiation, and migration, which contributes significantly to tumorigenesis[31–33]. However, in a subgroup of tumors, the loss of H3K27me3 occurs in the absence of histone mutations and is mediated by the

overexpression of EZHIP, a functional inhibitor of the PRC2 complex, which compromises the methyl transferase activity of EZH1/2[34]. One of the biological processes affected by H3K27me3 is epithelial-mesenchymal transition (EMT), a process that is essential in early embryonic development and is involved in gastrulation, neural crest cell migration, and neural tube formation, processes that are essential for the correct organization of the CNS[35–37]. Gene expression studies[38], based on RNA-seq have shown that DIPG with the H3K27M mutation have a significant enrichment of genes associated with EMT than non-mutated tumor forms. In particular, the most highly expressed genes are those characteristics of the early stages of EMT compared to those associated with the late stages, in addition to the presence, once again, of differences between the two histone variants. The H3.1 isoform appears to be related to a more advanced stage of EMT than those with the H3.3 mutation.

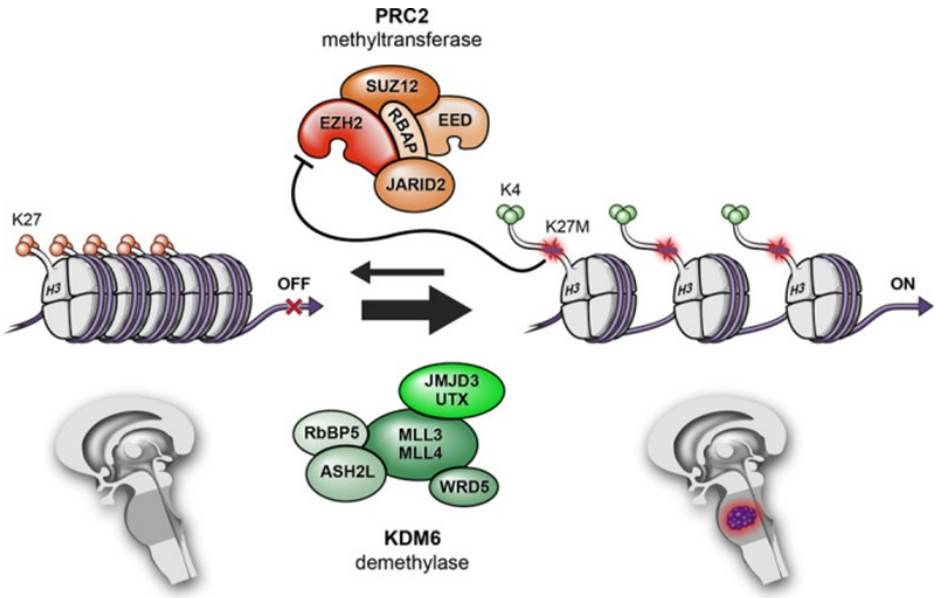

Figure 2. Histone modifications by PRC2 methyltransferase and KDM demethylase activities. H3K27M binds PRC2 with high affinity. The K27M mutation blocks methylation by PRC2 on K27 of the mutant histone tail and sequesters PRC2, reducing global levels of K27me 3 within cells. This model is based on the assumption that PRC2 levels are restricted[39].

Another important aspect of this pathology concerns the cellular origin of DIPG, which, based on experimental evidence, appears to be associated with a population of susceptible cells, influenced by both genetic alterations and the local microenvironment. In particular, the cells of origin of the tumor appear to be oligodendroglial progenitor cells (OPCs), responsible to produce myelin, which are abundant in the brainstem during childhood and adolescence, a period of intense myelination. Proliferation and survival depend on the signal from platelet-derived growth factor A (PDGF-A) and its receptor (PDGFRA), which is essential for the maintenance of OPC cells but inhibits their terminal differentiation, as PDGFRA signalling decreases as OPCs progress toward maturation into myelinating oligodendrocytes (OL)[40]. However, PDGFRA is subject to various genetic amplifications or mutations observed in different forms of DMG that contribute to the alteration of these processes, although the molecular mechanisms are not fully understood[17]. Using mouse models, it has been shown that prenatal overexpression of human PDGFRA compromises oligodendroglial development and induces hypomyelination, and subsequent studies have confirmed a time-space correlation between the proliferation of Olig2-expressing precursor cells in the brainstem and the development of paediatric gliomas. Therefore, through experimental models, it has been possible to induce DMG in two distinct populations of brain progenitor cells expressing Olig2 and Nestin. However, the introduction of the H3.3 mutation produced different effects depending on the cellular context: in Nestin-positive cells, it significantly accelerated tumor progression, while in Olig2-positive cells, its effect was more limited, emphasizing that the oncogenic effect of H3K27M is strictly dependent on the type of cells of origin[38].

In-depth analysis of the gene mutations that code for histone H3 variants, specifically the H3K27M mutation, has been fundamental to understanding the development of DIPG. This disease presents considerable clinical and molecular diversity, also characterized by various secondary mutations, highlighting the complex molecular picture of tumorigenesis.

1.1.4. Effects of radiation therapy on genetic processes

Despite major progress in drug therapies, radiotherapy remains essential in multifocal treatment and is, in effect, the only successful therapeutic approach. Precisely, due to the failure of most therapies, there is a need to analyse the gene expression patterns of brain tumors and, above all, to observe in detail how the genetic profile changes after radiotherapy[15]. This could be a key element in identifying critical genes and pathways involved in the main signalling mechanisms, DNA repair mechanisms, and cell cycle regulation in response to irradiation, with a view to developing personalized therapeutic strategies, including in response to resistance to certain drugs[41,42]. Several gene expression studies have been conducted on various tumour types, such as medulloblastoma and glioblastoma, leading to the identification of the ASPM gene as a potential molecular target due to its overexpression[43]. In medulloblastoma, this analysis has allowed the classification of four molecular subsets, each characterized by the involvement of specific signalling pathways related to neuronal development, metabolism, and tumor proliferation regulation[44]. In the genetic picture of midline gliomas (DMG), the partial loss of trimethylation of lysine 27 of histone H3 (H3K27me3) is one of the main molecular features of these tumors, leading to extensive transcriptional activation with overexpression of genes involved in tumorigenesis and cell metabolism. Early analyses of the impact of radiotherapy on gene expression profiles in brain tumors[45], revealed significant alterations, especially in recurrent tumors, as transcriptomic analyses performed on post-radiotherapy recurrent malignant glioma tissues showed significant differences compared to untreated tumors. The reduction in the expression of paracrine mediators such as Vascular Endothelial Growth Factor (VEGF) and Platelet-Derived Growth Factor Receptor β (PDGFRβ), and autocrine mediators such as Epidermal Growth Factor Receptor (EGFR), Platelet-Derived Growth Factor α (PDGFα), Platelet-Derived Growth Factor A (PDGFA), and Basic Fibroblast Growth Factor (bFGF), suggests that radiation-induced selective pressure causes a remodelling of tumor interactions, with effects on cell survival, proliferation, and the tumor microenvironment in general.

Further studies have investigated the molecular mechanisms underlying the adaptation of gliomas to irradiation, identifying five gene signatures (HOXC10, LOC101928747, CYB561D2, RPL36A, and RPS4XP2) associated with treatment response and prognosis[46]. Many experimental and clinical models have shown that radiotherapy is associated with the activation of inflammatory and immune pathways such as those of Chemokine and IL-6[47], as well as the significant presence of epigenetic changes able to modulate gene transcription, including Polycomb complex regulatory genes and oncogenes (Figure 2) that have been identified during tumor progression[48]. A central role in therapeutic response is played by the O-6-methylguanine-DNA methyl-transferase (MGMT) gene[49], which is involved in DNA repair mechanisms. In patients with glioblastoma, low levels of MGMT expression lead to a significant reduction in tumor size and, together with MGMT promoter methylation, are associated with a better response to treatment and a more favorable prognosis[50,51], regardless of concomitant use of temozolomide[52]. Conversely, its high expression in DMG patients with H3K27M alteration contributes to therapeutic resistance and may explain the limited benefit of pharmacological treatment with temozolomide in DIPG[49].

1.1.5. New therapeutic approaches for the treatment of DIPG/DMG

Over the past two decades, several studies have contributed to clarify the molecular picture of paediatric brain stem gliomas (BSGs). Among the first relevant findings is the identification of ERBB1 amplification and overexpression in high-grade tumors, in association with TP53 mutations independent of grade[53], determining the ERBB1 signal as a potential therapeutic target. In addition, significant expression of the mutated EGFRvIII variant has been detected in paediatric DMG, reinforcing the hypothesis of EGFR as a further potential therapeutic target[54].

Another frequent alteration in DMG is somatic mutations of ACVR1[55]. Although the use of ALK2 inhibitors has demonstrated antitumor activity in experimental models, their use as monotherapy is

not sufficient. Innovative approaches have instead identified promising therapeutic combinations, such as vandetanib, which targets ACVR1 by inhibiting VEGFR/RET/EGFR, and everolimus (Figure 3), an mTOR/ABC transporter inhibitor, capable of reducing cell viability and tumor burden in xenograft models, highlighting the importance of combination therapies[56]. The importance of molecular profiling has been further confirmed by clinical studies that have shown an increase in overall survival in a study conducted on DMG patients using targeted therapy involving nimotuzumab/vinorelbine[57] or temozolamide (Figure 3) combined with radiotherapy using specific drugs selected based on the molecular profile of the tumor. Among the various treatments, everolimus emerges as one of the drugs associated with the most favorable outcomes[58]. Subsequently, studies were conducted on therapeutic agents capable of reversing the gene signature of DMG, making it more similar to that of healthy tissue, from which two drugs emerged, triptolide and mycophenolate mofetil (MMF) (Figure 3), capable of inhibiting cell viability and tumor growth *in vivo*[59]. Along with molecular therapies, immunotherapy is a constantly evolving field, and in particular, the use of anti-GD2 Chimeric Antigen Receptor T cells (CAR-T cells) has emerged for neuroblastoma and glioma[60]. CAR-T cells engineered to recognize disialoganglioside GD2, belonging to the type b ganglioside family, have demonstrated great efficacy and persistence over time, as well as the ability to cross the BBB. There are currently several clinical trials in paediatric and adult patients with h-GGs expressing GD2, with encouraging preliminary results[61,62].

In the field of targeted therapies for DMGs, the state of the art in clinical trials shows that approximately 250 clinical studies[63] have been initiated on various biological targets involved in tumor pathogenesis. Among these, PDGFRA and EGFR are the most amplified genes within these pathways; however, treatments targeting PDGFRA, with imatinib (Figure 3) and desatinib, have limited clinical efficacy[64]. On the other hand, studies based on EGFR inhibition mediated by nimotuzumab, gefitinib, and erlotinib have demonstrated positive therapeutic effects in certain subgroups of patients with DMG[65–67]. JMJD3 inhibitors, panobinostat (Figure 3) and GSK-4, acting

on histone deacetylase and demethylase, have shown promising results[68,69], as well as chromatin remodeling agents, such as EZH2 in combination with tazemetostat (Figure 3)[70].

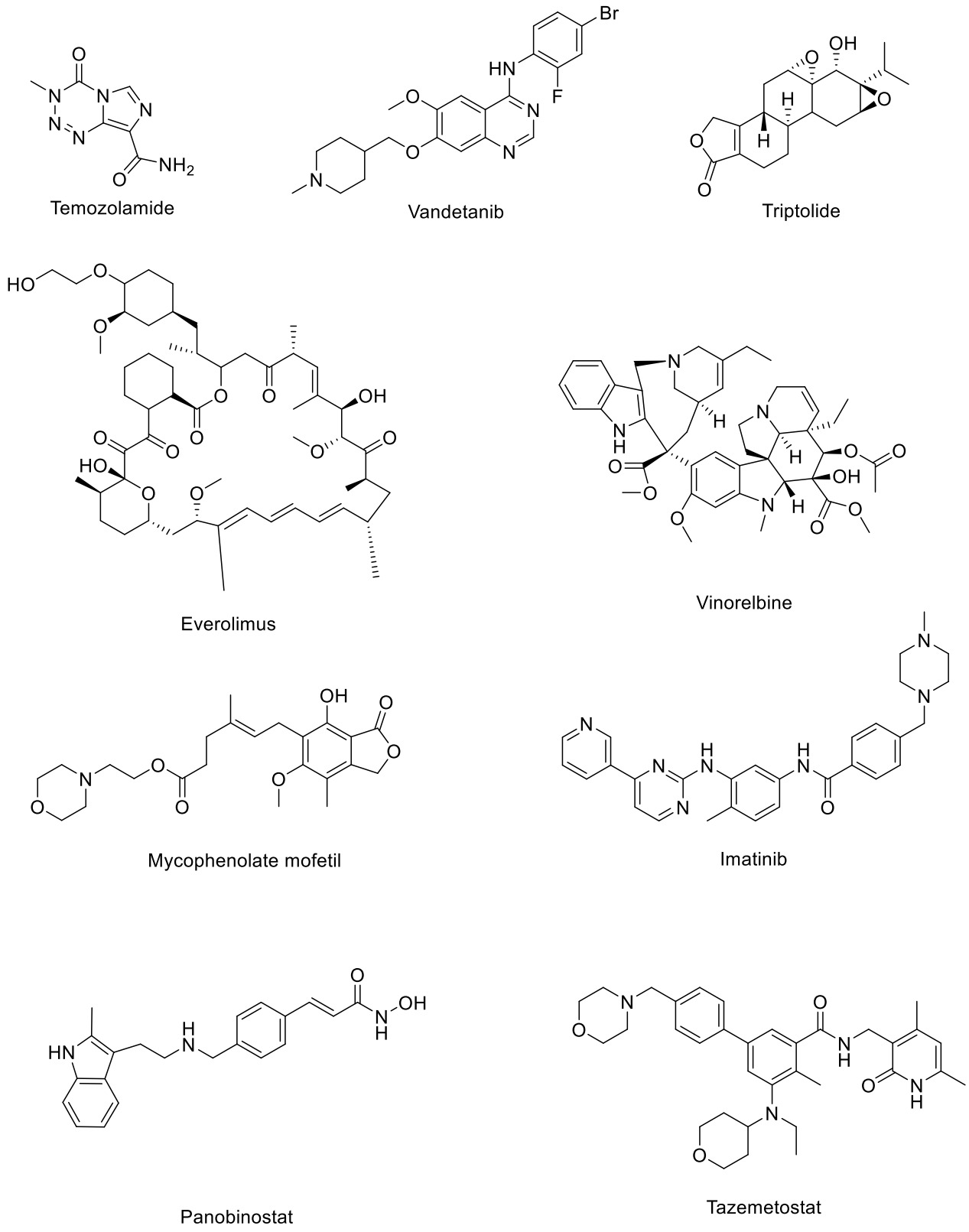

Figure 3. Chemical structure of some drugs for new therapeutic approaches for treatment of DMG.

1.1.6. Focused ultrasound as a strategy for blood-brain barrier crossing

Use of radiotherapy in paediatric patients, however, is particularly delicate since CNS is still developing and is particularly sensitive to long-term side effects. Chemotherapy has also contributed significantly to therapeutic advances, but its effectiveness is still limited by the blood-brain barrier (BBB) integrity, which is the primary obstacle to drug distribution in CNS[71]. In fact, crossing BBB is related to specific chemical-physical characteristics of compounds summarized by Lipinski's rules (low molecular weight, appropriate lipophilicity, and limited interaction with plasma proteins). Overall, only 2% of lipophilic small molecules are able to permeate BBB, while most small molecules and certainly macromolecules, peptides, recombinant proteins, and monoclonal antibodies do not cross the barrier[72,73]. To overcome these limitations, several strategies have been developed with the aim of improving CNS accessibility. BBB is the primary protection system of the brain and, at the same time, is a dynamic and highly selective physiological barrier that ensures the maintenance of homeostasis in the neuronal microenvironment. It regulates the bidirectional flow of neuroactive substances between the systemic circulation and the CNS, preventing the entry of toxic compounds while ensuring the delivery of essential nutrients to brain tissues[74]. These molecules pass through BBB *via* various mechanisms, including active paracellular transport, passive diffusion, carrier-mediated transport, and adsorptive or receptor-mediated transcytosis[75]. All these transport systems protect CNS from both potentially damaging endogenous substances and xenobiotics. In brain tumors, BBB is often intact or only partially altered, limiting access and, above all, the achievement of effective therapeutic concentrations of antineoplastic drugs. One strategy developed involves the local administration of drugs through stereotactic intracranial injection or the implantation of surgical reserve catheters. These approaches, known as convection-enhanced delivery (CED), allows the drug to be distributed directly into the tumor tissue through a pressure gradient, ensuring greater diffusion than passive diffusion. Due to catheterization, this system allows repeated administration of drugs through small-caliber needles, demonstrating efficacy and safety

even in prolonged treatments[76]. However, the use of catheters may be associated with infectious and non-infectious complications, such as obstructions and fluid loss[77,78], in addition to the possibility of neurological side effects, including mild or moderate headache, facial weakness, dysarthria, and ataxia, which reverse after cessation of infusion[79]. Due to the limitations of using such catheters, an innovative approach to facilitate drug treatment has been identified, namely focused ultrasound (FUS). This is an experimental technique, but it is beginning to show promising results. FUS has the ability to induce a temporary and safe opening of BBB, lasting approximately 24 hours, allowing effective delivery of drugs directly to the tumor tissue[80]. In recent decades, significant progress has been made in the clinical applications of FUS, thanks to its integration with magnetic resonance imaging and ultrasound techniques that allow for accurate targeting and monitoring of treatment[81]. In the clinical setting, high-intensity focused ultrasound (HIFU) or low-intensity focused ultrasound (LIFU) can be used. The HIFU wave is characterized by a very concentrated focus, with a diameter of about 1 mm and a depth of about 10 mm, which allows for precise localization of thermal effects. At the point of focus, the temperature can exceed 60 °C for a few seconds, causing irreversible cell death without damaging the surrounding tissues, where the energy density is significantly lower. This high precision makes HIFU particularly interesting for ultrasonic surgery applications[82]. In addition to LIFU, more recent research reports the use of even lower ultrasonic intensities for opening BBB, in combination with microbubbles (FUS/MB). Microbubbles were initially developed as imaging contrast agents and have a diameter between 1 and 10 μm, with a lipid or protein coating that encapsulates high molecular weight gas[83,84]. Once in the bloodstream, gas-filled microbubbles expand and contract under the effect of ultrasonic pressure waves (0.2–2 MHz), inducing a phenomenon known as cavitation. Cavitation generates mechanical forces on the endothelium within the focal area of the FUS, causing sonoporation of the plasma membrane, disruption of tight junctions, and, consequently, opening BBB (Figure 4)[85–87].

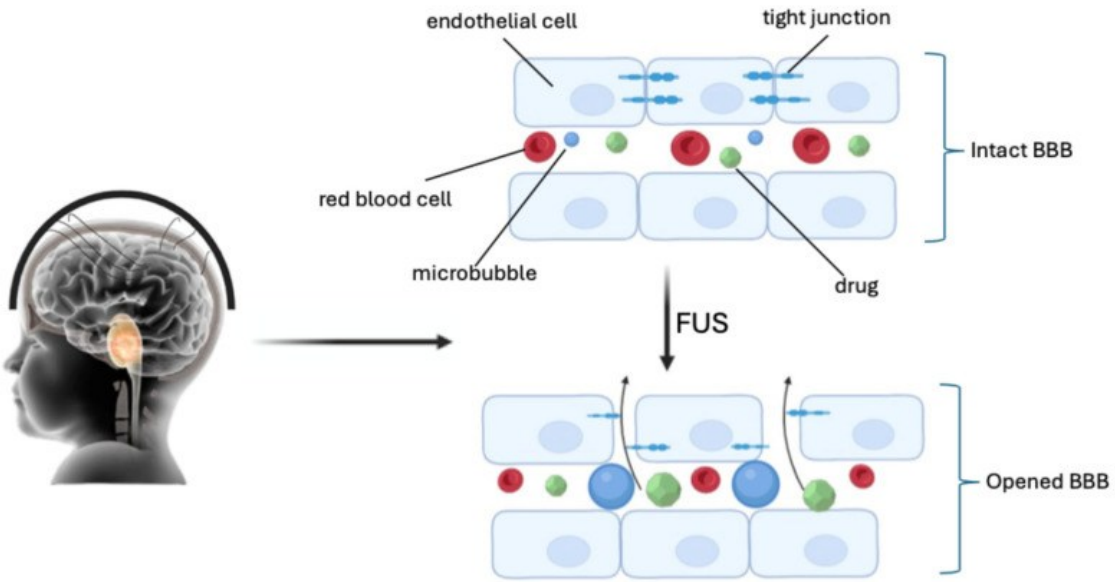

Figure 4. Sonoporation of plasma membrane, disruption of tight junctions, and BBB opening by FUS[88].

The combination of FUS and radiotherapy (RT), monitored by magnetic resonance imaging, confirmed the reversible opening of BBB, with complete recovery of the barrier integrity within 72 hours of ultrasound application. In terms of efficacy, combination of FUS and RT did not result in a survival advantage over RT alone[89,90].

For this reason, it is essential to combine this technique with the administration of chemotherapeutic agents such as doxorubicin, which has antitumor efficacy as well as a limited ability to cross BBB due to its structure and was chosen for its *in vitro* effect on different DIPG cell lines[91]. Studies conducted on mice have shown that the level of doxorubicin detected in the brainstem of animals treated with magnetic resonance-guided focused ultrasound (MRgFUS) were approximately 50 times higher than in untreated control, and the amount of drug in the target tissue remained high for approximately two hours after administration, despite the relatively short plasma and tissue half-life of free doxorubicin (Figure 5)[92].

Another study was conducted using panobinostat (Figure 3), which, as a histone deacetylase (HDAC) inhibitor, showed a cytotoxic effect in H3K27M cell lines both *in vitro* and in murine xenograft models. Although structurally is a small molecule, following administration it binds significantly to plasma proteins, resulting in an increase in its molecular weight, making it very difficult to cross BB. Low doses of panobinostat in combination with MR-guided FUS/MB were evaluated in a PDX mouse model of DIPG with H3K27 mutation and concomitant TP53 mutation. The study showed a significant increase in drug concentration in the tumor parenchyma of approximately three times compared to cerebral cortex.

The effect of olaparib (Figure 5), a PARP inhibitor (PARPi) already used as first-line treatment in several cancers, in combination with either RT or FUS/MB was also studied, and a 5.4-fold increase in the amount of olaparib in the pons was observed, based on blood/tissue ratio[93].

Finally, the FUS/**ONC201** combination resulted in a reduction in the expression of NADH-ubiquinone oxidoreductase 1 alpha subcomplex 12 (NDUFA12), an mitochondrial enzyme complex I and a biomarker of response to **ONC201**, and an increase in ROS production compared to the treatment with **ONC201** monotherapy[94]. In conclusion, FUS, and particularly LIFU (which is safer), may represent an effective and reliable strategy to overcome BBB blockade, facilitating drug delivery to the brain and opening new perspectives for the future treatment of DIPG.

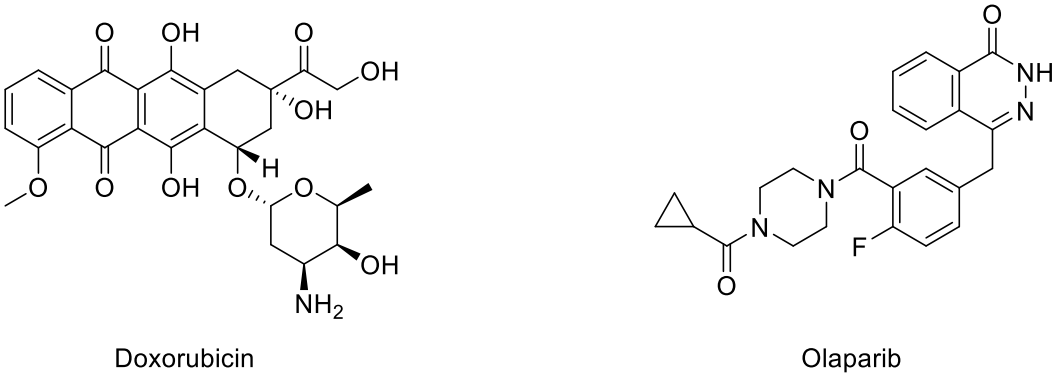

Doxorubicin Olaparib

Figure 5. Chemical structures of Doxorubicin and Olaparib studied in combination with FUS.

1.2. ONC201

By screening approximately 2,000 small molecules from the National Cancer Institute Chemical Library DIversity Set II, **ONC201**, formerly known as TIC10 (Figure 6), was identified as an inducer of p53-independent TRAIL-mediated apoptosis[95]. In August 2025, the FDA approved **ONC201**, under the name dordaviprone (Modeyso™), for recurrent H3K27M-mutant DMG, including DIPG, due in part to its ability to cross BBB, which is crucial given the location of the tumor. **ONC201** main mechanism of action is the stimulation of the production in tumor cells of Tumor-Necrosis Factor-Related Apoptosis-Inducing Ligand Stimulation (TRAIL)[96], which belongs to the TNF superfamily of cytokines[97].

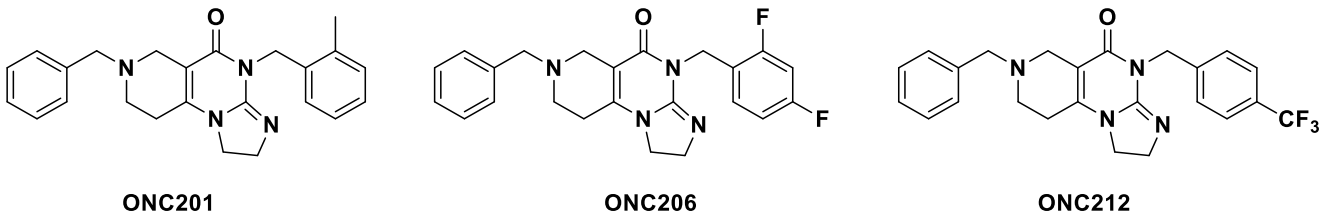

Figure 6. Chemical structure of **ONC201**, **ONC206** and **ONC212**.

The interaction of these cytokines with the complex receptor system, composed of five distinct receptors, triggers various mechanisms with pro-apoptotic or regulatory functions. Two of these receptors, DcR1 and DcR2, act as trap receptors, as the former lacks signalling capacity while the latter can bind TRAIL but does not have a cell death domain and is able to activate cell survival pathways, such as NF-kB, contributing to resistance to apoptosis. Dopaminergic receptor DR4 and DR5 are responsible for transducing the extrinsic apoptotic signal through the formation of the death-inducing signaling complex (DISC) which, by inducing the activation of caspase-8, activates the effector caspase cascade. This signalling pathway can be further amplified through the involvement of the intrinsic mitochondrial pathway mediated by the cleavage of the Bid protein, the

release of cytochrome c, and the activation of caspase-9, which ends with the activation of caspase-3, resulting in a cell death signal. The fifth receptor, osteoprotegerin, is a soluble protein that appears to exert an inhibitory function by sequestering TRAIL in the extracellular space[98]. The TRAIL system is an important therapeutic target for selectively inducing apoptosis in cancer cells, and **ONC201** has demonstrated significant antitumor activity, as it has been shown to arrest growth and induce apoptosis in several antitumor models with minimal effect on normal cells[99]. A key mechanism associated with this activity is the activation of the integrated stress response (ISR), which leads to the induction of transcription factors such as Activating Transcription Factor 4 (ATF4) and C/EBP homologous protein (CHOP), which together lead to an upregulation of the DR5 receptor, triggering marked apoptotic signaling[100]. However, the therapeutic effect of **ONC201** does not depend only on TRAIL induction, as in some forms of cancer, such as breast cancer, it significantly reduces cell viability[101] without raising TRAIL level and is also effective in TRAIL-resistant models and in various haematological malignancies[102,103]. The antitumor effect of **ONC201** has been associated with the inhibition of another signalling pathway, Akt/ERK, two oncogenic kinases that act on the regulation of the transcription factor FOXO3a, a known tumor suppressor[104,105]. Transcription factors belonging to the Forkhead box (FOX) family are a group of highly conserved factors consisting of a DNA-binding domain that is responsible for the specificity of interaction with target genes. These factors play an essential role in regulating cell proliferation, metabolism, stress response, and tumorigenesis. In mammals, there are four different isoforms (FOXO1, FOXO3a, FOXO4, and FOXO6), and their activity is regulated by the PI3K/Akt[106] signalling pathway. Among the different isoforms, FOXO3a is one of the most studied because it is involved in the transcriptional activation of genes associated with apoptosis, cell cycle regulation, and DNA damage response. The activity of this factor is modulated by several post-translational modifications, such as Akt-mediated phosphorylation, which promotes the translocation of FOXO3a from the nucleus to the cytoplasm, resulting in the inhibition of its transcriptional activity[107].

Similarly, phosphorylation by ERK leads to its ubiquitination and subsequent proteasomal degradation[108]. On the other hand, modifications such as deacetylation and methylation regulate the affinity of FOXO3a for DNA and its transcriptional activity. The inhibition of kinases and, therefore, the relative phosphorylation of FOXO3a prevents the cytoplasmic translocation of the factor, which remains at the nuclear level and inhibits the transcription of pro-apoptotic genes, including TRAIL. This represents one of the main molecular mechanisms through which **ONC201** promotes apoptosis in cancer cells, highlighting the essential role of FOXO3a in the integration of cell survival and death signals[109].

1.2.1. Dopaminergic antagonism of ONC201

TRAIL and Akt/ERK system certainly explain the pro-apoptotic effect of **ONC201**; however, **ONC201** is a selective antagonist of dopaminergic receptors, particularly DRD2 and DRD3 receptors. It binds *h*D2R and *h*D3R with Ki values of 14.8 ± 1.40 μM and 4.09 ± 0.69 μM^2. The implication of the dopaminergic system represents a possible therapeutic strategy since dopamine, in addition to being a known neurotransmitter that acts on the central and peripheral nervous systems, is involved in the modulation of various biological tumor processes, influencing neoplastic growth, cell survival, and response to antitumor treatments. Dopamine can promote tumorigenesis processes, primarily through its endogenous production, but also through the development of tumors whose microenvironment is rich in dopamine and through the functional expression of dopaminergic receptors by neoplastic cells. Some neoplasms originate directly from cells that physiologically synthesize catecholamines, such as pheochromocytomas, paragangliomas, and neuroblastomas, and consequently maintain the biosynthetic capacity to produce dopamine[110]. Paediatric neuroblastomas also frequently show a catecholaminergic profile dominated by dopamine, and these malignancies can independently produce dopamine and express dopaminergic receptors, creating an

autocrine/paracrine process that can contribute significantly to tumor survival. However, there are also tumors that do not produce dopamine autonomously but develop in anatomical areas characterized by a high physiological concentration of the neurotransmitter, as in various brain neoplasms. In particular, h-GGs, including glioblastoma and DIPG, can arise in regions with high dopaminergic innervation[111]. The dopamine released by surrounding neurons acts on the tumor through receptor mechanisms, specifically by activating D2-like receptors, specifically DRD2, belonging to the family of Gi/o protein-coupled receptors that negatively regulate adenylate cyclase activity, thereby reducing intracellular cAMP levels and protein kinase A (PKA) activity[112]. This activation leads to the cascade development of oncogenic pathways such as PI3K/Akt, NF-kB, and MAPK, resulting in increased expression of anti-apoptotic proteins and the development of treatment-resistant phenotypes[113]. DRD2 antagonism by imipridones disrupts Gi-coupled signalling cascades that suppress adenylate cyclase, resulting in increased intracellular cAMP and activation of protein kinase A (PKA). This destabilizes survival signalling networks and relieves the inhibition of pro-apoptotic pathways[114]. More importantly, DRD2 blockade activates the ISR *via* phosphorylation of eIF2α, leading to enhanced translation of ATF4 and CHOP. These transcription factors, in turn, induce a suite of pro-death genes, including the tumor necrosis factor-related apoptosis-inducing ligand receptor DR5, sensitizing tumor cells to extrinsic apoptosis. DRD2 antagonism also induces cancer cell death in preclinical models of h-GGs and other malignant malignancies[115,116].

However, based on more recent evidence **ONC201** antitumor activity can not be attributed only to dopaminergic antagonism, which still needs to be further proven. Indeed, in May 2019, the diffractometric characterization (X-ray) of the complex between human Caseinolytic Protease P (*h*ClpP), a mitochondrial serin-protease, and **ONC201** (PDBID: 6DL7) led to the identification of *h*ClpP as its true biological target[117,118].

1.3. Mitochondrial caseynolitic Protease P (ClpP)

1.3.1. Generality

ClpP is a serine protease forming with the AAA+ unfoldase protein (ClpX) the ClpXP complex, whose main function is to degrade damaged or misfolded proteins to prevent their accumulation, thus preventing disruption of normal cellular function. Given its mitochondrial localization, ClpP acts as an effector of the Mitochondrial Unfolded Protein Response (UPRmt), a system that, under conditions of oxidative and proteotoxic stress, intervenes to restore normal mitochondrial function by inducing the expression of chaperones, such as HSP60, HSP10, and mtHSP70, which ensure protein refolding, and proteases such as LONP and ClpP itself, which degrade irreparably damaged proteins[119]. Its fundamental characteristic is its structural dynamism under physiological conditions but especially in the presence of its allosteric activator, whose binding is strongly correlated with various conformational changes.

Structurally, the ClpXP protease complex consists of two ClpP heptamers that form a barrel-shaped tetradecamer, closed at both ends by ClpX hexamers (Figure 7). As such, the ClpP monomer has low peptidase specificity, as this specificity is attributed, at the intracellular level, to its bonding with the ClpX chaperone, which has the task of recognizing, binding, unfolding, but above all, transporting proteins into the central barrel chamber where their physiological degradation will take place through an ATP-dependent process that leads to their cleavage into small peptides (5-11 amino acids), which are released through lateral pores[2].

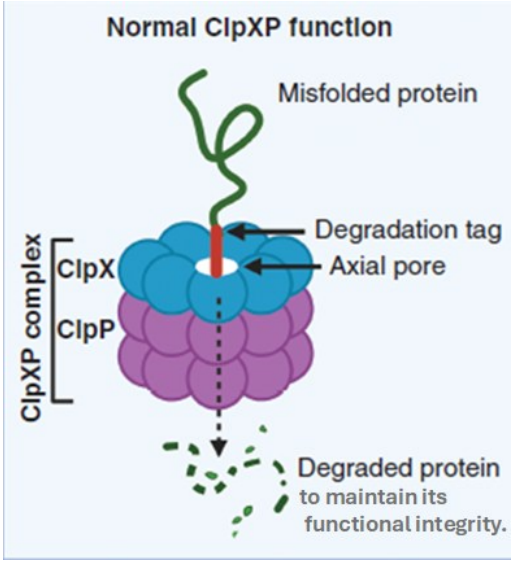

Figure 7. Schematic representation of the ClpXP complex

Although the role of *h*ClpP in DIPG is not yet fully defined, its expression is upregulated in multiple solid tumors including lung, stomach, liver, thyroid, bladder, breast, ovary, prostate, testis, and brain, as well as in haematological malignancies. For this reason, modulating its proteolytic activity may be an effective therapeutic strategy.

1.3.2. Physio-pathological role of ClpP

ClpP has gradually established itself as a central protein in tumor biology, acting not only as a molecular target but also as a true "mitochondrial checkpoint" capable of integrating energy metabolism, proteostasis, stress response, and cell survival programs. Evidence from various haematological and solid tumors has shown that ClpP is a functional target common to different tumor types, independent of tissue origin, with a high dependence on mitochondrial metabolism. Several studies have shown that ClpP is overexpressed in several primary samples of acute myeloid leukemia (AML) and that it is involved in the mitochondrial metabolism of leukemic cells,

promoting their survival. Therefore, in this case, the hyperactivation or inhibition of proteolytic activity has an important therapeutic effect and, in particular, its hyperactivation induced by activators such as **ONC201** or its analogues **ONC206** and **ONC212** (Figure 6), leads to unregulated proteolysis of mitochondrial complexes with a consequent increase in ROS and cell apoptosis[117]. Furthermore, in pancreatic ductal adenocarcinoma (PDAC), which is characterized by high clinical aggressiveness, ClpP is associated with processes of adaptation of tumor metabolism towards mitochondrial respiration, often related to chemoresistance. ClpP expression levels have been found to be an important prognostic biomarker, positively impacting patient survival. The use of **ZG111** (Figure 8), through the activation of ClpP proteolytic activity, triggered a process of unregulated degradation of the components of the respiratory chain both in vivo and in vitro[120].

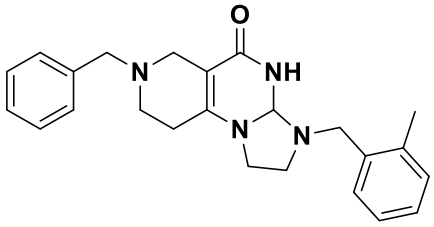

IMP075

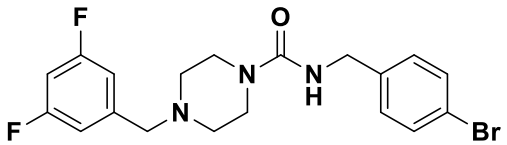

ZK53

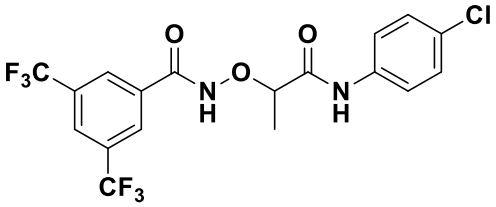

CCG1423

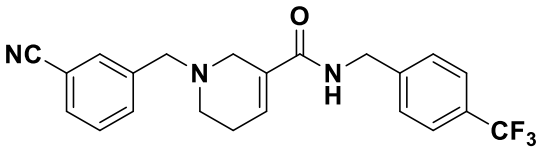

NCA029

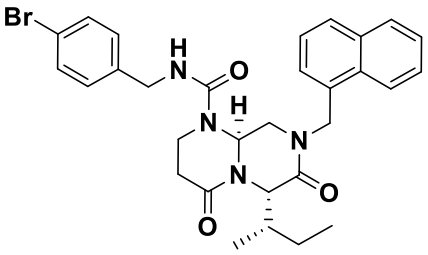

ZG111

Figure 8. Chemical structures of **IMP075**, **CCG1423**, **NCA029**, **ZG111** and **ZK53**.

ClpP is also associated with several liver disorders such as non-alcoholic steatohepatitis (NASH) and the onset of hepatocellular carcinoma (HCC)[121]. At the hepatic level, low levels of ClpP appear to promote the progression of these diseases, as its reduced expression leads to a general impairment of fatty acid oxidation processes, depletion of ATP levels, and accumulation of ROS, activating various inflammatory processes that culminate in steatosis and hepatocellular damage. When ClpP levels are restored, there is a reduction in oxidation and a general improvement in liver histology. Treatment with **ONC206** causes marked mitochondrial damage, characterized by organelle swelling, loss of mitochondrial membrane potential, ATP depletion, and accumulation of reactive oxygen species (ROS). Interest in targeting ClpP also extends to metastatic liver disease[122]. In orthotopic models of uveal melanoma liver metastases, the efficacy of ClpP activators, including **ONC201** and **ONC212**, was evaluated. Both compounds resulted in a significant reduction in tumor burden and prolonged survival *in vivo*. **ONC212** alters amino acid metabolism, reduces intracellular glutathione and polyamine reserves, and increases mitochondrial ROS production, promoting the activation of apoptotic signals[123].

Evidence has identified altered expression of ClpP, highlighting its possible role in the development of gastric cancer. Proteomic analysis has revealed abnormal regulation of various mitochondrial enzymes, including ClpP as well as components of the respiratory chain and lipid metabolism, indicating an alteration in redox metabolism and mitochondrial protein quality control systems[124]. In several gastric adenocarcinoma cell lines, **ONC201** induced a significant increase in the expression of the DR5 death receptor, increasing cell sensitivity to recombinant TRAIL. Furthermore, the combination of **ONC201** and TRAIL markedly activated the extrinsic apoptotic pathway, activating caspases 8 and 3, while the combination of **ONC201** and the PEGylated trimeric

form of TRAIL (TYL012) inhibited tumor growth and induced apoptosis in gastric cancer organoids without significant systemic toxicity[125,126].

In colorectal cancer, a disease characterized by high metabolic plasticity, altered mitochondrial metabolism has been observed, associated with ClpP overexpression. A derivative of **ONC201**, **IMP075** (Figure 8), through the hyperactivation of ClpP, has shown marked cytotoxic activity, causing mitochondrial membrane depolarization, reduced ATP levels, and increased ROS, with consequent activation of the ISR and induction of apoptosis[127]. Subsequently, **NCA029** (Figure 8), an activator designed from **CCG1423** (Figure 8), was shown to have high selectivity and potent antiproliferative activity in HCT116 cells (IC_{50} of 1.0 μM). Molecular docking and mutagenesis studies confirmed stable interactions with key residues (TYR118, TYR138, and TRP146) within the hydrophobic pocket of ClpP. From a functional standpoint, **NCA029** induces mitochondrial dysfunction, increased ROS, ISR activation, and transcriptional modulation of genes involved in stress and apoptosis pathways[128].

In lung cancer, the relevance of ClpP is due not only to mitochondrial stress, but also to its ability to actively regulate metabolic reprogramming, ferroptosis, and therapeutic response in both non-small cell lung cancer (NSCLC) and small cell lung cancer (SCLC). Experimentally, the selective *h*ClpP activator **ZK53** (Figure 8) has been developed, which in lung squamous cell carcinoma (LUSC) models promotes the degradation of electron transport chain proteins, compromising oxidative phosphorylation (OXPHOS) and inducing energy stress with cell cycle arrest in the G1 phase. Although it does not cause direct apoptosis, **ZK53** activates the ATM-mediated DNA damage response, suggesting a functional link between mitochondrial dysfunction and nuclear genomic surveillance[129].

1.3.3. Structure of ClpP

Although human ClpP is certainly the isoform to focus on for therapeutic purposes, it is essential to analyse, for the same aim, the structural studies carried out on bacterial isoforms. Crystallographic studies of ClpP of *Escherichia coli*[130], *Bacillus subtilis*[131] and *Plasmodium falciparum*[132] have identified the essential structural common portions of the monomer. It consists of an *N*-terminal loop, a large main domain, and a handle-like domain that forms the E-helix (Figure 9)[133].

- The ***N*-terminal loop** protrudes from the axial end of the cylinder and facilitates specific interaction with ClpX[134].

- The **main domain** is the key area for the implementation of protease activity; in fact, this region contains the active site consisting of the catalytic triad. This is located inside the cylinder and is a highly hydrophobic portion where the main interactions between subunits take place[131].

- The **HANDLE-LIKE (helix E)** domain is one of the most structurally relevant regions. This portion binds the two heptameric rings, forming a cylindrical structure approximately 10 nm high[133]. This region is so essential that its deletion leads to the formation of proteolytically inactive tetradecamers[135], as charge-charge interactions are established between the main domain and the handle domain. Each subunit is made up of seven α-helices and 11 β-strands. At the interface between these two domains are the residues that make up the catalytic triad that for *Sa*ClpP consists of Ser98, His123, Asp172[133]. The region where E-Helix is present is also the most dynamic, capable of assuming two distinct forms in solution depending on the temperature.

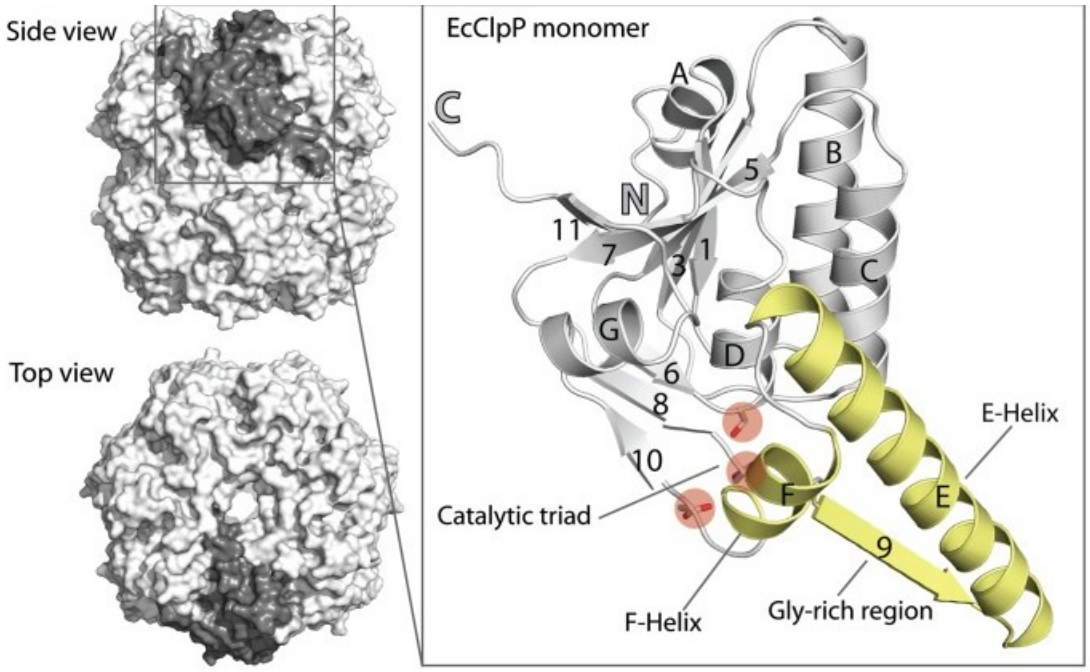

Figure 9. Main structural elements of ClpP. Top and side view of the tetradecameric ClpP complex from *E. coli* (EcClpP, PDBID: 1TYF, surface representation) with one subunit highlighted in dark gray. Relevant secondary structures (α-helices E and F, β-strand 9) are highlighted in gold[136].

1.3.4. Conformational dynamics between different states of ClpP

ClpP can assume three different conformational states: **extended**, **compact**, and **compressed**. It is essential to analyze how the portions, that form the protease, are subject to conformational changes in the dynamic transitions between different states in which there are significant structural changes[137]. Among the different forms, only the extended state has the structural conditions favourable to performi protease activity thanks to the correct positioning of the catalytic triad. The compact and compressed forms are inactive. The main differences between these states are located mainly in the handle domain. The **extended** state (Figure 10), has been observed in the crystal structures of ClpP from *Escherichia coli*[130,138–140], *Helicobacter pylori*[141], *Bacillus subtilis*[131,142],

Homo sapiens mitochondria[143], and *Staphylococcus aureus*[133,144,145]. In this state, the handle domain from opposing seven membered rings is well ordered and interlocked.

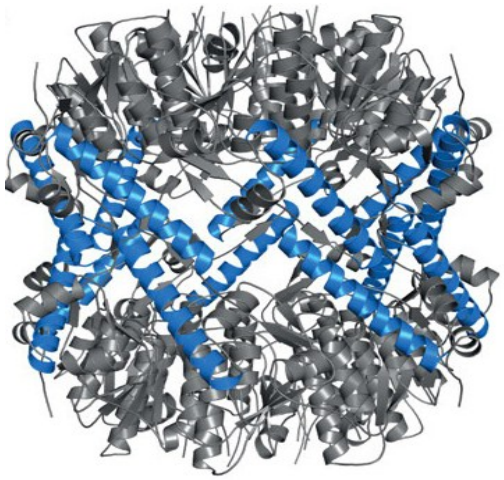

Figure 10. Tetradecameric *Sa*ClpP in the active, extended conformation[133].

There is a spatial arrangement of the carbonyl function of Ile122, which is located in the opposite direction to His123, part of the catalytic triad, plays an important role in the handle domain[133]. This causes the residues from Gln124 to Gln132 to protrude beyond the main domain, forming a β-sheet, allowing a series of highly conserved glycine residues, the Gly-loop, to bind to the corresponding residues of a monomer on the other ring, maintaining the equatorial surface of ClpP continuous (Figure 11). The E-Helix portion maintains a linear conformation from Ala133 to Thr158. This orderly condition ensures the correct distance in the active site between the amino acids involved in proteolytic activity.

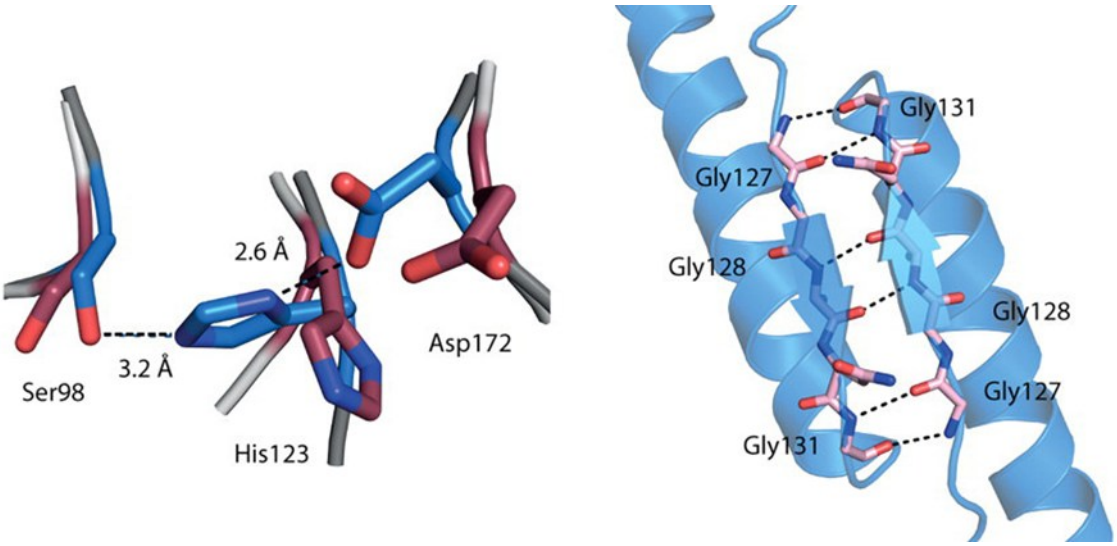

Figure 11. Catalytic triad in the extended state, with the correct positioning of the amino acids involved in proteolytic activity (on the left). Gly-loop, a series of glycine residues highly conserved in the bond between the residues of a monomer of one ring and the monomer of the opposite ring, which keeps the equatorial surface of ClpP continuous (on the left)[133].

Another structural feature is present in a highly conserved region, in what has been defined as the Asp170/Arg171 sensor (Figure 12), whose localization varies depending on the state. In the extended active form, Arg171 of one monomer interacts with Asp170 of the opposite monomer, allowing the protease to assume a tetradecamer structure and thus perform controlled proteolytic activity[133].

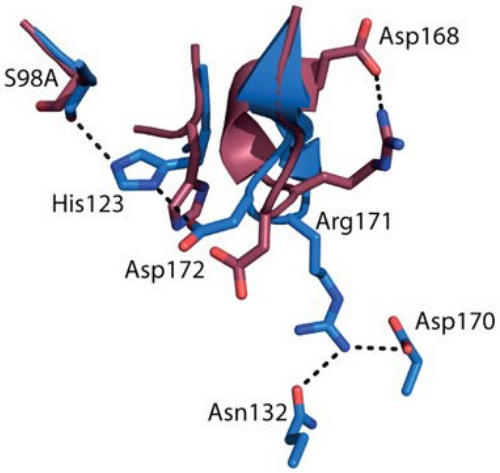

Figure 12. Asp170/Arg171 sensor in the extended conformation[133].

The **compressed** (Figure 13) state was first identified in *Sa*ClpP. Compared to ClpP from other species, it structurally presents a barrel compressed by 10Å in the axial direction, with approximately 14 lateral pores on the equatorial surface, whose diameter can vary up to 6Å (Figure 14). The *Sa*ClpP monomer is highly similar in structure to the monomers of other species, but differences can be observed in the handle domain.

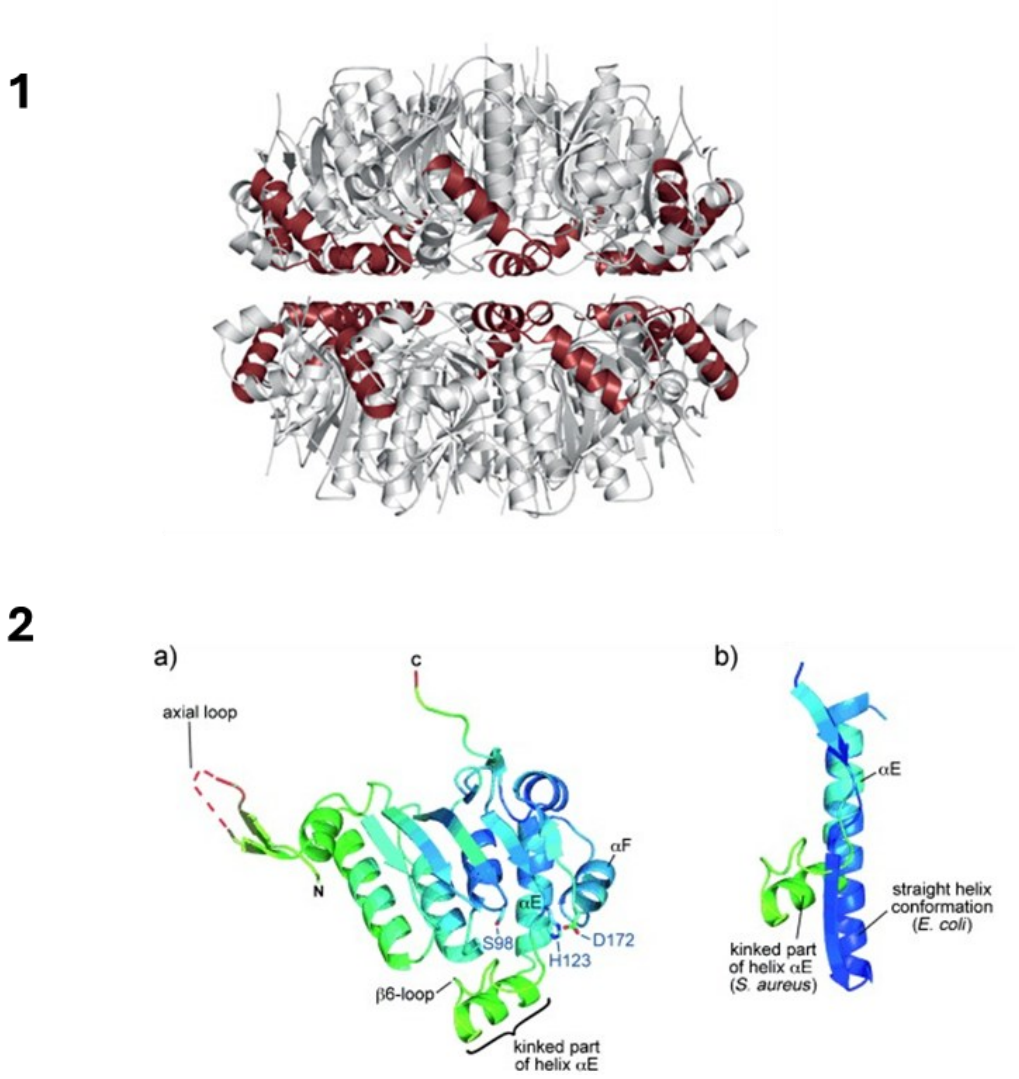

Figure 13. 1) Tetradecameric *Sa*ClpP in the inactive, compressed conformation[133]; 2) a-*Sa*ClpP monomer is shown secondary structure elements, the axial loop, the handle domain, and residues of the catalytic triad. b- Superposition of the kinked αE helix in the compressed state (*Sa*ClpP) with the straight αE helix in the extended state (*Ec*ClpP, PDBID: 2FZS, dark blue)[145].

In the extended state, the αE helix is almost always straight or partially disordered adjacent to the β6 strand, whereas in the compressed state of *Sa*ClpP, the αE helix is kinked, there is a major shift in the helix αF compared to the extended form and the β6 is disordered (Figure 15a)[145]. A conformational alteration is observed at the Arg/Asp sensor, causing Arg171 to interact with Asp168

and no longer be able to interact with Asp170 via hydorgen bonds. This causes Asp172 of the triad to rotate outward, resulting in a shift of His123 by approximately 3.5 Å and misalignment of the triad, which can no longer perform its main activity[136].

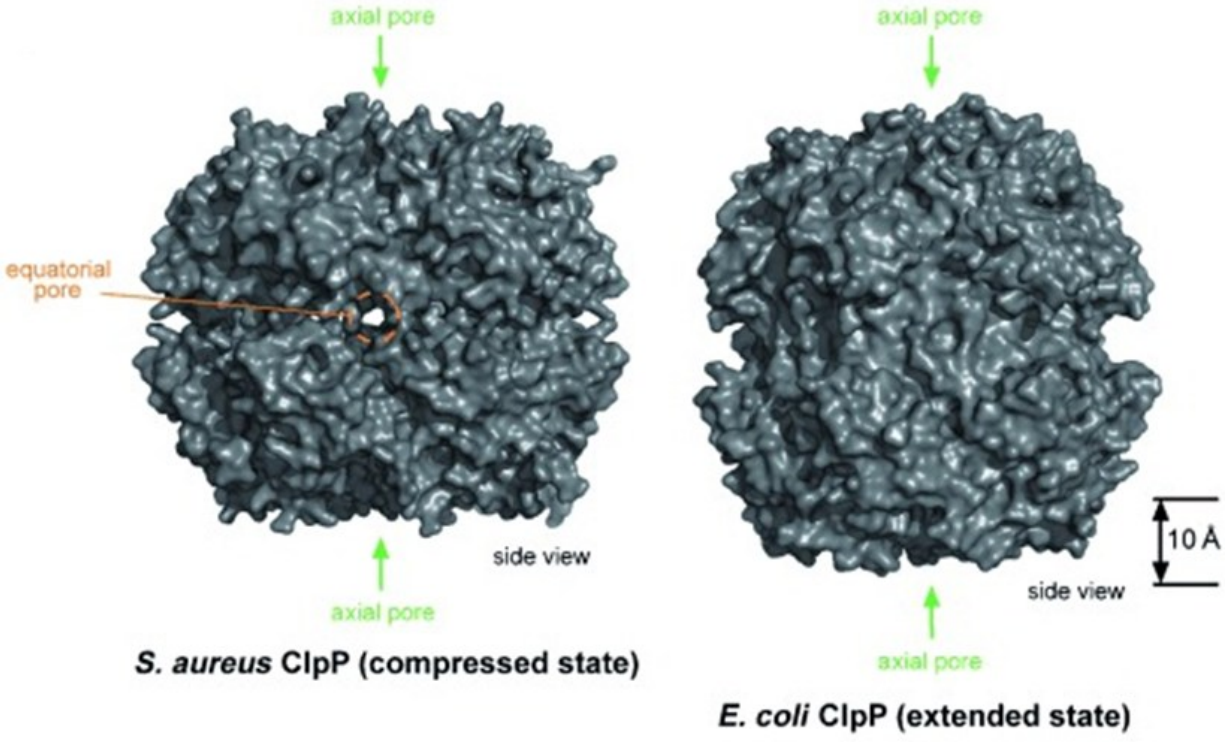

Figure 14. Transition in the ClpP ring–ring interface and formation of equatorial pores. Surface representation of *Sa*ClpP in the compressed state with an equatorial pore and *Ec*ClpP in the extended state without equatorial pores during catalytic cyle.

Through NMR spectroscopy analysis[146] and predicted from biochemical data and calculations[147], an intermediate state has been identified that highlights the presence of a conformational switch from the extended to the compressed state. This intermediate state has been defined as **compact** and has characteristics similar to the extended state. The **compact** (Figure 17B) state is found in the ClpP from *E. coli*[147], *Streptococcus pneumonia*[135], *Mycobacterium tuberculosis*[148], *and Plasmodium falciparum*[149]. No kinked αE is observed in the compact state, but a minor shift of the αF helix is

observed (Figure 15b) [145]. Residues 139-150 are disordered, and the two rings, through equatorial rotation, cause the opposing αE surfaces to slide over each other, bringing the apical surfaces approximately 10Å closer together. The components of the catalytic triad are generally disorganized, and the presence of a disordered β6 indicates that the protease is proteolytically inactive in this state[147].

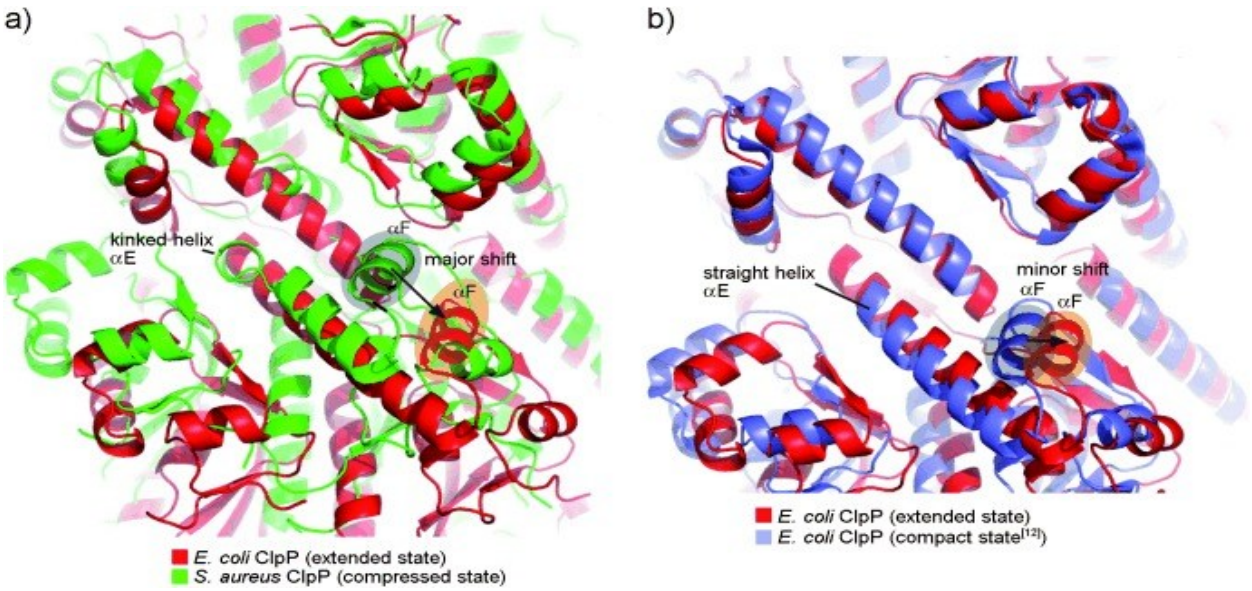

Figure 15. The ClpP compressed state different from compact state. **a**) Superposition of *Sa*ClpP (compressed state) with *Ec*ClpP in the extended state (PDBID: 2FZS) reveals kinking of helix αE and a major shift in helix αF; **b**) Superposition of *Sa*ClpP (compressed state) with *Ec*ClpP in the compact state (PDBID: 3HLN) reveals no kinking of helix αE and only a minor shift in helix αF[145].

Understanding the transition between different conformational states is essential to understand the mechanism underlying the ClpP catalytic cycle, whose primary purpose is to degrade misfolded proteins. The study of conformational changes at the ring-ring interface identified the possibility of αF helices shifting up to 9Å and highlighted the structural importance of the Asp170/Arg171 sensor located in a region adjacent to the αF helices. These residues establish a series of salt bridges with

their counterparts on the opposite ring. These interactions, which are essential for stabilizing the ring-ring interaction, undergo a reorganization during the ClpP catalytic cycle that does not lead to the dissociation of the two rings at any time, but which always remain in their tetradecamer state even in the presence of a disordered handle domain. These characteristics have made it possible to define a catalytic cycle consisting of three phases: 1) initially, the ClpX chaperone unfolds the target protein, which is then translocated through the axial pores into the barrel chamber, 2) the proteins are fragmented into small peptide fragments in the catalytic triad region, 3) in the last phase, the protein undergoes a conformational change in the handle domain, where an axial ring-ring rotation occurs, causing the active sites to close and opening the equatorial lateral pores, allowing the release of the peptide fragments[145].

In this state, Ala140 is identified as a "hinge" region in the transition between the extended and compressed forms through the compact form. By molecular dynamics simulation, a true helical unfolding/refolding process was identified at the *N*-terminal portion of the helix E (133-145). Initially, the first two turns of the helix (133-140) are unfolded and adopted turn structure, then they partially readapt into α-helical shape with an increasing of the degree of kinking of segments 133-158, and finally these segments stabilize into a helical structure. As a result of this rearrangement, the helix E, which was elongated in its extended state, is broken into two shorter helices at the Ala140 hinge (Figure 16)[150].

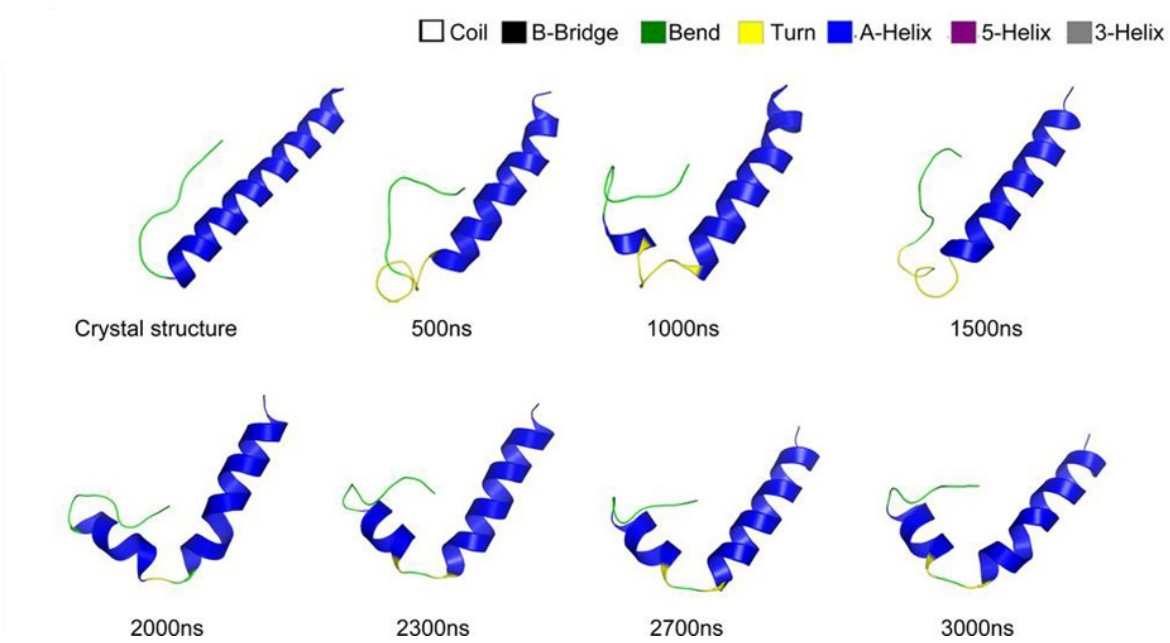

Figure 16. Snapshot structures of ClpP molecular dynamics that showing the dynamic unfolding/refolding process of ClpP leading to a kinked helix αE^{150}.

Another characteristic feature of ClpP dynamism is the narrow axial pore at the center of each heptameric ring. This pore, and therefore its diameter, is crucial to the activity, as proteins are directed into the proteolytic chamber of ClpP through its opening. This diameter varies significantly depending on the conformational state of ClpP. The different conformations are also associated with a variation in the height of the cylinder.

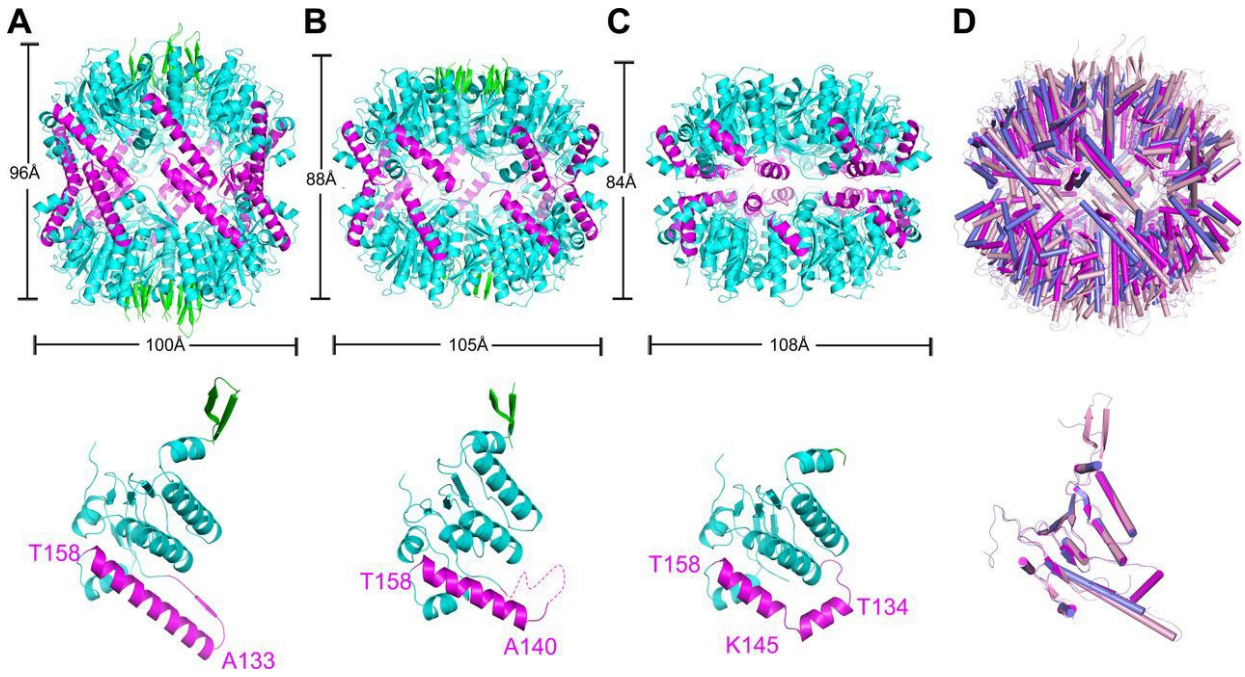

Figure 17. **Three states observed in ClpP.** A) structure of *Sa*ClpP (PDBID: 3STA) showing the ClpP tetradecamer in the extended state. B) structure of *Sa*ClpP (PDBID: 4EMM) showing ClpP in the compact state. With Ala140 "hinge". C) structure of *Sa*ClpP (PDBID: 3ST9) showing the enzyme in the compressed state, the E-Helix is broken into two shorter helices at the Ala140 hinge. D) alignment of three states. The extended, compact, and compressed monomers are shown in *pink*, *purple*, and *magenta*, respectively[150].

1.3.5. Human mitochondrial caseynolitic Protease P (*h*ClpP)

After defining the essential characteristics of bacterial ClpP, it was identified that, *in vitro*, *h*ClpP has structural and enzymatic characteristics similar to those of *Escherichia coli*[151], with 108 overlapping amino acids out of 193 and a C-terminal extension of 28 amino acids present only in the human form, which, however, does not influence its activity. *h*ClpP and *e*ClpP have an identical amino acid sequence that is 56% overlapping and 70% similar[143]. This similarity is highlighted by the finding that the heterologous *e*ClpX/*h*ClpP complex is indistinguishable from its homologous

counterpart *e*ClpXP under electron microscopy. They differ in terms of activity, as the human form has 1-5% less peptidase activity than the bacterial form and differs in terms of protein substrate specificity. This specificity is not attributed to homologous ClpX-ClpP interactions but only to ClpX, as the bacterial form does not recognize the same substrates as the human form, even though it correctly transports the substrate in the presence of a heterologous form[152].

*h*ClpP is present in solution as a mixture of heptamers and tetradecamers, while that of *E. coli* is in the form of a stable tetradecamer[137], as there are significant differences in the amino acid sequence at the β9 strand, in the region where interactions between the two rings of *h*ClpP occur[151]. The structural stability of the tetradecamer of bacterial forms is due to the presence of a conserved region consisting of residues E143 and R147, which establish an intra-helix salt bridge, stabilizing the handle domain in the extended active state. However, in the human form, these residues are replaced by A192 and E196 in the same positions, making the protein intrinsically more unstable in its active conformation and more subject to oscillating between compact and compressed states, both of which are catalytically inactive. In fact, according to PDB data, human ClpP has almost always been identified in its inactive compact conformation, even in the presence of activators such as **ONC201**. Like the bacterial form, in the **ONC201**-bond structure, it has a tetradecamer structure formed by two stacked heptameric rings of ClpP, and there is an absence of electron density at residues 181-187 of the β strand handle (Figure 18). In the terminal handle domain, the handle helix loses two turns (196-214) and a barrel height of 81Å is observed, similar to the more familiar bacterial form. Residues E225 and R226, which constitute the oligomerization sensor, are in a spatial position such that they interact, inducing a separation of the loop containing Q179, which causes a misalignment of the catalytic H178, leading to stabilization of the compact inactive form. However, crystallographic analysis and cryo-electron microscopy have also resolved the structure of the human form in its extended active state. *h*ClpP in the extended state was resolved by X-ray crystallography at a resolution of 2.8Å, revealing a predominant tetradecamer form and a barrel

height of 95Å, greater than in the inactive state, with a clear electron density in the triad region involving residues S153, H178, and D227. The handle domain is completely ordered, and residue E225 of the oligomerization sensor is involved in H-bonding with Q179, which determines the correct positioning of H178 at the catalytic triad level, allowing proteolytic activity to be carried out and also highlighting, in the human form, the great dynamism of the protein in the transition between the various states[137].

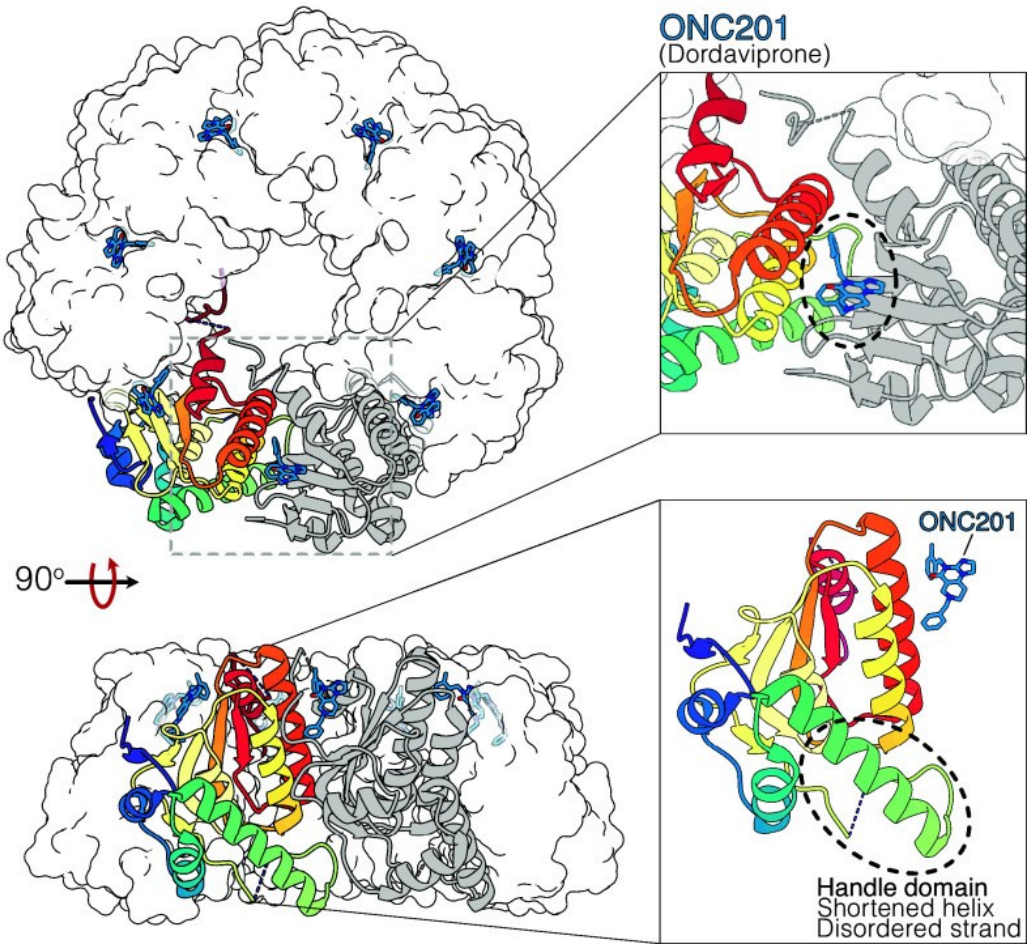

Figure 18. Structure of human mitochondrial ClpP **ONC201**-bound in the inactive compact state (PDBID: 6DL7) with shortened handle domain helices and disordered handle strands. **ONC201** binds to the hydrophobic pockets of ClpP (Inset – Top).

1.3.6. *h*ClpP activators

Once the structural elements of ClpP have been identified, it is important to understand how these elements and its most dynamic regions are influenced by the presence of modulators of the proteolytic activity from the perspective of their therapeutic potential. Activators are the most studied, and in-depth analysis using crystallographic studies can be a particularly useful tool to identify the structural motifs essential to activate the protease. In their mechanism of action, activators bind allosterically to ClpP. Specifically, one activator molecule binds to each of the seven allosteric active sites present on each ClpP heptamer, in a hydrophobic region connecting the tetradecamer subunits, binding a total of 14 molecules. The binding site of these activators is spatially distant from the site where proteolytic activity occurs, indicating the dynamism of this complex.

The binding of the activator induces several conformational changes compared to the apo state, without the activator. First, activation induces a physical detachment of ClpX from ClpP, which remains in its proteolytically active state. Subsequently, an increase in the diameter of the axial pore is observed, which assumes a configuration that facilitates substrate entry. The binding of the activator stabilizes the protein in the extended proteolytically active state, even though analysis of the co-crystal complexes of the activators with ClpP shows the characteristics of the compact state. This is due to the crystallization conditions and the existence of a dynamic equilibrium between the two forms in solution, highlighting the intrinsic instability of the human isoform. This activation induces an imbalance in mitochondrial proteostasis, resulting in proteolysis of the respiratory chain subunits, ribosomal proteins, and metabolic enzymes, causing cell death.

1.3.7. X-ray crystallographic analysis of hClpP activators

Several activators of *h*ClpP are known, such as imipridones, acyldepsipeptides (**ADEPs**) and oxadiazonocarboxyamides (**D9**) **(**Figure 19)[1,153]. The most extensively studied ClpP activators are imipridones, with **ONC201** as the prototype; later, *in silico* studies identified a tetrahydropyridopyrimidinone (**THPPD**)[119,154] scaffold that yielded more potent *h*ClpP activators (e.g., **TR-57**, Figure 19). From these activators, other derivatives with structural characteristics similar to the previous ones were developed, such as **ZG** and **ZK53** (Figure 8). High-resolution structures of the co-crystal complexes of these ClpP activators with *h*ClpP are available, and in-depth analysis of the interactions is essential to understand precisely which amino acids are key to the interaction and thus define the minimum characteristics of the molecules to begin a rational design process for a new powerful *h*ClpP activator, which is the central focus of this work.

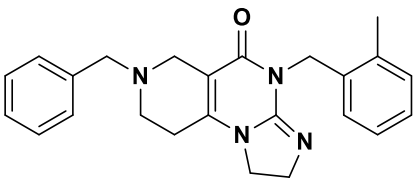

ONC201

*h*ClpP EC_{50} = 1.0 μM

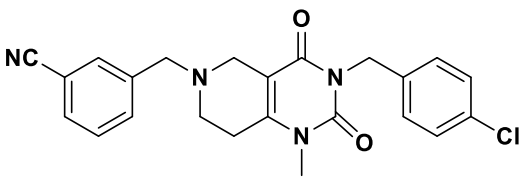

TR57

*h*ClpP EC_{50} = 0.13 μM

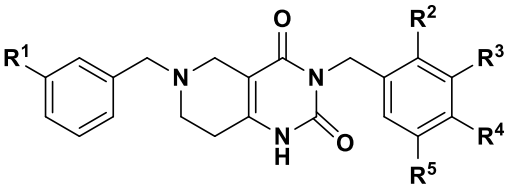

THPPDs

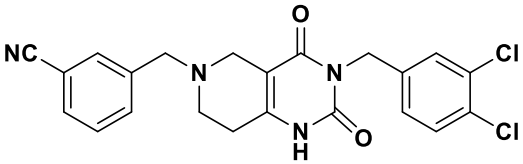

THX6

*h*ClpP EC_{50} = 1.18 μM

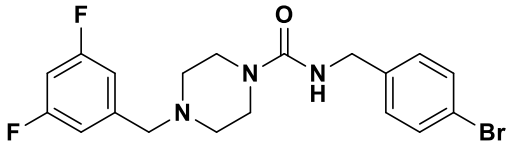

ZK53

*h*ClpP EC_{50} = 0.22 μM

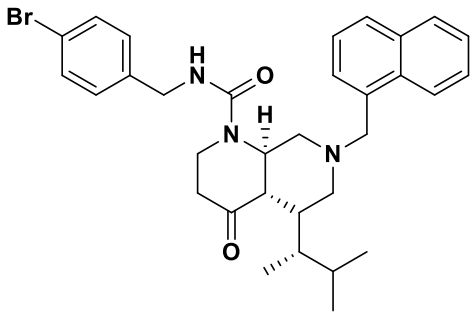

ZG111

*h*ClpP EC_{50} = 1.4 μM

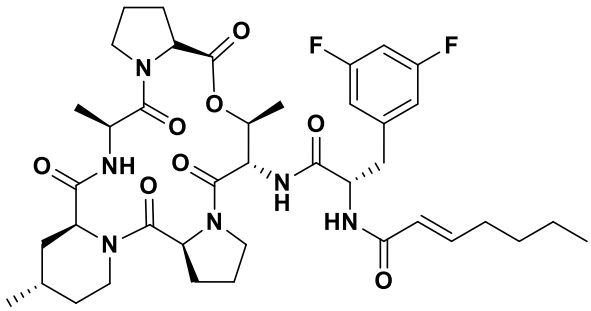

ADEP-28

*h*ClpP EC_{50} = 3 μM

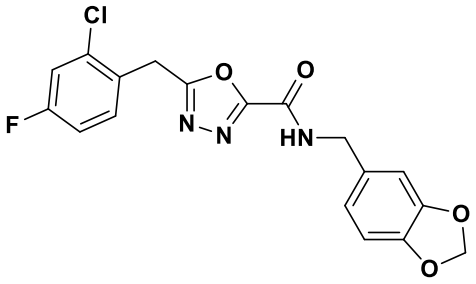

D9

*h*ClpP EC_{50} = 110 μM

Figure 18. Chemical structures of **ONC201**, **TR-57**, **THPPDs**, **THX6**, **ZK53**, **ZG111**, **ADEP-28**, and **D9** and their EC_{50} (half maximal effective concentration).

ONC201

Since its discovery, **ONC201** has been the molecule used as a benchmark with great therapeutic potential, so much so it has been included in several clinical trials and is now approved for the treatment of h-GGs. **ONC201** (*h*ClpP EC_{50} = 1.0 μM) is an allosteric activator of ClpP belonging to the chemical class of imiprodones whose binding has been extensively studied through X-ray crystallographic analysis. **ONC201** has been co-crystallized with human ClpP with a complex resolution of 2Å (PDBID: 6DL7). The binding of **ONC201** stabilizes the compact inactive form of the protease, inducing an enlargement of the axial pore diameter from 12Å in the apo state to 17Å and leading to a reduction in cylinder height from 93Å to 88Å. The interactions observed include a series of H-bonding and hydrophobic interactions. The non-planar piperidine nitrogen interacts with the hydroxyl group of Tyr118, while the carbonyl oxygen atom of the bicyclic ring interacts, via H-bonding mediated by an H_20 molecule, with the side chain of Gln107 and the carbonyl of Leu104. The phenyl ring located between Tyr138 and Tyr118 establishes several hydrophobic π-stacking interactions (Figure 20). X-ray crystallographic analysis has identified several conformational changes in residues 178-193, including the end of strand β6, the entire strand β7, and one-third of helix α5. These changes cause a misalignment of the catalytic triad in which the His178 ring is about 5Å further away from the catalytic Ser153, rotating about 70° together with Asp227. The Asp227 of the catalytic triad of two heptamer-heptamer subunits, which are 17Å apart in the apo form, move closer together in the presence of the activator, reaching 4.6Å. His178 is closer to Ser181 than that of the catalytic triad, and the hydroxyl group of this serine is 3.2Å from the carboxylate of Asp227[117].

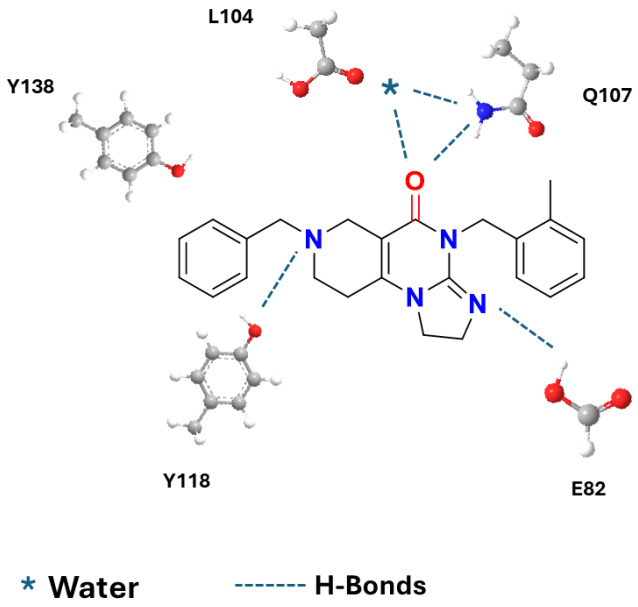

Figure 20. **ONC201** with interactions with key amino acids in the allosteric site of *h*ClpP.

Starting from the structure of **ONC201**, a substituent translocation strategy was implemented to stabilize the bond with the protease by attempting to insert additional interactions with Y138 or Q107 or L104. The insertion of the benzyl group on the imidazole nitrogen of **ONC201** led to the creation of a structure whose binding mode always occurs in a U-like pincer conformation, as in **ONC201** and **ADEP-28**, but which establishes additional interactions due to the variation of the distances between groups, and translocation of the substituent. In compound **IMP075**, there is a clear improvement in activity compared to **ONC201**, despite the presence of the same substituents. In the binding mode, analyzed by molecular dynamics, the unsubstituted benzyl ring always inserts between Y118 and Y138, establishing π-stacking interactions, while the piperidine nitrogen atom establishes interactions with Y118 at a shorter distance than **ONC201** (3.0Å). The carbonyl function of the ring establishes an interaction with Y138 (2.7Å), which does not occur for **ONC201** but is present with one of the carbonyl functions of **ADEP-28**. However, in the optimization process using the substituent translocation strategy of **IMP075**, compound **16z** was obtained in which, again using molecular dynamics, it can be observed that the molecule inserts itself into the binding site in a

conformation rotated 180° respect to the other compounds. This allows the carbonyl function to interact with the terminal amide of Q107 but, above all, allows the additional interaction, never observed before, between the amide nitrogen of the cycle and Y138 (Figure 21)[155].

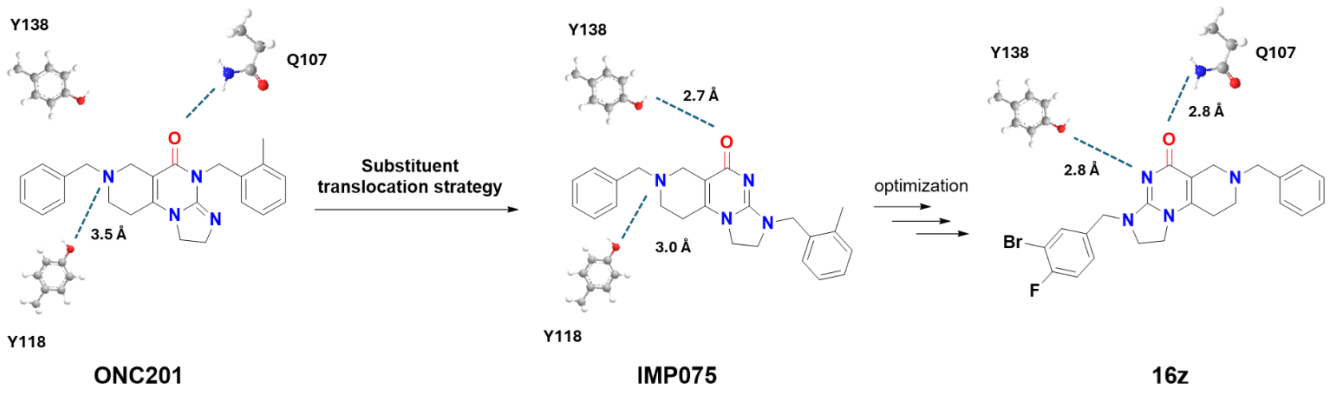

Figure 21. Substituent translocation strategy, with H-bonding by molecular dynamics, that led from **ONC201** (EC_{50} = 1.0 μM) to **IMP075** (EC_{50} = 0.30 μM), which through structural optimization led to compound **16z** (EC_{50} = 0.20 μM).

This analysis was confirmed by the study of **IMP075** co-crystals with *h*ClpP (PDBID: 8YLB). In fact, interactions with Y118 of the carbonyl are shown, in addition to a further direct interaction with the terminal amide function of Q107. Unlike molecular dynamics, the analysis of co-crystals emphasized that the imidazole nitrogen atom, essential in the interaction of **ONC201**, has a marginal effect in stabilizing the bond in **IMP075** and that, on the other hand, it could preclude interactions with nearby amino acids given the large distances with E82 (5.1 and 5.2Å), I84 (4.1Å), and R78 (7.4Å), which are necessary to establish H-bonding. Based on this assessment, an initial structural simplification of **IMP075** was carried out, specifically a ring-opening scaffold mechanism at the imidazole nucleus level, which led to lead **Cmpd2** (EC_{50} = 1.22 μM), which underwent an optimization process to obtain compound **7k** (EC_{50} = 0.79 μM). AutoDock was used to perform a docking fit of wild-type *h*ClpP (PDBID: 6DL7) with **ONC201**, **Cmpd2**, and **7k**. ONC201 exhibits the interactions highlighted so far, in which the carbonyl of the bicyclic ring acts as an H-bond

acceptor with Y118 (3.5Å) and establishes π-stacking interactions with Y138. In compound **Cmpd2**, the hydrophobic interactions that ensure the U-shape conformation are maintained, but the interaction of Y118 with the piperidine nitrogen atom of the ring is lost, while the interaction of the nitrogen resulting from the opening of the ring with the carbonyl of E82 (3.5Å) is gained. Contrary to what happens in compound **Cmpd2**, the insertion of a *p*-F atom on the right benzyl ring leads to compound **7k**, in which the interaction with Y118 is restored with the piperidine nitrogen (2.8Å) as an H-bonding acceptor, and the interaction of the nitrogen atom bound to the benzyl ring is also observed, again as an H bond acceptor, with glutamate 82 (2.9 Å), and in both cases the bond distance is reduced, further stabilizing the bond (Figure 22)[156].

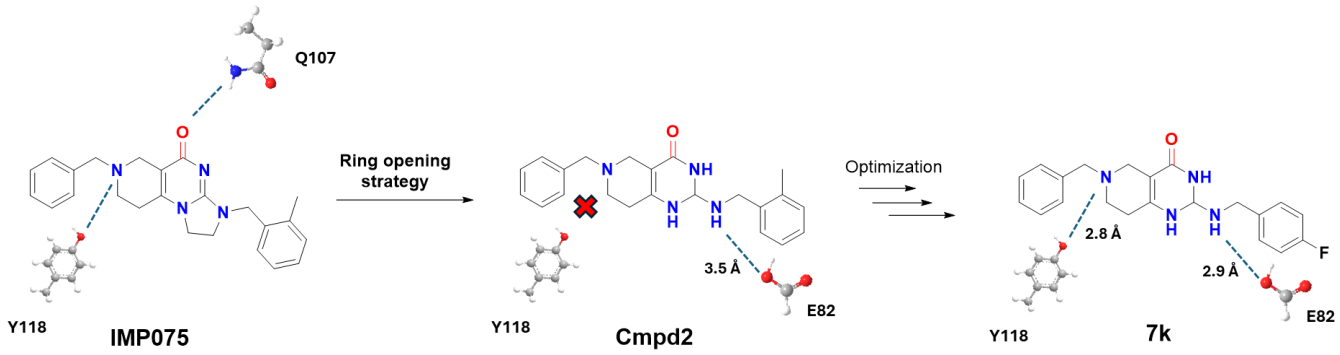

Figure 22. **IMP075** (PDBID: 8YLB) ring opening strategy and docking fit of wild-type *h*ClpP (PDBID: 6DL7) with **ONC201**, **Cmpd2**, and **7k**.

ADEP-28

Another class of activators of ClpP consists of ADEP acyldespeptides, initially developed as antibiotics. Analysis of the **ADEP-28** complex with *h*ClpP (PDBID: 6BBA), obtained at a resolution of 2.8Å, shows that it behaves as an allosteric activator in the same way as imipridones. It stabilizes ClpP in its compact state, leading to an increase in the axial pore diameter and a reduction in the height of the complex from 90Å to approximately 82Å. **ADEP-28** binds to the interface between neighboring ClpP subunits, inducing a significant structural change in the binding zone. The two

opposite subunits are linked together by ionic interactions, in particular R78 of one with E109 of the other. In the ADEP interaction, H-bonding is observed between Y118 of one subunit and Y138 of the other with the carbonyl of the depsipeptide ring. An H-bonding, mediated by an H_20 molecule, is established between Q107 and the carbonyl oxygen atom of the amide that connects the long hydrophobic chain to 3,5-difluorophenyl. The latter creates hydrophobic interactions with W146. Although the large depsipeptide ring is exposed to the solvent, it establishes several hydrophobic interactions due to the presence of multiple nitrogen heterocycles. There is interaction between His168 of β5 and the methyl piperidine ring, and it is specifically this amino acid that conferred a higher binding affinity of **ADEP-28**, providing the space to accommodate this substituent (Figure 23). This does not occur in the bacterial ClpP analogue, where there are several bulkier amino acids that do not allow for correct positioning.

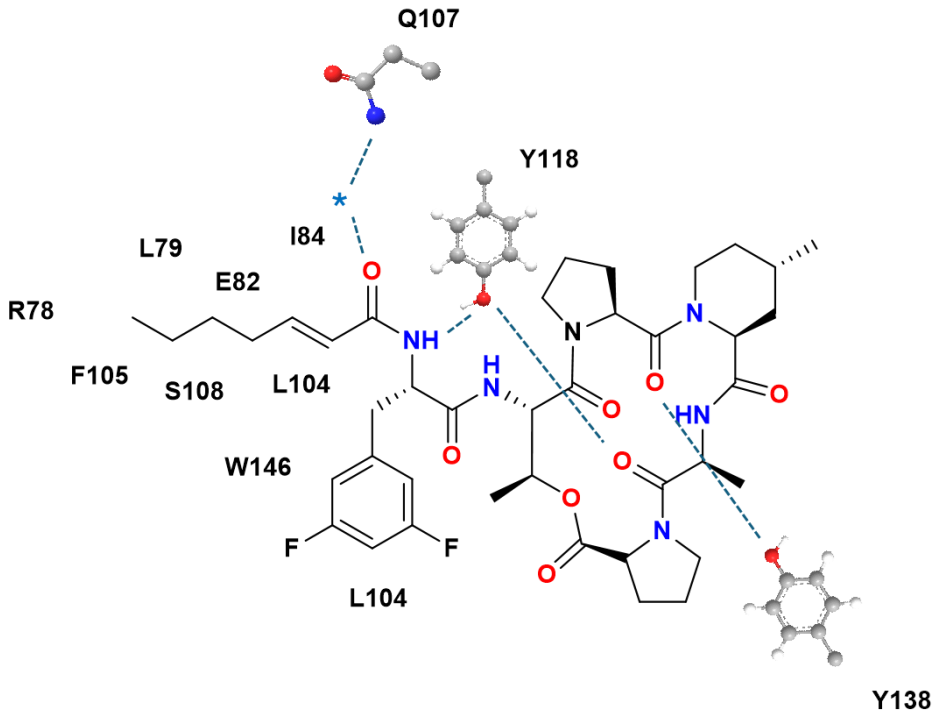

Figure 23. **ADEP-28** interactions with key amino acids in the ClpP allosteric site.

When **ADEP-28** binds, it makes the *N*-terminal axial loop orderly compared to the initial disordered condition. This is possible thanks to the establishment of three new hydrogen bonds between E64 of one subunit and R78 of the same subunit and with E109 of the other subunit. Finally, R78 also interacts with E82 of the other subunit. This rearrangement causes the opposing subunits to move closer together, leading to a misalignment of the catalytic triad. His178 of one subunit interacts with D227 of the other, leading to the loss of the initial interactions between His178 and Ser153 within the subunit and D227 with Q194 between the subunits, resulting in a compact, inactive form of the tetradecamer[157].

D9

The extensive structure-activity relationships investigation that led to the identification of compound **D9** (Figure 24) (EC_{50} ~ 110 μM) was also essential, once again, in identifying the structural determinants for ensuring peptidase activity. The main modifications were made at the benzyl moiety which, as in other activators, is one of the pendants that fits into the hydrophobic pocket of the protease. The modification of the halogens on the aromatic ring, both in position and type, did not lead to any improvement in activity. The introduction of an electron-donor group led to a loss of peptidase activity, as did the presence of an unsubstituted aromatic ring. These data show that the presence of the benzyl ring and the electron-withdrawing effect of the halogens, which in **D9** are 2-Cl and 4-F substitution, are essential. The second part of the "pincer" structure, consisting of benzodioxole, showed greater tolerance to modifications, maintaining activity when substituted with a methoxy-substituted benzyl ring or with a chain extension. Activity is completely lost when substituted with hydroxy, alkyl, dimethoxy, alkyne, or imidazole.

The study on how this compound binds to the protease was carried out by analyzing the **D9** complex with a mutated form of human ClpP Y118A (PDBID: 6H23). This form, in the bacterial analogue,

has greater peptidase activity due to the formation of a more stable tetradecamer. This increase is also observed in the human mutant, and in the presence of **D9**, the activity is even more pronounced. Like activators, **D9** stabilizes the protease in the compact inactive conformation, with the pore diameter opening from 15 to 25Å and the height of the tetradecamer reducing from 90 to 80Å. This mutant form, has once again, highlighted the importance of hydrophobic interactions in ensuring activity. At the benzyl level, π-π stacking interactions are established with a recurring Y118, Y138, W146 (YYW) motif, identifying tryptophan 146 as an amino acid capable of conferring selectivity to the human ortholog rather than the bacterial one, as W146 is not present in this form. The misalignment of the catalytic triad induces a shift in Q179, which thus coordinates serine, inhibiting its activity. Despite the same binding modes as ADEP, the benzyl ring of **D9** shows a slight shift, probably due to the Y118A mutation[158].

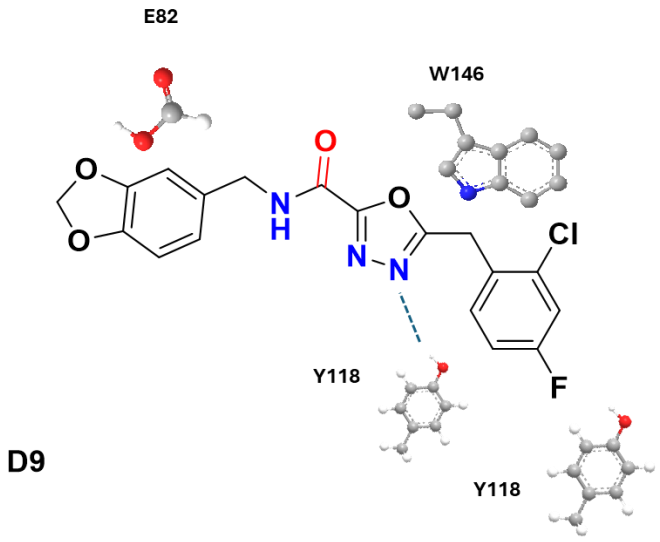

Figure 24. Chemical structure of **D9** with interactions with key amino acids in the allosteric site.

TR-COMPOUNDS

Starting from imipridones, with **ONC201** as the prototype; later, *in silico* studies identified a tetrahydropyridopyrimidinone (**THPPD**) scaffold that yielded more potent *h*ClpP activators.

Analysis of the co-crystals of TRs with *h*ClpP made possible to define important structural features that activators must retain in their rational design, thanks to differences in binding with other known activators. Five different TRs were identified, **TR-27** (PDBID: 7UVM) and **TR-65** (PDBID: 7UVR), which have an imipridone structure identical to **ONC201**, but differ from the last in the substituents present on the two benzyl rings (Figure 25).

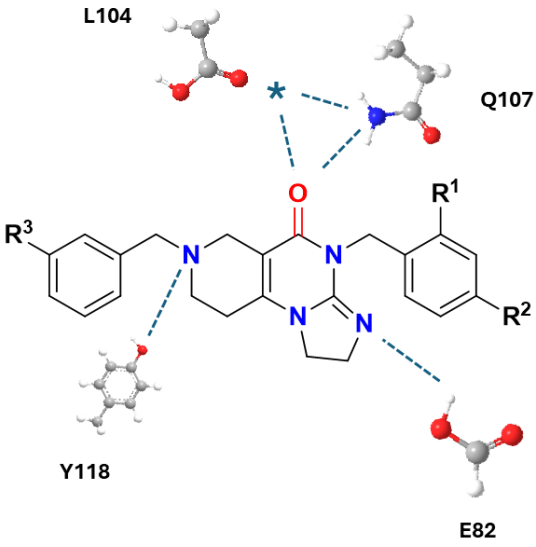

Compound	R^1	R^2	R^3
ONC201	CH_3	H	H
TR-27	H	Cl	CCH
TR-65	H	Cl	CN

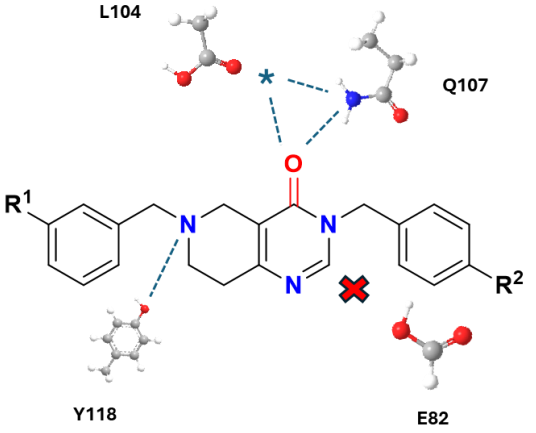

Compound	R^1	R^2
TR-107	CN	Cl
TR-133	CN	Br

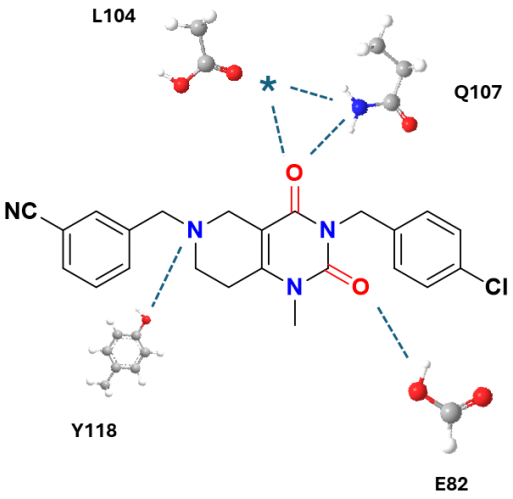

TR-57

Figure 25. Chemical structure of **ONC201** and **TR** compounds.

As with all the activators analyzed, the TR compounds stabilize ClpP in its compact conformation, in relation to the already known conformational equilibrium during its proteolytic cycle. They are located within the allosteric site according to a "pincer" topology, like **ONC201**, and several interactions of different types are identified, depending also on the structural features of the different compounds. The two benzyl rings show π-stacking interactions with the side chains of E82, H116, Y118, Y138, and W146. The bond is stabilized by three H-bonds; the non-planar piperidine nitrogen atom of the bicyclic ring interacts with the hydroxyl of Y118, a residue located at the end of the enzyme. An interaction is observed between the carbonyl of the bicyclic ring and the amino group of the side chain of Q107, which is located closer to the pore region of ClpP. For TR-27 and TR-65, there is an interaction between the imidazole nitrogen, as for **ONC201**, and the carboxylate portion of E82, and the same residue interacts with an additional carbonyl present in the bicyclic ring of **TR-57** (PDBID: 7UVN), which appears to be crucial for stabilizing the bond with the enzyme, also in relation to the lower activity of the **TR-107** (PDBID: 7UVU) and **TR-133** (PDBID: 7UW0) due to the absence of an H-bonding acceptor group[117]. Again, studying how substituents on the benzyl rings affect activity was key to solving the architecture of ClpP. The more polar cyano group is

preferred to the etinylene group in binding to ClpP, probably due to the extensive peptide bonds that make up the walls of the large hydrophobic binding pocket, in which, however, regions with both positive and negative surface potential are distributed. By comparing the binding of these compounds with **ADEP-28**, it was possible to identify how the binding type and overall charge influence activity. In the structure of **ADEP-28**, the C-7 aliphatic chain has excessive conformational freedom around the simple C-C bonds compared to the benzyl of TRs, which, thanks to a smaller structure, are positioned in a pincer conformation, showing greater complementarity with the H sites of the binding site. The small size compared to **ADEP** also influences interactions with Q107 and Y118, as in the large structure of **ADEP-28** these interactions cover a smaller cross-section and are positioned below its centre of mass, unlike TRs, which have a higher area/mass ratio, further stabilizing covalent interactions. Furthermore, the interaction with E82 is essential for stabilizing the bond, while no variation is observed in the effect of the different substituents that interact with the terminal carboxylate. However, the importance of the electron-withdrawing effect of substituents on benzyl rings is highlighted, as in **TR-27**, where *p*-Cl allows anion-π interactions with E82, further stabilizing the bond thanks to the interaction with the phenyl ring of F105[154].

ZG111/ZG36/ZG180

ZG111 (Figure 26) has been identified as a ClpP activator with an EC_{50} = 1.4 μM with therapeutic potential in the treatment of pancreatic ductal adenocarcinoma, inducing mitochondrial dysfunction and tumor suppression *in vivo* and *in vitro*. The **ZG111**/*h*ClpP complex (PDBID: 7VP9) was analyzed at a resolution of 2.55Å. Like activator, it stabilizes the protein in a compact inactive state, determined by an enlargement of the pore diameter from 13 to 26Å and a reduction in the height of the tetradecamer from 91 to 85Å. Several H-bonds that stabilize the bond are observed in the interaction. The carbonyl of the cycle interacts with Y138, the carbonyl oxygen atom of the amide interacts with Q107, while the nitrogen atom of the same amide moiety establishes H-bonding with

E82. In identifying **ZG111**, a synthetic optimization process was implemented starting from the lead compound **ICG-001** (Figure 26), which has an EC_{50} = 9.2 μM. This has an unsubstituted benzyl, and the greater affinity of the **ZG111** compound is therefore due to the presence of the 4-bromobenzyl, as the electron-withdrawing effect of the substituents is essential for the activity. **ZG111**, like **ONC201** and **ADEP-28**, fits into the active site in a pincer conformation, with two pendants that fit into highly hydrophobic regions. These pendants consist of the naphthyl and the 4-bromobenzyl group. The importance of this binding mode and therefore of the presence of these hydrophobic pendants has been confirmed by the complete loss of activity in **ZG63** (Figure 27) in which the hydrophobic naphthyl ring is replaced by one hydrophilic N-atom into the naphthyl motif in ICG-001, which is unfavourable for the hydrophobic interactions.

The **ZG111** bond brings the *N*-terminal axial loop into an ordered state, and an absence of electron density was observed at residues S181 and A192, indicating a shortening of the E-helix typical of the compact conformation with consequent misalignment of the catalytic triad. Furthermore, it is observed that Y118, which is one of the key interaction sites with activators, is rotated by 120° to minimize the steric hindrance due to the large naphthyl group of **ZG111**[120].

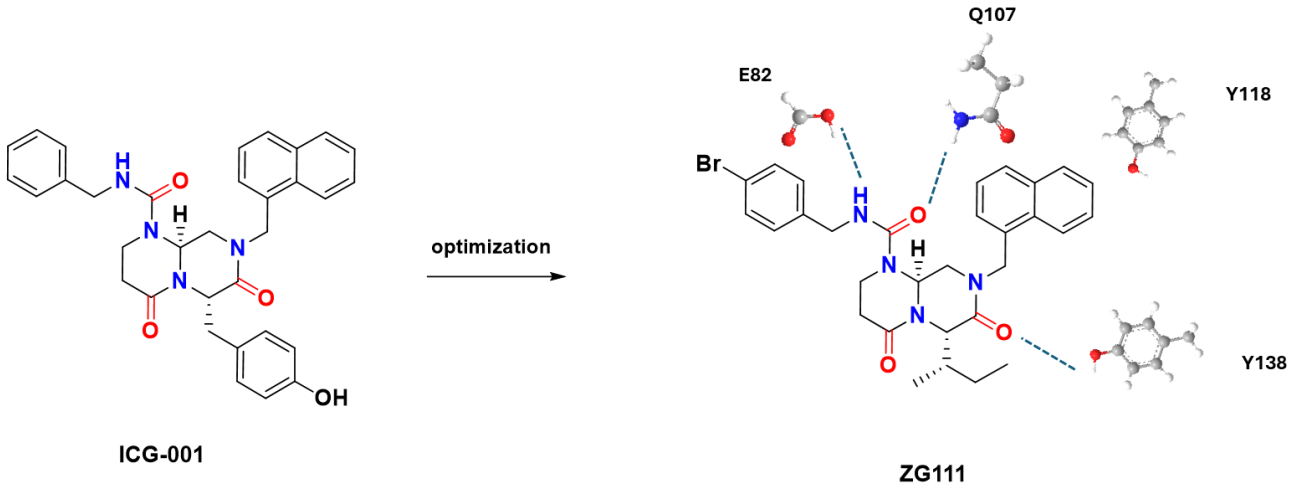

Figure 26. Chemical optimization of **ICG-001** and **ZG11** with interactions with key amino acids in the allosteric site.

Based on the data obtained during the optimization process of **ZG111**, an extensive study of the structure-activity relationship (SAR) of the diacylpyrimide core was carried out, leading to the compound **ZG36** (Figure 27), with an EC_{50} of 0.54 μM. SAR revealed the importance of the nitrogen atom of the ureide portion which, as with **ZG111**, interacts with an E82 residue. Linked to this ureidic portion is a 4-bromobenzyl, which once again highlights the hydrophobic effect of the aromatic ring that interacts with the lipophilic residues R78, L79, E82, L104, F105, and S108, whose bond is further stabilized by the electron-withdrawing effect of bromine. The carbonyl functionality in the cycle interacts with Y138, and in this region, the greatest activity was observed with the sec-butyl. Finally, on the naphthyl ring, which interacts with I100, L104, Y118, Y138, W146 of the hydrophobic region, a methoxy group was inserted, resulting in greater affinity due to increased hydrophobic interactions and the establishment of additional interactions with Y118 and I84 not present in the less active compound. These interactions were identified using the **ZG36** *h*ClpP complex (PDBID: 8I7X) with a resolution of 1.99Å[159].

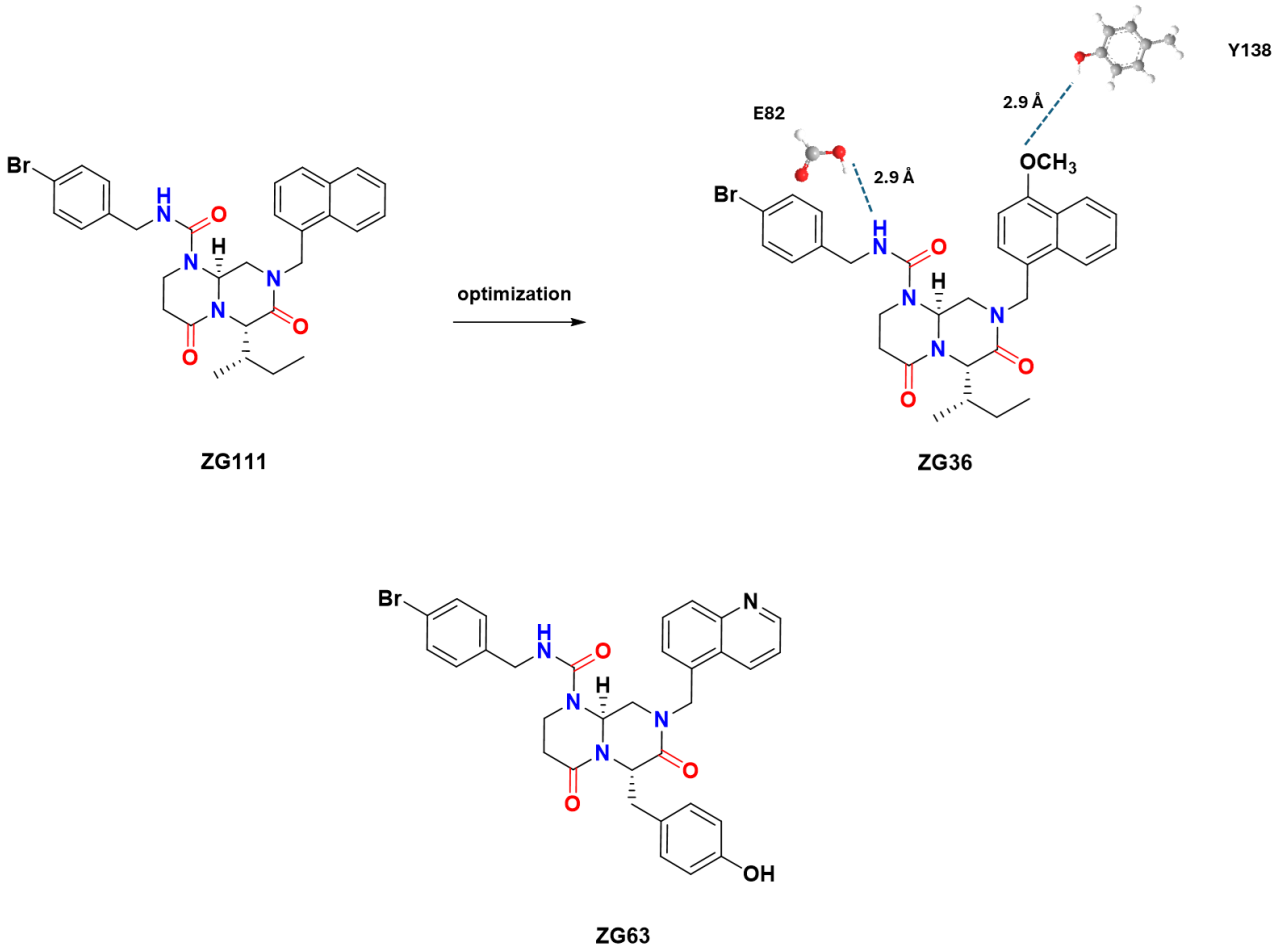

Figure 27. Structure optimization leading to **ZG36** and its interactions with *h*ClpP (PDBID: 8I7X). Chemical structure of **ZG63** (EC_{50} > 100 µM)

ZG180 (Figure 28) also belongs to this class of compounds with an *h*ClpP EC_{50} = 5.4 µM, making it less active than the others, but its analysis has allowed us to identify another characteristic of *h*ClpP compared to bacterial *Sa*ClpP. Unlike **ZG36** and **ZG111**, this compound has a 4,4,4-trifluorobutyl instead of the 4-bromobenzyl[160]. This highlights the importance of the presence of strong electron-withdrawing groups but also that a chain extension, even with lower activity, allows the protease to be activated in the same way, indicating the presence of a rather large

hydrophobic pocket. This compound was used as a starting point to identify a compound that was selective for *Sa*ClpP over *h*ClpP so that it could be used for its antibacterial effect.

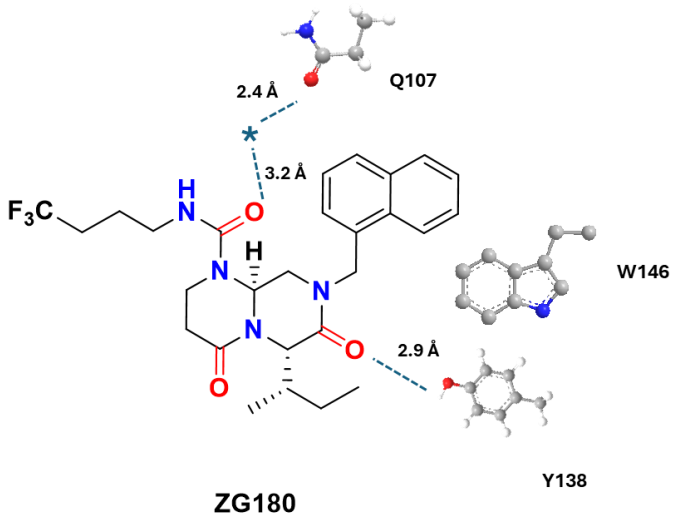

Figure 28. ZG180 interactions with key amino acids in the allosteric site of *h*ClpP.

ZG197 was identified by inserting a methyl group on the carbon in alpha to naphthyl (Figure 29). The group was inserted in an area where interaction occurs with the large side chain of a W146 (*h*ClpP), establishing a steric hindrance that led to a loss of activity that was not observed in the bacterial form where W146 is replaced by a less hindered I91 residue. This was confirmed by analyzing the (*R*)- and (*S*)-**ZG197** forms, in which it was observed that in the (*S*) form, the naphthyl group inserts in the opposite direction to the (*R*) form and **ZG180**, creating a steric hindrance that makes this form completely inactive towards human ClpP. However, in the (*R*) form, there is a significant reduction in EC_{50} = 31.5 µM activity due to the presence of the methyl group, which influences the plasticity of the naphthyl in fitting properly into the enzyme hydrophobic pocket[160].

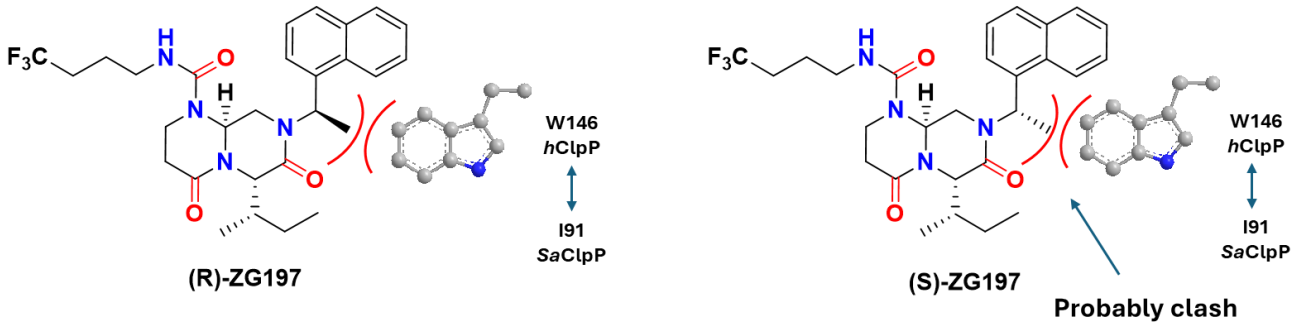

Figure 29. Chemical structures of **(R)** and **(S)- ZG197** highlighting the W146 residue of *h*ClpP and the groups that, due to steric hindrance, confer selectivity towards bacterial ClpP.

ZK53

The interactions of **ZK53** (Figure 30) were identified by analyzing the complex with *h*ClpP. This compound, which has an EC_{50} = 0.22 μM, was identified by optimizing the compound **ZK111**, which has an EC_{50} = 0.45 μM. By resolving the crystal structure, it was possible to identify that the hydrophobic interactions of the pendants, which constitute the pincer structure, are essential for stabilizing the bond with the protease. In particular, the interaction of the 3,5-difluorobenzyl ring establishes π-π interactions with W146, increasing selectivity towards human ClpP compared to bacterial ClpP, in which I91 (*Sa*ClpP) is present instead of W146 (Figure 30). These hydrophobic interactions are essential and selective for structures with simpler central scaffolds and not for more complex structures such as **ADEP**. The 4-bromobenzyl ring establishes further hydrophobic interactions with V148, L170, and the alkyl side chains of I84, L79, and E82. The amino nitrogen atom of the central nucleus establishes interactions with the side chain of Y118, while the ureidic nitrogen outside the ring forms a water-mediated H-bond with Q107[129].

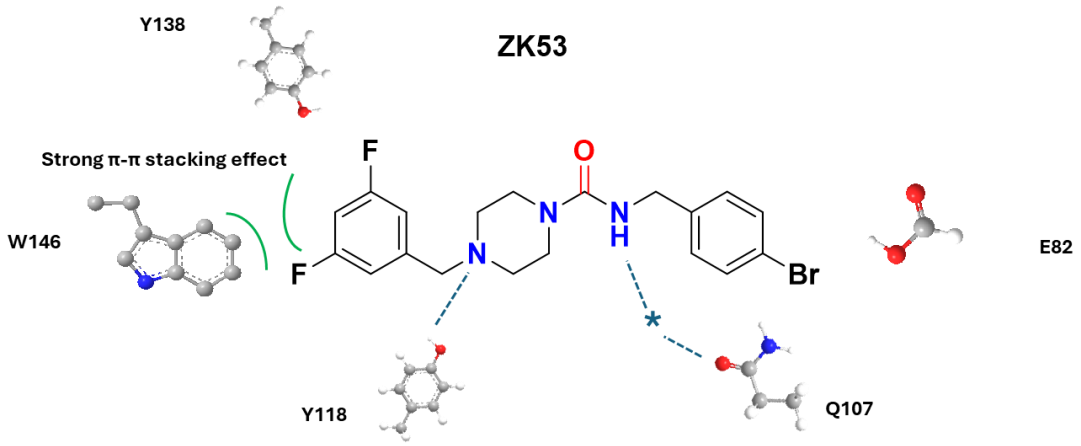

Figure 30. Chemical structure of **ZK53** with interactions with key amino acids in the allosteric site. In this case, the position of the 3,5-difluorobenzyl ring establishes π-π interactions with W146, increasing selectivity toward human ClpP compared to bacterial ClpP.

Chapter 2. Results and Discussion

2.1. Rational design of piperazines

The aim of this work was to identify a new chemical scaffold more easly to prepare activator of *h*ClpP. This was achieved through careful structural analysis of already known protease activators. Subsequently, based on the results obtained, a structural simplification process was implemented, leading to the 1,4-piperazine-2-one scaffold.

In a previous work, starting from the **TR-57**, two new series of compounds (**THX** and **THY**) were designed using the **THPPD** scaffold as a prototype (Figure 31). Through an extensive study of structure-activity relationships (SAR), it was found that benzyl substituents influence *h*ClpP activity, cytotoxicity in patient-derived DIPG cell lines, and cellular fatty acid profiles. Among these, the most promising compound, **THX6** (EC_{50} = 1.18 µM), alters the levels of proteins considered essential in mitochondrial processes, such as oxidative phosphorylation, organelle biogenesis, and mitophagy, highlighting that its anti-cancer effect is mainly related to the inhibition of mitophagy[2].

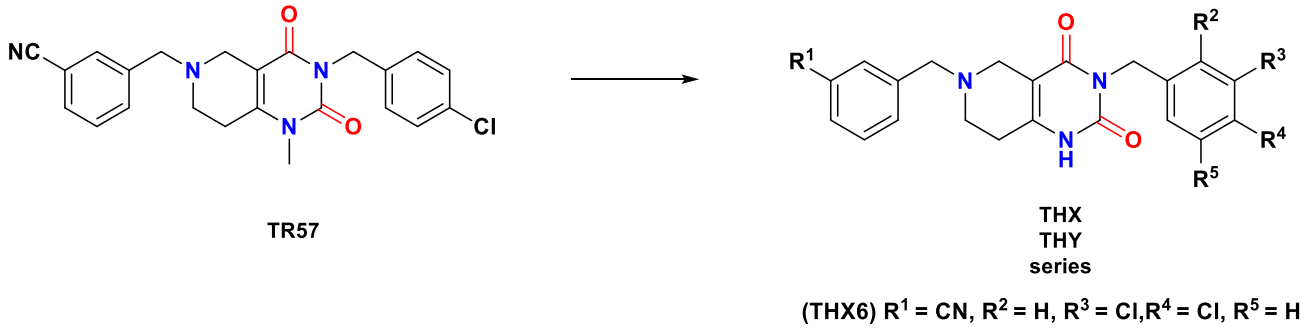

Figure 31. Chemical structure of **TR-57** and the new series **THX** and **THY**.

By analyzing the interaction modes of the main allosteric activators reported in the literature, through the study of their complex crystals, it was possible to identify the main interactions inside the protease. This analysis led to the rational design of a new scaffold able to establish strong interactions with the enzyme allosteric site and thus further increase its proteolytic activity in their

presence. By analyzing the activators, it is possible to observe a structural overlap. A variable flexible central core is identified in the **ONC201**, **THPPD**s, **ZG36**, and **ZG111**, consisting of a cyclic structure in which nitrogenous heterocycles are recurrent, as it has been observed that the nitrogen atom plays a crucial role in establishement interactions with the amino acids present in the allosteric site of *h*ClpP. However, this scaffold can be simpler, as in **ZK53**, which again contains a nitrogen heterocycle. **ONC201** and **THPPD**s have nitrogen atoms in the 1,3-position of an "unsaturated" piperidine, unlike **ZK53**, in which the nitrogen atoms are in 1,4-position of a "saturated" piperazine with an exocyclic carbonyl. Three essential interactions with Q107, Y118, and E82 were also identified, which stabilize the bond with the protease *via* H-bonding. The terminal amide or carbonyl of Q107 is involved in the bond as an acceptor or donor of H-bonding with an endocyclic carbonyl as in **ONC201**, **THX6**, or with the exocyclic function that is part of a ureidic function as in **ZG111**, **ZG36**. Only in compound **ZK53** does the interaction occur with the nitrogen atom of the exocyclic ureidic moiety. There is a non-planar piperidine or piperazine nitrogen atom that establishes interactions with Y118, except for the **ZG** series, in which the steric hindrance of the substituents causes the endocyclic carbonyl to interact with Y138, which is usually involved in establishing predominantly hydrophobic interactions. The interaction with E82 is the most variable. In fact, the side chain of E82 can interact with an imidazole nitrogen atom as in **ONC201**, or with an additional carbonyl of the **THPPD** bicyclic ring (such as **THX6**), which in this case stabilizes the interaction with the protease compared to compounds in which it is not present. However, the charged carboxyl of glutamic acid can also give rise to anion-π interactions with the aromatic rings that constitute one of the pendants of the pincer structure. This is possible for the presence of electron-withdrawing substituents in the structures of the most potent activators, as they partially deactivate the ring, making it positively charged and allowing ionic interaction in addition to the classic hydrophobic interaction. X-ray crystallographic analysis has identified another amino acid, W146, as the element for developing activators selective for *h*ClpP compared to *Sa*ClpP. When bulky groups as the terminal indole are inserted, even just a methyl group as in **ZG197**, in positions

adjacent to tryptophan, this determines selectivity towards the bacterial isoform in which I96 is present instead of W146. However, as in **ZK53**, the presence of nonpolar functions adjacent to W146 stabilizes the bond with the human isoform thanks to a strong π-π stacking effect (Figure 32).

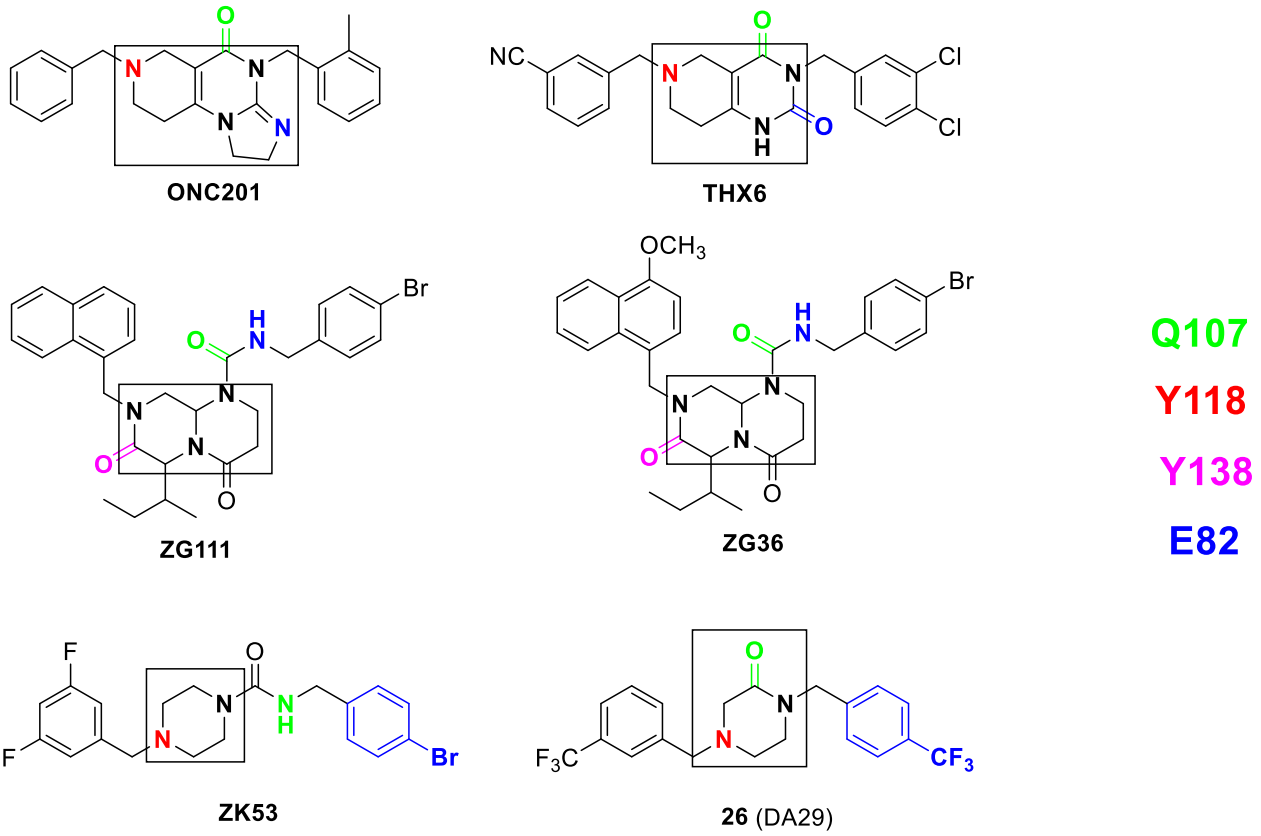

Figure 32. ClpP activators structure, highlighting the central scaffold and the main groups that interact with Y118, Y138, Q107, and E82.

Based on these features, a saturated ring bearing the two nitrogen atoms in the 1,4-position was designed, yielding simplified scaffolds based on piperazine, piperazine-1-one (exocyclic carbonyl), piperazine-1,4-dione (exocyclic carbonyls), piperazine-2-one (endocyclic carbonyl), and piperazine-2,5-dione (endocyclic carbonyls) (Figure 33), incorporating endo- or exo-cyclic carbonyl(s) but avoiding the pseudo-ureidic moiety of **ZK53**[2]**.**

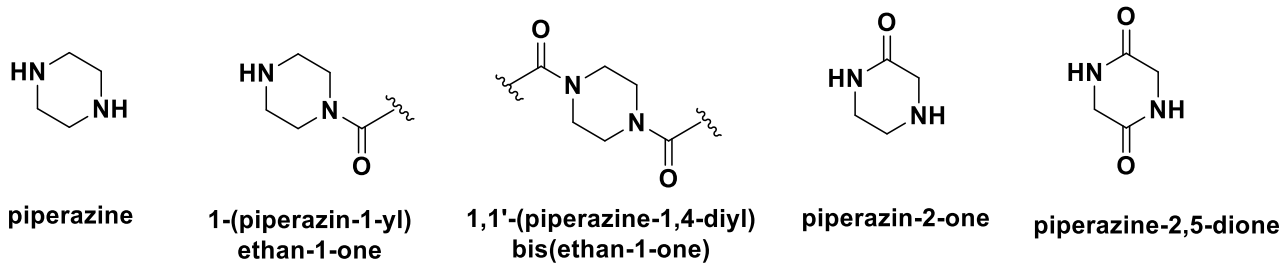

Figure 33. Core scaffolds of piperazine, piperazine-1-one (exocyclic carbonyl), piperazine-1,4-dione (exocyclic carbonyls), piperazine-2-one (endocyclic carbonyl), and piperazine-2,5-dione (endocyclic carbonyls). The endocyclic carbonyl has a carbonyl carbon atom that is part of the piperazine cycle; the exocyclic carbonyl has a carbonyl carbon atom outside the piperazine cycle.

2.1.1. Mapping allosteric site for drug development

The rational design of piperazines was carried out by incorporating, during the construction of the scaffold, substituents selected based on the structural features of the known activators, with the aim of ensuring effective interactions with Y118, Q107 and E82, the three amino acid residues considered essential for protein activation. The simple piperazine scaffold without any carbonyl did not activate ClpP at concentrations up to 100 μM as evaluated by a cell-free fluorimetric assay. A further modification of the piperazine was accomplished to improve interactions with the enzyme, based on the essential contacts established for **ONC201** and **ZK53** within the allosteric binding site of *h*ClpP.

Analysis of the *h*ClpP:TR-57 complex (PDBID: 7UVN) revealed the essential structural features that allow THPPDs to act as activators of *h*ClpP (Figure 19). These compounds possess a central planar heterocycle, deficient in electrons, and two benzyls that establish π-π hydrophobic interactions within the allosteric site. Their binding promotes ClpX dissociation, ClpP tetradecamer stabilization, and axial pore widening.

In addition, several hydrogen bonding interactions are critical for stabilization: the nitrogen atom of tetrahydropyridopyrimidinone (**THPPD** and **TR-57**) forms a hydrogen bond with the hydroxyl group of Y118, while the carbonyl forms a water-mediated hydrogen bond with the terminal amide of glutamine Q107. An additional hydrogen bond involves the carboxyl of glutamic acid (E82), which interacts with the imidazole nitrogen atom of **ONC201** and related imipridones. In derivatives with a tetrahydropyridopyrimidinone nucleus, such as **TR-57**, the same carboxyl E82 interacts instead with a second carbonyl group in the bicyclic structure, which stabilizes the interaction within the allosteric site (Figure 34).

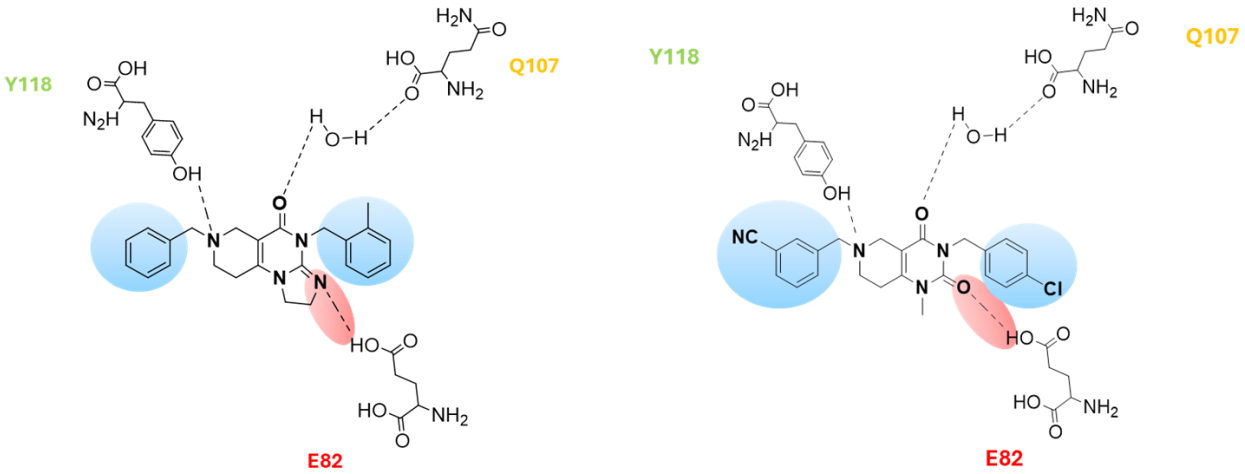

Figure 34. Main interactions of *h*ClpP with **ONC201** (left) and **TR-57** (right). In **ONC201**, the carboxyl of E82 interacts with the imidazole nitrogen atom, whereas in **TR-57** the same residue interacts with a carbonyloxygen aatom. These specific interactions are highlighted in red and light blue.

The benzyls are located within two lateral hydrophobic pockets, containing L79, L104, and F105. Additionally, there is a series of aromatic amino acids, including Y118, Y138, and W146, which collectively determine the ligand positioning in a "U-like" conformation (pincer topology) (Figure 35).

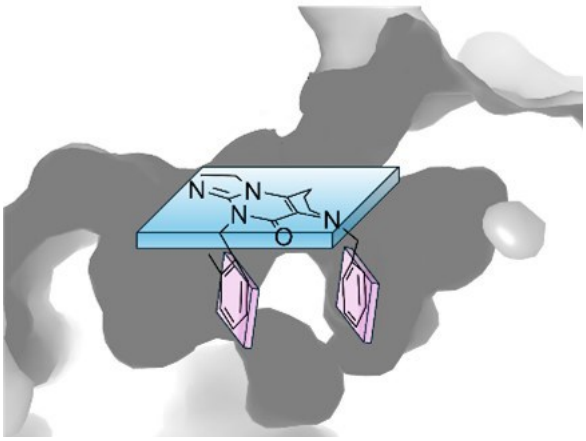

Figure 35. ONC201 in the U-shaped conformation (pincer topology).

Based on the finding that simpler compounds such as **ZK53**, than **ONC201** and THPPDs, still act as *h*ClpP activators while maintaining the essential characteristics for activity, we initiated a deeper structure-activity relationship study using piperazine-based scaffolds.

2.2. Chemistry

The synthesis of piperazines (Scheme 1) **1** (DA1) and **2** (DA4) was performed by reacting the commercially available piperazine with the corresponding 4-chlorobenzyl bromide or 3-cyanobenzyl bromide, respectively, in the presence of K_2CO_3 (2.5 equivalents); similarly, the monosubstituted piperazine **3** (DA2) was prepared using a smaller amount of K_2CO_3 (1.3 equivalents). Piperazine treated with the appropriate benzoyl chloride, in turn prepared from the corresponding benzoic acid and $SOCl_2$, afforded the mono-benzoylpiperazines **5** (DA13) and **6** (DA16), and the 1,4-dibenzoylpiperazine **7** (DA12) and **8** (DA15). Finally, 3-(4-(4-chlorobenzoyl)piperazine-1-carbonyl)benzonitrile (**9**, DA17) was obtained by reacting 3-(piperazine-1-carbonyl)benzonitrile (**6**, DA16) with 1.5 equivalents of 4-chlorobenzoyl chloride.

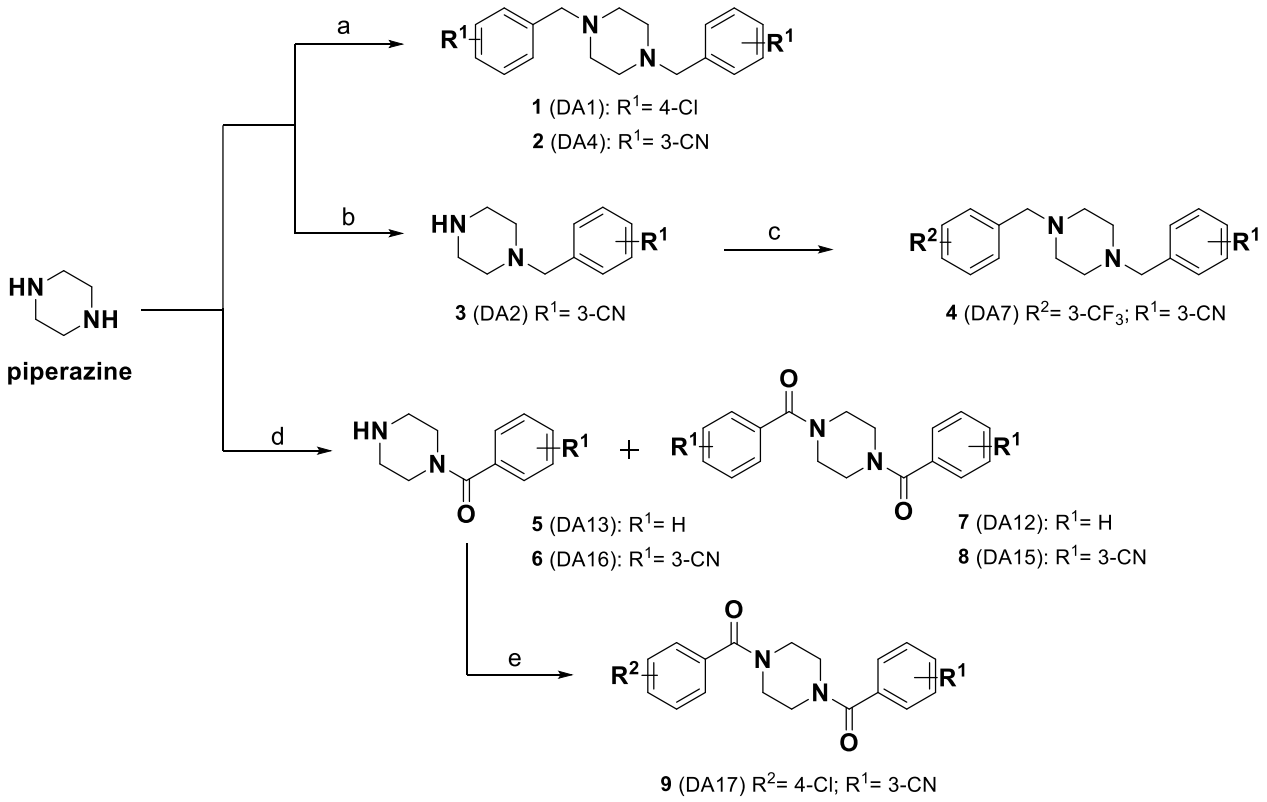

SCHEME 1. *Reagents and conditions*: **A**) a) aryl bromide, K_2CO_3 (2.5 eq), CH_3CN, r.t., 2h; b) 4-chlorobenzyl bromide or 3-cyanobenzyl bromide, K_2CO_3 (1.3 eq), CH_3CN, r.t., 2h; c) 3-trifluoromethylbenzyl bromide, K_2CO_3 (1.3 eq), CH_3CN, r.t., 2h; d) benzoyl chloride or 3-cyanobenzoyl chloride (1 eq), absolute EtOH, 0 °C, r.t., overnight; e) 4-chlorobenzoyl chloride (1.5 eq), absolute EtOH, 0 °C, r.t., overnight.

The commercial 2-oxopiperazine (piperazine-2-one) was treated the appropriate benzyl bromide in dry DMF in the presence of NaH, to obtain the symmetric substituted oxopiperazines **10**-**16**. Monosubstituted derivatives **17**-**20** were obtained by reacting 2-oxopiperazine, in the presence of the weaker base $NaHCO_3$, with the appropriate benzyl bromide. **17-20** treated with the corresponding substituted-benzyl bromide in dry DMF in the presence of NaH, allowed the synthesis of **21**-**27** (Scheme 2). Compound **31** (DA45) was prepared starting from 2-oxopiperazine *N*-Boc protected **28** (DA41), in turn converted into **29** (DA43) by reacting with 4-trifluormethylbenzyl bromide, the later then converted into **30** (DA44) after deprotection of **29** (DA43) **30** (DA44) reacted with 2-(3,4-dichlorophenyl)acetyl chloride to afford **31** (DA45) (Scheme 2).

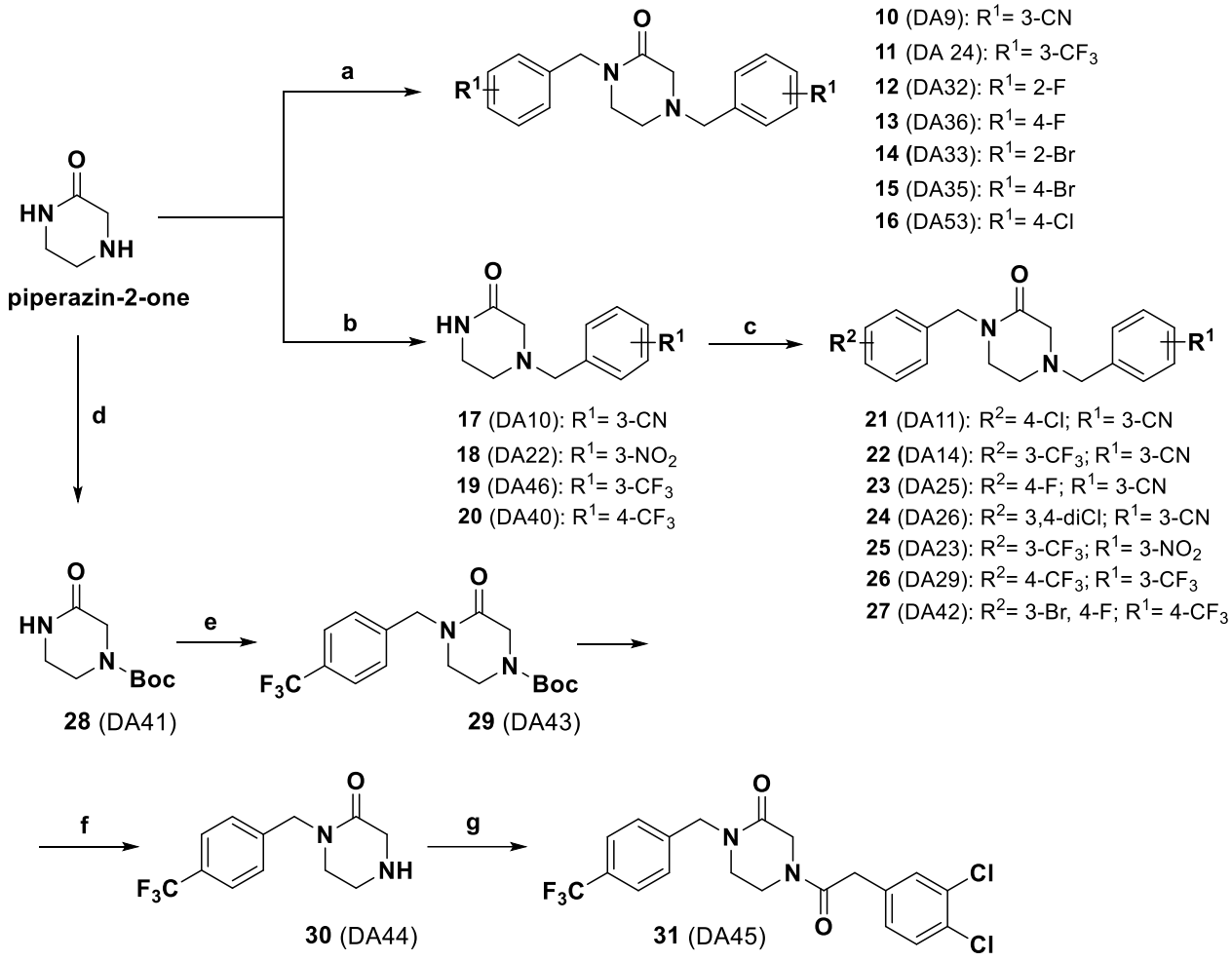

SCHEME 2. *Reagents and conditions*: a) substituted-benzyl bromide, NaH, anhydrous DMF, 0 °C for 30 min, 50 °C, overnight; b) substituted-benzyl bromide, $NaHCO_3$, anhydrous DMF, 100 °C, overnight; c) substituted-benzyl bromide, NaH, anhydrous DMF, 0 °C for 30 min, 50 °C overnight; d) di-*tert*-butyl decarbonate, CH_2Cl_2, 0 °C to r.t., 3h; e) substituted-benzyl bromide, anhydrous DMF, NaH, 0 °C, 30 min, 50 °C, overnight; f) CF_3CO_2H, CH_2Cl_2, r.t., 5h; g) 2-(3,4-dichlorophenyl)acetyl chloride, CH_2Cl_2, r.t. overnight.

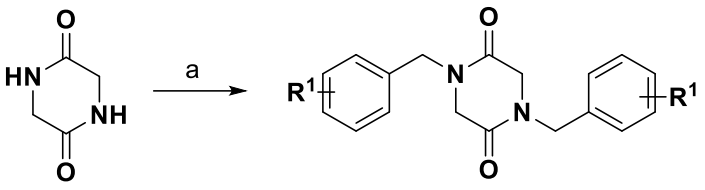

piperazine-2,5-dione

32 (DA28): R^1= H
33 (DA34): R^1= 3-CF_3

SCHEME 3. *Reagents and conditions*: a) substituted-benzyl bromide, NaH, anhydrous DMF, 30 min, r.t., 16h.

33 (DA28) and **34** (DA34) were prepared by reacting the piperazine-5,6-dione (**32**) with benzyl bromide and 3-cyanobenzyl bromide, respectively, in anhydrous conditions and in the presence of NaH (Scheme 3). **36** (DA5) and **37** (DA6) were prepared in good yields by reacting the 1-(piperazin-1-yl)ethan-1-one (**35**) and 4-chlorobenzyl bromide or 4-cyanobenzyl bromide, respectively, in the presence of K_2CO_3 (Scheme 4).

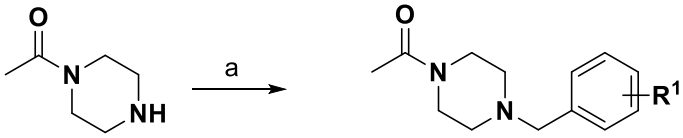

35

36 (DA5): R1= 4-Cl
37 (DA6): R^1= 4-CN

SCHEME 4. *Reagents and conditions*: a) substituted-benzyl bromide, K_2CO_3, CH_3CN, r.t., 2h.

2.3. Biology

2.3.1 Evalutation of human ClpP activation rate

The new piperazines were designed to enable interactions with key *h*ClpP residues, aiming to reproduce the typical U-shaped conformation with two benzyls positioned in the hydrophobic pockets (Figure 35). As a preliminary step, precursors bearing only one benzyl were tested for their ability to enhance *h*ClpP proteolytic activity evaluated using a fluorimetric cell-free assay based on the cleavage of FITC-labeled casein substrate, with activity monitored as an increase in fluorescence intensity over time. Compounds **5** (DA13), **6** (DA16), **36** (DA5), and **37** (DA6), considered precursors of **ZK53** with an exocyclic carbonyl, and compound **17** (DA10), with an endocyclic carbonyl as in **THX6**[2], were evaluated. All showed low potency as *h*ClpP activators, with EC_{50} values >100 μM and *h*ClpP activation in the range 0-13% (Figure 36).

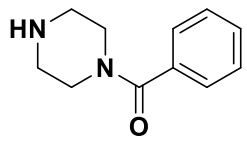

5 (DA13)

*h*ClpP EC_{50} > 100 μM
activity at 100 μM = 0%

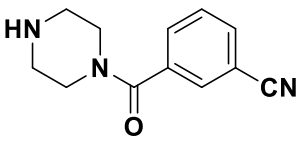

6 (DA16)

*h*ClpP EC_{50} > 100 μM
activity at 100 μM = 6%

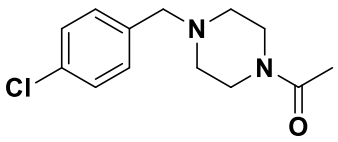

36 (DA5)

*h*ClpP EC_{50} > 100 μM
activity at 100 μM = 9%

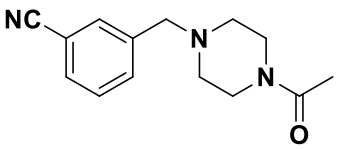

37 (DA6)

*h*ClpP EC_{50} > 100 μM
activity at 100 μM = 6%

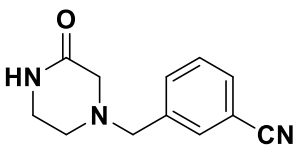

17 (DA10)

*h*ClpP EC_{50} > 100 μM
activity at 100 μM =

Figure 36. Some precursors of the target compounds bearing only one benzyl.

In the series of piperazines lacking the carbonyl(s), either endo- or exocyclic such as **1** (DA1), **2** (DA4), and **4** (DA7), only weak *h*ClpP activation was observed (EC_{50} >100 μM, 9-27% activation at 100 μM; Scheme 1, Table 1). This low activity is attributed to the absence of carbonyl-mediated interaction with residue Q107, as seen in imipridones (i.e. **ONC201**), **TRs**, and **THPPDs** (Figure 19 and 34). Nonetheless, residual activity may result from preserved interactions of the two piperazine nitrogen atoms with E82 and Y118, together with the contribution of benzyl substituents bearing electron-withdrawing groups (EWG) (mild EWG effect from chlorine, strong EWG effect from cyano group) (Figure 37).

To strengthen the binding force with the enzyme, a carbonyl external to the piperazine core was introduced. Piperazines **7 (**DA12), **8 (**DA15) and **9 (**DA17) were obtained; EC_{50} > 100 μM and 9-11 % activation at 100 mM were found for all the three compounds. These results clearly showed that the carbonyl must be endo-cycle at least for these compounds, despite **ZK53** having an exocyclic carbonyl.

To further eluacidate the role of carbonyls, new derivatives were designed with a 2-oxopiperazine core, where the carbonyl at position 2 interacts with residue Q107. But this interaction seems not enough to sustain *h*ClpP proteolytic activity: compound **10** (DA9) showed EC_{50} > 100 μM likely due to the cyano substituent on the left benzyl rendering the phenyl electron-poor and unable to establish strong π-π interactions. By contrast, compound **11** (DA24) achieved a significant increase in *h*ClpP-mediated hydrolysis, with 85% activation and an EC_{50} = 12 ± 5.15 μM. In this series, the proteolytic activity was strongly affected by the substituents on the aromatic moieties of the two benzyl groups, increasing with electron-withdrawing effects, particularly on the right-hand benzyl, which favored anchoring within the hydrophobic pockets (Figure 37).

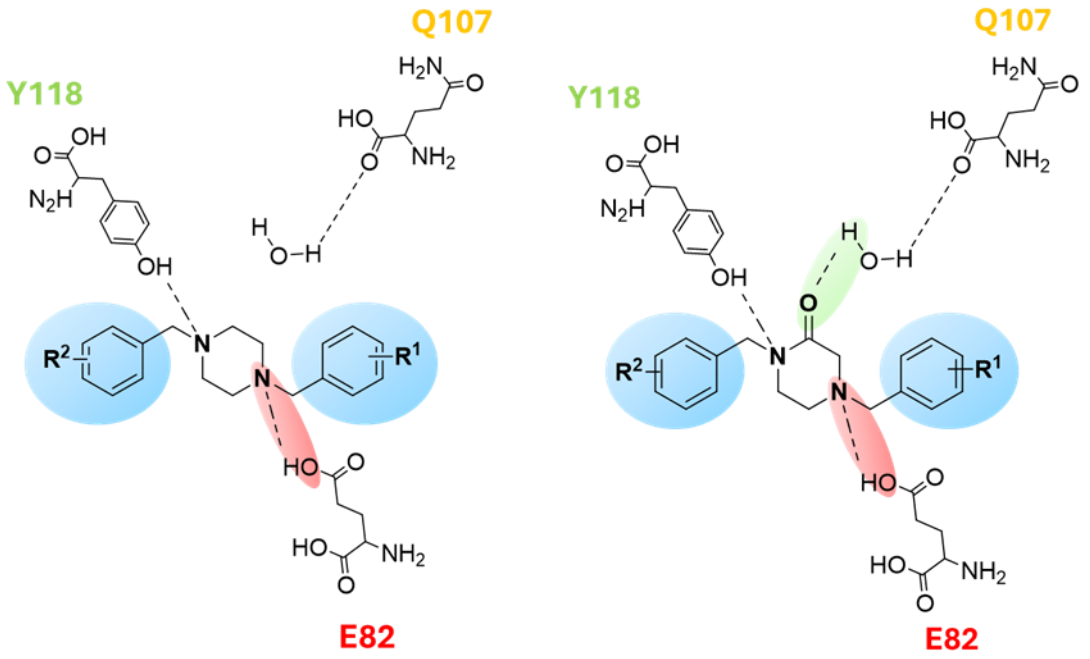

Figure 37. On the left there are piperazine-core interactions, where the interaction with Q107 is lost; on the right, there are dibenzyl 2-oxopiperazine derivatives where the carbonyl interaction with Q107 is restored.

No halogen effect was observed for fluoro- and chloro-substituted compounds **12** (DA32), **13** (DA36), **14** (DA33) and **16** (DA53) having EC_{50} >100 µM. In contrast, the effect of bromine depended on its position: *ortho* substitution increased activity by 24% at 100 mM, while *para* substitution markedly enhanced activation to 91% at the same concentration [EC_{50} = 6.08 µM for **15** (DA35)]. Introducing the cyano or nitro group (very strong EWG) on the right benzyl ring yielded new activators [**21** (DA11), **22** (DA14), **23** (DA25), **24** (DA26) and **25** (DA23)], with EC_{50} values of 15-30 µM. The most potent compound, **26** (DA29), combined a 3-CF_3 substituent on the right benzyl with a 4-CF_3 on the left, achieving EC_{50} = 0.85 ± 0.14 µM. However, replacing the 3-CF_3 with two halogens (3-Br, 4-F) abolished activity (EC_{50} >100 µM), even when incorporated into a piperazine-2-one [**27** (DA42)] or a piperazine-2-one bearing an additional exocyclic carbonyl [**31**

(DA45)]. Similarly, derivatives with a second endocyclic carbonyl [**33** (DA28), **34** (DA34)] remained inactive (EC_{50} >100 µM).

Table 1. EC_{50} (µM) and percentage activation values (%) of *h*ClpP of the dibenzylpiperazines, determined by a fluorimetric cell-free assay based on the cleavage of FITC-labeled casein substrate.

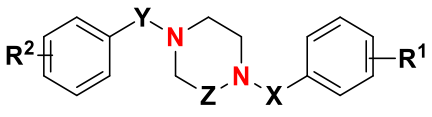

Compd	Z	X	Y	R^2	R^1	*h*ClpP EC_{50} (µM)[a] (% activation at 100µM)
1 (DA1)	CH_2	CH_2	CH_2	4-Cl	4-Cl	>100 (9)
2 (DA4)	CH_2	CH_2	CH_2	3-CN	3-CN	>100 (19)
4 (DA7)	CH_2	CH_2	CH_2	3-CF_3	3-CN	>100 (27)
7 (DA12)	CH2	CO	CO	H	H	>100 (0)
8 (DA15)	CH_2	CO	CO	3-CN	3-CN	>100 (11)
9 (DA17)	CH_2	CO	CO	4-Cl	3-CN	>100 (15)

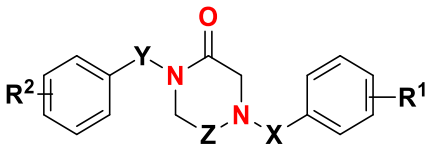

Compd	Z	X	Y	R^2	R^1	*h*ClpP EC_{50} (µM)[a] (% activation at 100µM)
10 (DA9)	CH_2	CH_2	CH_2	3-CN	3-CN	>100 (28)
11 (DA24)	CH_2	CH_2	CH_2	3-CF_3	3-CF_3	12 ± 5.15 (85)
12 (DA32)	CH_2	CH_2	CH_2	2-F	2-F	>100 (15)
13 (DA36)	CH_2	CH_2	CH_2	4-F	4-F	>100 (43)
14 (DA33)	CH_2	CH_2	CH_2	2-Br	2-Br	>100 (24)
15 (DA35)	CH_2	CH_2	CH_2	4-Br	4-Br	6.08 ± 0.51 (91)
16 (DA53)	CH_2	CH_2	CH_2	4-Cl	4-Cl	>100 (14)
21 (DA11)	CH_2	CH_2	CH_2	4-Cl	3-CN	15 ± 0.68 (63)

22 (DA14)	CH_2	CH_2	CH_2	3-CF_3	3-CN	30 ± 0.15 (58)
23 (DA25)	CH_2	CH_2	CH_2	4-F	3-CN	22 ± 9.01 (43)
24 (DA26)	CH_2	CH_2	CH_2	3,4-diCl	3-CN	14 ± 2.81 (57)
25 (DA23)	CH_2	CH_2	CH_2	3-CF_3	4-NO_2	20 ± 1.22 (65)
26 (DA29)	CH_2	CH_2	CH_2	4-CF_3	3-CF_3	0.85 ± 0.14 (95)
27 (DA42)	CH_2	CH_2	CH_2	4-CF_3	3-Br, 4-F	>100 (18)
31 (DA45)	CH_2	$COCH_2$	CH_2	4-CF_3	3,4-diCl	>100 (24)
33 (DA28)	CO	CH_2	CH_2	H	H	>100 (28)
34 (DA34)	CO	CH_2	CH_2	3-CF_3	3-CF_3	>100 (13)

[a]EC_{50} values are presented as means ± SEM from at least 3 independent experiments, each performed in triplicate. The drug-stimulated proteolytic activity of *h*ClpP was evaluated using a fluorimetric assay based on the cleavage of FITC-labeled casein substrate, with activity monitored as an increase in fluorescence intensity over time.

2.3.2. Evalutation of dopaminergic activity by dibenzylpiperazine

Since **ONC201** is a dopamine receptor antagonist and ClpP activator, and following the emerging implication of the dopaminergic system in tumor onset, selected compounds [**9** (DA17), **11** (DA24), **12** (DA32), **14** (DA33), **15** (DA35), **16** (DA53), **26** (DA29), **27** (DA42), **31** (DA45), **33** (DA28), and **34** (DA34)] were evaluated for their ability to interact with dopamine receptors. All the tested showed negligible affinity for dopamine D2 and D3 receptors (Ki >10,000 nM, Appendix Table S1). By contrast, **ONC201** binds *h*D2R and *h*D3R with Ki values of 14.8 ± 1.40 μM and 4.09 ± 0.69 μM, respectively, consistent with its dual mechanism of *h*ClpP activation and dopamine receptor antagonism[2]. These results confirm that the tested compounds selectively target *h*ClpP with minimal off-target activity on D2-like receptors (Appendix Table S1). The crystal structure (PDBID: 8HGK), FLAP and Autodock Vina analyses showed that **26** (DA29) binds in a mode comparable to **ZK53**, engaging, Y118, V145 and W146 with enhanced interactions and a more favorable binding energy (-10.3 vs -9.3 kcal/mol, Appendix Figure S1).

2.3.3. *h*ClpP:26 (DA29) complex structural analysis by X-ray

Following the hypotheses of interactions between the synthesized compounds, the interactions between **26** (DA29) and *h*ClpP were validated, the X-ray structure of the *h*ClpP:**26** (DA29) complex was determined at 2.78Å. Crystallographic data collection and refinement statistics are shown in **Table 2**.

Table 2. Data collection and refinement statistics for *h*ClpP bound with **26** (DA29)*.

PDBID	9Z3C
Wavelength	0.979338
Resolution range	34.41 - 2.781 (2.84 - 2.78)
Space group	C 1 2 1
Unit cell	170.061 121.139 100.826 90 116.58 90
Total reflections	332548
Unique reflections	46004 (2866)
Multiplicity	7.2
Completeness (%)	99.95 (99.90)
Mean I/sigma(I)	7.1
Wilson B-factor	39.83
R-merge	0.296
R-meas	0.347
R-pim	0.179
CC1/2	0.977
CC*	0.994
Reflections used in refinement	46004 (2866)
Reflections used for R-free	2307 (150)
R-work	0.1898 (0.3009)
R-free	0.2407 (0.3657)
Number of non-hydrogen atoms	9818
macromolecules	9479
ligands	209
solvent	130
Protein residues	1223
Nucleic acid bases	0
RMS (bonds)	0.002
RMS (angles)	0.51
Ramachandran favored (%)	95.94
Ramachandran allowed (%)	4.06
Ramachandran outliers (%)	0
Rotamer outliers (%)	0.67

Clashscore	3.25
Average B-factor	40.04
macromolecules	40.01
ligands	43.49
solvent	37.04

*Statistics for the highest resolution shells are found in parentheses.

*h*ClpP crystallized as a tetradecamer with fourteen **26** (DA29) molecules bound in the hydrophobic pockets at subunit interfaces (Figure 38A, B). The complex adopts an open pore compact conformation consistent with previously reported *h*ClpP structures bound with activators (e.g. **ONC201**, **ZK53, TR-57**)[129,143,157]. In the apo state, the flexible *N*-terminal regions cover the axial pore of *h*ClpP restricting substrate access to the catalytic chamber. Upon agonist binding, these loops undergo ordering into a collar of β-hairpins that results in pore widening[117,161]. In the **26** (DA29)-bound structure, crystal packing prevented full resolution of the *N*-terminal loops however partially resolved chains indicate a clear ordering of this region. The axial pore radius is widened to 26Å compared to the 13Å radius of the apo structure (PDBID: 1TG6)[143] (Figure 38A, B). The αE helices in the **26** (DA29)-bound structure are shortened from seven to five turns, indicating *h*ClpP crystalized in a compact state. This conformation is inactive due to the geometry of the catalytic triad. The H178 residue is oriented away from S153, breaking the hydrogen-bonding network needed for catalysis, and is instead rotated toward D227 (Figure 38C).

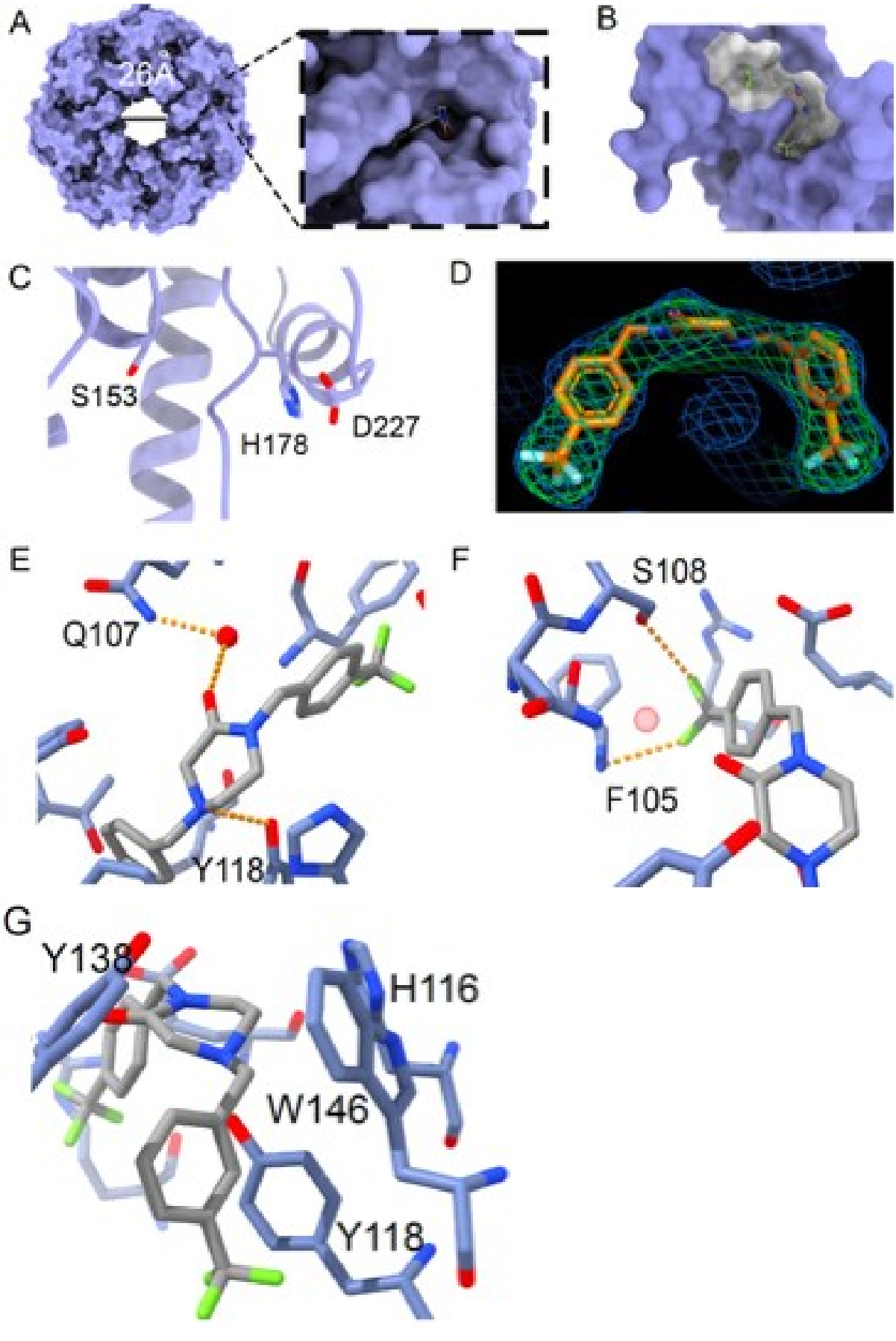
A
28 Å
B
C
S153
H178
D227
D
E
Q107
Y118
F
S108
F105
G
Y138
H116
W146
Y118

Figure 38. 26 (DA29) **binding *h*ClpP.** (**A**) Top view of *h*ClpP showing enlarged pore diameter and **26** (DA29) bound in all hydrophobic pockets. Inset shows an enlarged view of **26** (DA29) bound to the pocket. (**B**) **26** (DA29) adopts pincer (U-shaped) topology to dock into both cavities. (**C**) Geometry of the catalytic triad in **26** (DA29)-bound *h*ClpP**.** S153, H178, D227. (**D**) Electron density at the hydrophobic pocket; 2Fo-Fc maps are colored blue and contoured at 1.0σ, while composite omit maps are colored green and contoured at 1.8σ **E**, **F**, **G).** (**E**) Shown are interactions between **26** (DA29) (grey) and *h*ClpP (purple) highlighting the hydrogen bond interactions (yellow) with the piperazine-1-one ring. **(F)** Hydrogen bond interactions (yellow) with the para-substituted arm. (**G**) Hydrophobic and π-π interactions between the meta-substituted arm.

Continuous density for **26** (DA29) is evident in the H pocket 2Fo-Fc maps contoured at 1.0σ, with clear composite omit density at 1.8σ, supporting drug binding at the H pocket (Figure 38D). The H pocket is formed by two adjacent subunits in the apical domain of ClpP. **26** (DA29) adopts a pincer topology similar to **ONC201**, **THPPD** analogs and **ZG111**, with the eastern and western fragments extending into neighboring hydrophobic cavities in the H site (Figure 38B). The water mediated hydrogen bonding between the piperazine carboxyl and Q107 is present in eight of the fourteen binding pockets. The remaining six **26** (DA29) molecules are oriented in the same geometry, but with little to no electron density for the coordinated water. The interaction between Y118 and the piperazine ring is present in all 14 subunits (Figure 38E). However, the interaction occurs with the amide nitrogen atom rather than the ring amine hypothesized in Figure 37.

Both arms of **26** (DA29) feature a trifluoromethyl monosubstituted phenyl ring. The arm with the para substituted ring binds the hydrophobic groove closest to the *h*ClpP entrance pore while the arm with the meta substituted ring binds the groove further from the pore (Figure 38B), The para substituted arm forms hydrogen bonds between fluorine and the S108 sidechain, as well as the backbone amide of F105 (Figure 38F). The trifluoromethyl groups serve as a strong electron-

withdrawing group, deactivating the phenyl ring. Anion-π interactions can be found between the phenyl ring on one arm of DA29 and the negatively charged side chain of E82 The meta substituted trifluoromethyl group does not appear to participate in any hydrogen bonding. Rather this arm is held in place by π-π interactions with nearby aromatic residues H116, Y118, Y138, and W146. (Figure 38G).

2.3.4. Cellular thermal shift assay for assessing drug binding affinity to *h*ClpP

To evaluate the interaction of compound **26** (DA29) with *h*ClpP in Caco-2 cells, a cellular thermal shift assay (CETSA) was performed. Cells were incubated with 20 µM of **26** (DA29) for 1 h at 37°C, and the thermal stability of *h*ClpP was assessed by monitoring the soluble protein fraction across a temperature gradient using western blotting. Band intensities were normalized to the signal at 55 °C, set as 100%, and expressed as relative percentages for comparison. Treatment with **26** (DA29) markedly increased the thermal stability of *h*ClpP compared to the negative control **33** (DA28), confirming intracellular target engagement and corroborating the results of the cell-free enzymatic assay (Figure 39).

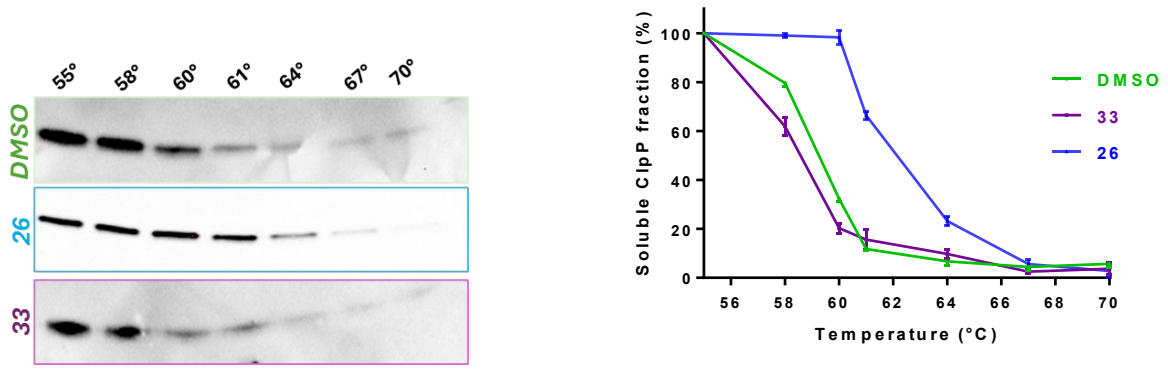

Figure 39. *h*ClpP thermal stability in Caco-2 cells treated with **26** (DA29), **33** (DA28), or DMSO (20 µM, 1 h), assessed by CETSA and normalized to T° = 55 °C.

2.3.5. Cytotoxicity in DIPG cell lines with different sensitivity to ONC201 and patient-derived tumor organoids (PDT-O)

Among the synthesized piperazines, only the most promising *h*ClpP activators **11** (DA24), **15** (DA35), **21** (DA11), **22** (DA14), **23** (DA25), **24** (DA26), **25** (DA23), **26** (DA29), and **33** (DA28),were tested to evaluate their potential antiproliferative activity on two DIPG patient-derived cell lines, SU-DIPG-36 (H3.1K27M) and SU-DIPG-50 (H3.3K27M) (Table 3). The compounds elicited distinct responses in the two models, highlighting differences in drug sensitivity. Notably, **24** (DA26) and **26** (DA29) were the most effective in SU-DIPG-36, with IC_{50} values of 7.8 μM (80% cell death) and 4.0 μM (86% cell death), respectively. In SU-DIPG-50, compound **26** (DA29) retained activity (IC_{50} = 11.6 μM, 69.1% cell death), whereas **24** (DA26) showed a remarkable reduced potency (IC_{50} = 41 μM, 57% cell death). Compound **11** (DA24) was active in both models, with slightly higher efficacy in SU-DIPG-36 (IC_{50} = 55 μM, 82.1% cell death at 100 μM) than in SU-DIPG-50 (IC_{50} = 15 μM, 68.1% cell death at 100 μM). Conversely, **21** (DA11), **23** (DA25), and **33** (DA28) displayed minimal cytotoxicity in both cell line, indicating weak engagement in essential survival pathways. Overall, similar to **ONC201**[2], the tested compounds showed greater efficacy in SU-DIPG-36 than in SU-DIPG-50 (considering the cell death percentage), underscoring the influence of the molecular subtype on therapeutic response.

Table 3. IC_{50} values in pediatric brain tumour-derived cell lines after 72 hours treatment with piperazines, assessed using CCK-8 cell viability assay.[a]

Compd	SU-DIPG-36 IC_{50} μM ± SEM (% inhibition at 100 μM)	SU-DIPG-50 IC_{50} μM ± SEM (% inhibition at 100 μM)
11 (DA24)	55 ± 6.25 (82.1)	15 ± 3.06 (68.1)
15 (DA35)	64.9 ± 5.28 (91)	46.8 ± 1.63 (73.5)
21 (DA11)	>100 (36)	72 ± 2.87 (64)
22 (DA14)	25 ± 2.51 (51)	75 ± 3.82 (53)
23 (DA25)	>100 (51)	>100 (22)
24 (DA26)	7.8 ± 0.56 (80)	41 ± 1.43 (57)
25 (DA23)	61 ± 2.93 (60)	>100 (53)

26 (DA29)	4.0 ± 1.20 (86)	11.6 ± 0.12 (69.1)
33 (DA28)	>100 (35)	>100 (26)
ONC201	37 ± 2.5 (82)	25 ± 12.3 (66)

[a]Data are expressed as the mean of three independent experiments and SEM values are reported.

To further validate the therapeutic potential of **26** (DA29) in a clinically relevant tumoral context, we assessed its cytotoxic efficacy in DIPG patient-derived tumor organoids (PDT-O). These 3D organoid models, established from fresh fine-needle biopsies, have been previously characterized and demonstrated to faithfully recapitulate the intratumorally heterogeneity, genetic landscape, and therapeutic responses of their original tumors[162].

Two distinct PDT-O lines, DMG2_O and DMG3_O, both harboring the H3.3K27M mutation, were treated with increasing concentrations of **26** (DA29) and reference compound **ONC201** in the range 0.1 – 100 µM. Dose-response curves revealed that **26** (DA29) reduced cell viability similarly to **ONC201** in both PDT-O models (Figure 40), with IC_{50} value of 2.57 ± 0.04 µM for **26** (DA29) compared to 2.23 ± 0.13 µM for **ONC201** in the DMG2_O model, and 1.94 ± 0.35 µM for **26** (DA29) compared to 1.11 ± 0.18 µM for **ONC201** in the DMG3_O model. Hence, **26** (DA29) demonstrated cytotoxic activity comparable to **ONC201** in clinically pertinent PDT-O models.

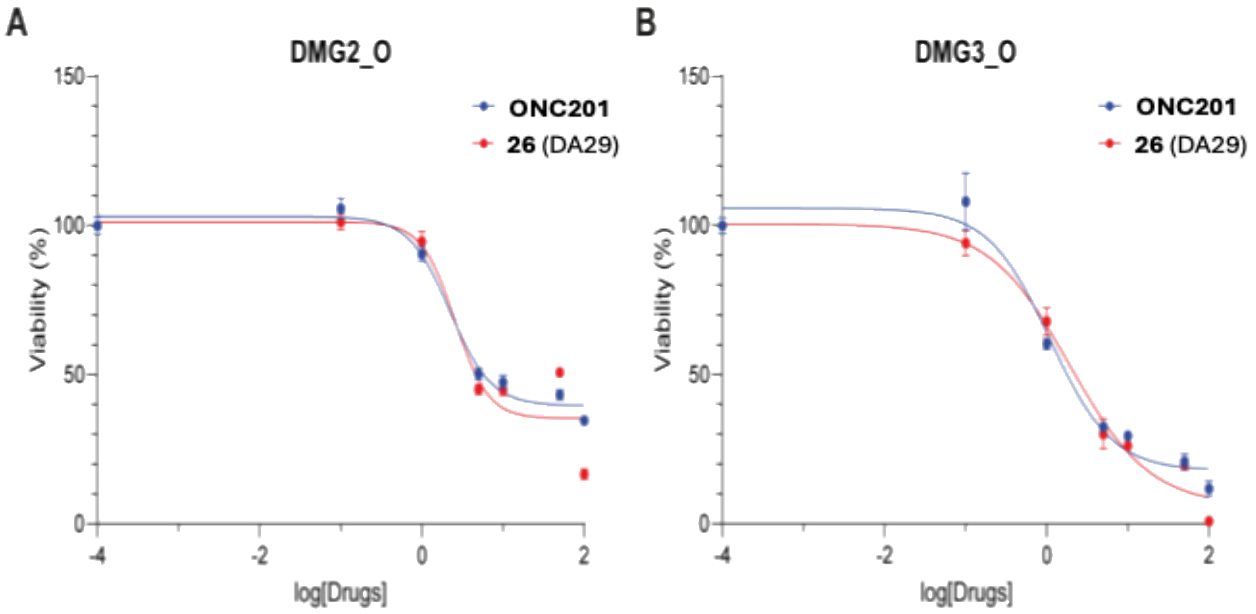

Sample name	Localisation	Primary/ Relapse tumor	Key genetic traits	Live/dead status
DMG2-O	brainstem	primary	H3: K27M; TP53: G404T	dead (<24months)
DMG3-O	brainstem / frontal, right	relapse	H3: K27M; PIK3CA: G1624A	dead (<24months)

Figure 40. Cytotoxic activity of 26 (DA29) and ONC201 in DIPG patient-derived tumor organoid models. Dose-response curves showing the viability of DMG2_O (**A**) and DMG3_O (**B**) after a 72 h of treatment with compound **26** (DA29) or **ONC201**. Cell viability was assessed using the CellTiter-Glo® 3D Cell Viability Assay and is expressed as percentage of untreated (vehicle) controls (n = 6).

2.3.6. Membrane permeability of ONC201, 26 (DA29), quercetin and caffeic acid

Compound **26** (DA29) was investigated for its membrane permeability, with emphasis on its potential to cross biological barriers. *In silico* analysis using the SWISS ADME platform (BOILED-Egg model, logP, and topological polar surface area)[163] suggested BBB penetration based on its physicochemical profile and pharmacokinetic properties. This prediction was experimentally validated using Caco-2 cells in static and dynamic assays, well-established *in vitro* models for intestinal absorption and, to some extent, BBB permeability due to their expression of multiple efflux and uptake transporters (Table 4).

Table 4. Apparent permeability ($\mathbf{P_{app}}$)[a] of **ONC201**, **26** (DA29), caffein and caffeic acid through CaCO-2 cell line monolayer. [a]Data are expressed as the meanof at least three independent experiments.

Compounds	P_{app} BA (nm/sec)	P_{app} AB (nm/sec)	BA/AB
ONC201	2157	356	6.05
26 (DA29)	2400	406	5.91
quercetin	486	237	0.48
caffeic acid	2005	380	5.28

The apparent permeability coefficients ($P_{app,}$ nm/s) of **ONC201**, **26** (DA29), quercetin, and caffeic acid in both basolateral-to-apical (BA) and apical-to-basolateral (AB) directions are summarized in Table 4. Quercetin displayed symmetric bidirectional permeability (Papp A→B = 486 nm/sec; Papp B→A = 237 nm/sec; BA/AB = 0.48), consistent with passive diffusion with minimal efflux and its known ability to cross the BBB, confirming its role as a positive control. In contrast, caffeic acid exhibited high apical-to-basolateral permeability (Papp A→B = 2005 nm/sec) but strong asymmetry (BA/AB = 5.28), indicative of active efflux and poor net BBB transport, thus serving as a negative control. **ONC201** and **26** (DA29) showed high BA permeability (2157 and 2400 nm/sec, respectively) and substantially lower AB values (356 and 406 nm/sec), resulting in ratios of 6.05 and 5.91. Notably, **26** (DA29) demonstrated a modestly higher BA permeability and slightly reduced efflux ratio compared to **ONC201**, suggesting an improved permeability profile that could translate into enhanced bioavailability and tissue penetration. **26** (DA29) does not interact with P-gp efflux pumps exhibiting an EC_{50} > 50 µM in the calcein-AM test assay (data not shown).

2.3.7. Evaluation of 26 (DA29) transport under physiological flow conditions

Dynamic permeability was assessed in the LB2 bioreactor under flow conditions, and apical concentrations were monitored over time by HPLC. Quantification was carried out at the λ_{max} of each compound by using calibration curves. The laminar flow applied (150 µL/min; shear stress ≈ 6×10^{-4} Pa) closely reproduced physiological intestinal dynamics[164]. **26** (DA29) displayed a

progressive, time-dependent decrease in apical levels, with ~60% depletion after 6 h, indicative of permeation across the Caco-2 monolayer (Figure 41). Quercetin and caffeic acid were included as reference standards due to their well-documented differences in permeability[165]. Consistent with expectations, quercetin rapidly disappeared from the apical chamber within 2-4 h, confirming high permeability, whereas caffeic acid remained largely unchanged, indicating poor translocation. These controls validated the assay and positioned **26** (DA29) as having intermediate permeability, between the low-permeable caffeic acid and highly permeable quercetin. This profile supports its potential for central nervous system (CNS) delivery, although additional studies are required to clarify the balance between passive diffusion and transporter-mediated mechanisms[166].

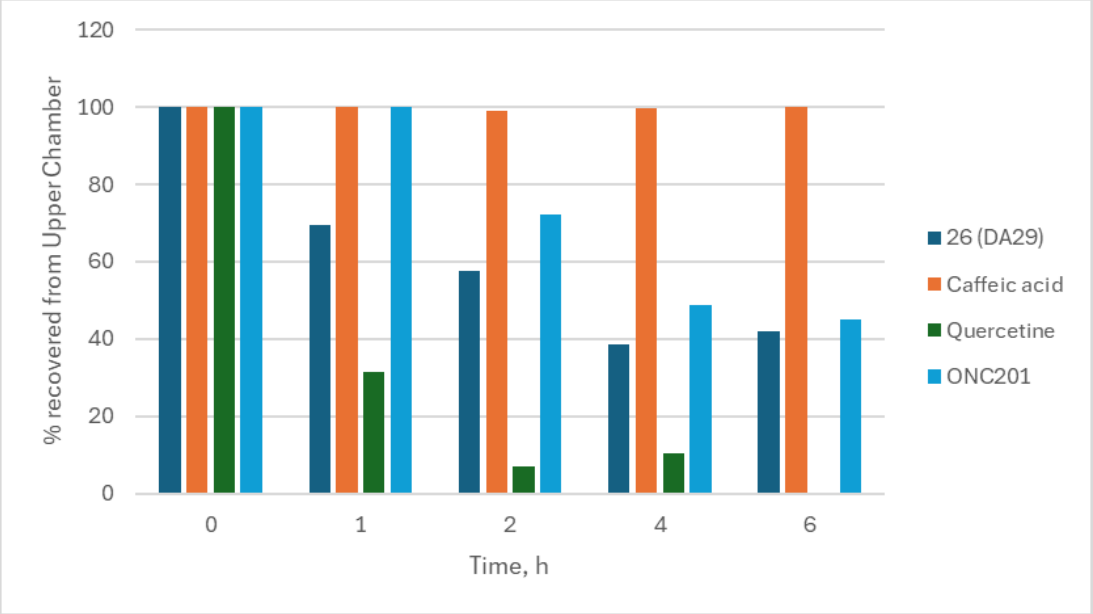

Figure 41. Time-dependent decrease in the percentage of compound recovered from the apical (upper) chamber under dynamic flow conditions in the FlowCell® LB2 bioreactor. The graph shows the percentage of **26** (DA29) (blue), caffeic acid (orange), and quercetin (green) remaining in the apical compartment at various time points, as determined by HPLC quantification at their respective λ_{max} using calibration curves.

2.3.8. Reactive Oxygen Species (ROS) production in SU-DIPG-36 cells lines treated with ONC201 or 26 (DA29)

To further investigate the anticancer mechanisms of the most promising compound in SU-DIPG-36 cells, **ONC201** and **26** (DA29) were evaluated for their ability to induce intracellular ROS. **ONC201** was tested at 20 µM, whereas **26** (DA29) was used at 1 µM, with incubation times of 1h, 6 h, and 24 h. The concentrations were selected based on the different EC_{50} cytotoxicity values observed for the two compounds. Intracellular ROS were detected using 1 µM dichloro-dihydro-fluorescein diacetate (DCFH-DA) for 1h. Menadione (25 µM, 50 min) served as a positive control for ROS induction[167], **ONC201** induced a fluorescence increase after 1 h, consistent with ROS production, which returned to basal x-median values (comparable to the control, 1 µM DCFH-DA at 1 h) after 6 h of treatment. **26** (DA29) triggered a marked fluorescence rise at 6 h, followed by a return to baseline at 24 h (Figure 42).

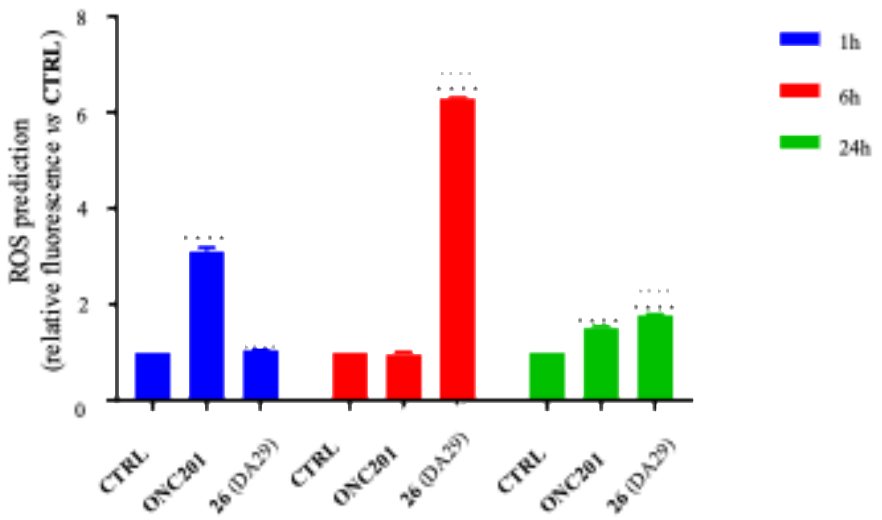

Figure 42. ROS production in SU-DIPG-36 cells in the presence of 20 mM **ONC201** or 1 mM **26** (DA29).

2.3.9. 26 (DA29) targeted *h*ClpP and hampered mitochondrial function in SU-DIPG-36 cells

Data reported above demonstrated that **26** (DA29) strongly activates purified recombinant *h*ClpP *in vitro*. On this basis, we evaluated whether **26** (DA29) could also bind the endogenous ClpXP complex in human cells. As previously shown by us and others[2, 170], ClpP chemical activators such as imipridones displace the chaperone subunit ClpX from the complex, leading to its degradation through a not fully defined mechanism. Therefore, ClpX suppression is considered an hallmark of ClpP engagement.

In cultured DIPG cells treated with **26** (DA29) for 24 h at concentrations comparable with the EC_{50} values, ClpX was completely abolished while ClpP remained unaffected (Figure 43A). In contrast, the negative control **33** (DA28) had no effect on either protein, confirming that **26** (DA29) specifically targets the ClpXP complex in cells.

The chemo-activation of ClpP promotes uncontrolled degradation of mitochondrial proteins, including respiratory chain subunits, TCA cycle enzymes, and the transcription factor TFAM, as also demonstrated by Mabanglo *et a*[170]. To test whether **26** (DA29) triggered this effect in DIPG cells, we examined representative subunits of the respiratory chain. After 24 h treatment, SDHB, UQCRC2, and ATP5A (Complex II, III, and V, respectively) were markedly reduced, whereas NDUFB8 (Complex I) was unaffected, suggesting that Complex I remained assembled. Moreover, the mitochondrial-encoded Cytochrome C Oxidase subunit I (COI, Complex IV) decreased (Figure 43A). These results indicate that ClpP hyperactivation by **26** (DA29) leads to the degradation of respiratory chain components, thereby impairing OXPHOS.

Consistently, **26** (DA29) also caused a dramatic reduction in mtDNA levels (Figure 43C). Since mtDNA maintenance depends mainly on TFAM, we measured its expression and found a strong decrease (Figure 43A, B). As TFAM is a substrate of activated ClpP, its loss is likely a direct consequence of ClpP hyperactivation. Longer exposures would probably result in complete TFAM

suppression but were lethal in SU-DIPG-36 cells. Notably, VDAC1, a marker of mitochondrial mass, remained unchanged, suggesting that mitochondrial biogenesis was not impaired after 24 h of treatment.

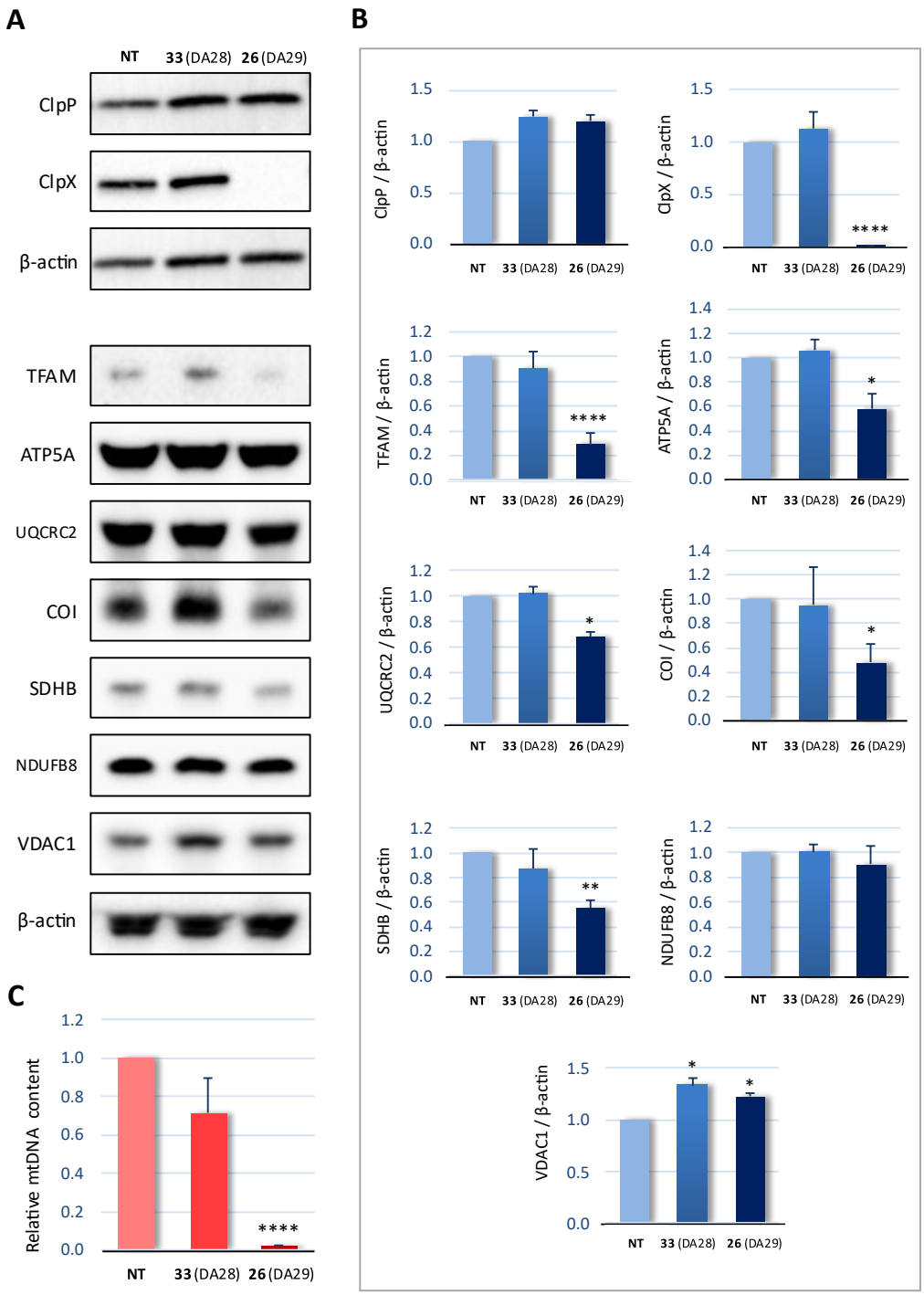

Figure 43. Mitochondrial effect of **26** (DA29) treatments on SU-DIPG-36 cells. **A)** Whole cell lysates were prepared after 24 hours of treatment with either negative control **33** (DA28) or **26**

(DA29) and separated by 12% SDS/PAGE. Immunodetection by specific antibodies revealed the steady-state level of examined proteins (depicted on the left); **B**) bars represent the relative quantification of proteins shown in panel B, normalized to β-actin. Results are presented as the mean ± SEM and are representative of at least three replicates. Statistical analysis was performed using the one-sample Student's t test (*, $p<0.05$; **, $p<0.01$; ****, $p<0.0001$); **C**) mitochondrial DNA relative levels were measured by qPCR. Bars represent the relative mtDNA content of the treated SU-DIPG-36 compared to untreated cells (NT, set as equal to 1), normalized to 18S rRNA gene (endogenous control). Ratios were calculated according to the Pfaffl's formula and presented as the mean ± SEM (n=4). Statistical analysis was carried out using the one-sample Student's t test (****, $p<0.0001$)

2.3.10. 26 (DA29) negatively affected polysome formation by activating ClpP in *cellulo*

Mitochondrial ribosomes are a central hub for protein quality control, integrating signals from various mitochondrial processes[171]. Disruption of this system can activate a stress response linking ribosome homeostasis and mitochondrial dysfunction[172]. Given the marked decrease in mtDNA and the degradation of OXPHOS subunits upon **26** (DA29) treatment, we investigated its effects on mitochondrial gene expression, focusing on mitoribosomes proteins (MRPs).

We first measured the steady-state levels of two MRPs, uL13m and mS29, representative proteins of the large (mtLSU, 39S) and small (mtSSU, 28S) ribosomal subunits. As expected, since mtDNA encodes both mt-rRNAs, **26** (DA29) treatment significantly reduced both MRPs (Figure 44A, B), indicating fewer ribosomes available for translation.

To assess the mitoribosome assembly in untreated and **33** (DA28) or **26** (DA29)-treated SU-DIPG-36 cells, total proteins were fractionated on an isokinetic sucrose gradient. Analysis of the

distribution along the gradient of mS29 and uL13m subunits showed that both mtSSU (fractions 4-5) and mtLSU (fractions 6-7) subunits were correctly assembled in all SU-DIPG-36 cells. However, in **26** (DA29)-treated cells both ribosomal subunits were concurrently undetectable in the highest density fractions (fractions 8-11). This finding, in line with the decrease of both subunits observed above, suggests that when SU-DIPG-36 cells were treated with **26** (DA29) but not with **33** (DA28), normal polysome formation does not occur, which is indicative of inefficient mitochondrial translation (Figure 44C).

The same analysis was used to evaluate ClpXP assembly. In untreated and **33** (DA28)-treated cells, ClpP and ClpX co-localized and were also present in high-density fractions (5-7), consistent with intact high-molecular-weight complexes. Upon **26** (DA29) treatment, ClpP was mostly found in the lighter fractions where ClpX was almost undetectable, indicating disassembly of the ClpXP complex and loss of the ClpX hexameric cap (Figure 44C). Overall, these findings confirm that **26** (DA29) binds ClpP in cellulo, displaces ClpX, and promotes its degradation.

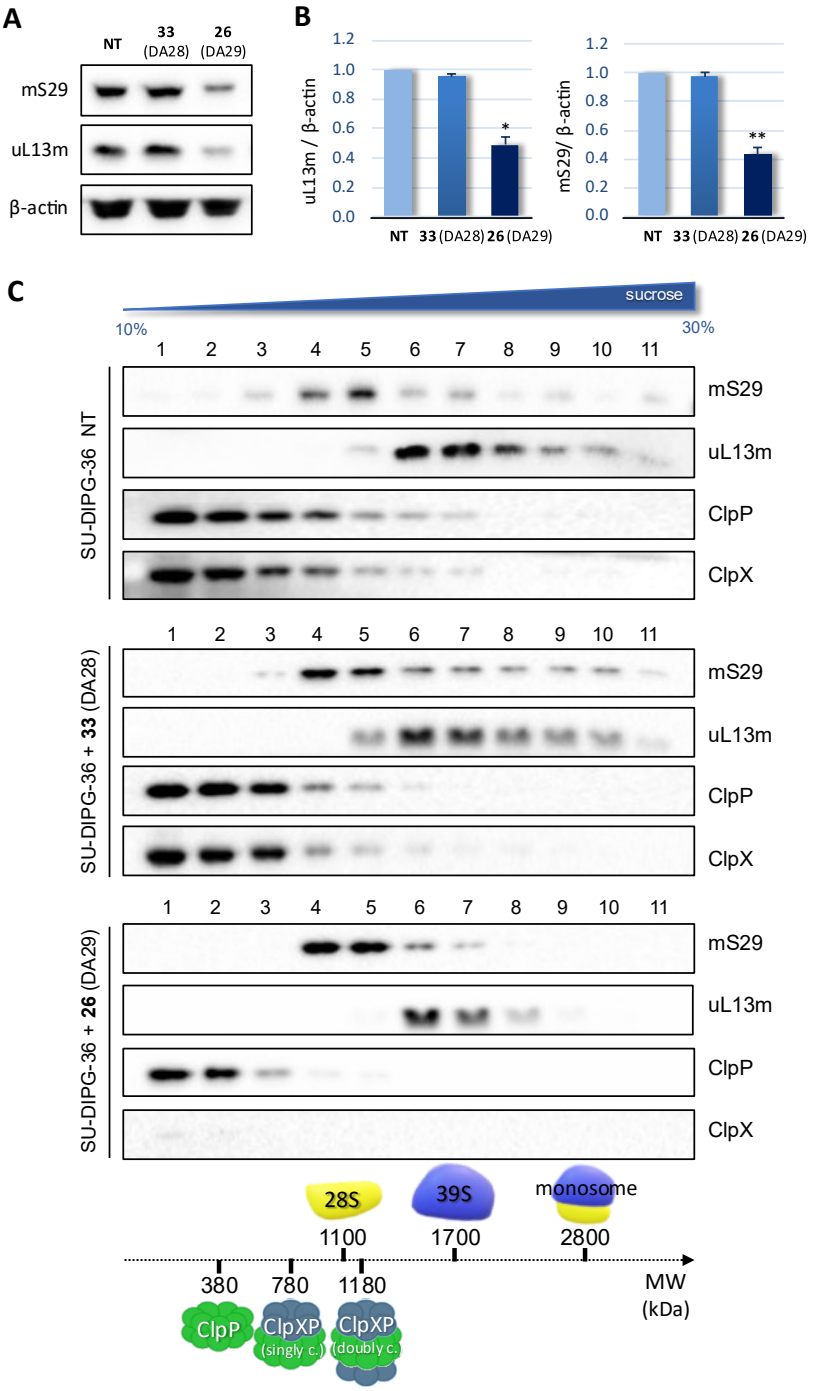

Figure 44. Molecular analysis of mitoribosomal subunits and ClpXP complex. **A)** Mitoribosomal subunit steady-state levels were determined by immunoblotting, as described in Figure 6D1 legend; **B**) Bars represent the relative quantification of proteins shown in panel A, normalized to β-actin. Results are presented as the mean ± SEM and are representative of three replicates. Statistical significance was evaluated by one-sample Student's t test (*, $p<0.05$; **, $p<0.01$); **C**) Isokinetic sucrose gradient analysis of mitoribosomal subunits and ClpXP complex in either SU-DIPG-36 cells

untreated (NT) or treated with **33** (DA28) (negative control) and **26** (DA29) (ClpP activator). At the bottom, the ClpP and ClpXP complexes (singly and doubly capped), as well as mtSSU (28S), mtLSU (39S) and monosome, are depicted in order of increasing estimate molecular weight (MW) corresponding to the gradient fractions.

2.3.11. Lipid profile in SH-SY5Y and SU-DIPG-36 cell lines treated with ONC201 and 26 (DA29)

Activation of *h*ClpP in cancer cells disrupts several metabolic pathways, including lipid metabolism[173]. To explore this effect, lipidomic profiling of SU-DIPG-36 and SH-SY5Y cells (neuroblastoma cell line from a metastatic bone tumor), untreated or treated with **ONC201** and **26** (DA29) was performed by GC-MS/FID (fatty acids) and HPLC-MS/MS (intact lipids). Lipid composition is one of key indicators of cell health, and treatments with drugs can markedly alter lipid metabolism.

GC-MS analyses identified 34 fatty acids across different chemical classes according to number and position of double bonds along the carbon chain. In untreated cells, saturated fatty acids (SFAs) were most abundant, ranging from 49.99 ± 0.07 % in SH-SY5Y to 68.65 ± 0.16 % in SU-DIPG-36. The main SFAs were myristic (C14:0, ~1.3-1.4 %), palmitic (C16:0, 28.69 ± 0.04 % and 41.15 ± 0.20 % in SH-SY5Y and SU-DIPG-36, respectively), and stearic acid (C18:0, 18.01 ± 0.03 % and 41.15 ± 0.20 %, respectively). Monounsaturated fatty acids (MUFAs) were the second most represented class (40.92 ± 0.16 % in SH-SY5Y; 23.33 ± 0.17 % in SU-DIPG-36), mainly palmitoleic (C16:1ω7, 0.71-3.36 %), oleic (C18:1ω9, 12.77-28.85 %), and vaccenic acid (C18:1ω7, 3.25-5.00 %). Polyunsaturated fatty acids (PUFAs) were least abundant (9.10 ± 0.23 % in SH-SY5Y; 8.01 ± 0.04 % in SU-DIPG-36), with linoleic (C18:2ω6, 0.26-2.46 %), arachidonic (C20:4ω6, 0.37-2.84 %), and docosahexaenoic acid (C22:6ω3, trace-1.41 %) as main representatives (Appendix Table S2).

As previously reported[2], drug treatments alter fatty acid composition, particularly MUFAs and PUFAs due to their higher susceptibility to oxidation processes than SFAs, in accordance with the availability of allylic hydrogen. **ONC201** (24 h treatment) markedly reduced MUFA and PUFA levels in SH-SY5Y, suggesting an effect on membrane composition (Figure 45). By contrast, **26** (DA29) did not significantly affect SU-DIPG-36 cells under the same conditions[2]. Indeed, fatty acid distributions in SU-DIPG-36 remained comparable between untreated and treated samples (Appendix Table S2), consistent with earlier findings in this cell line[2]. Therefore, further analyses were extended to intact lipids determined using HPLC-MS/MS.

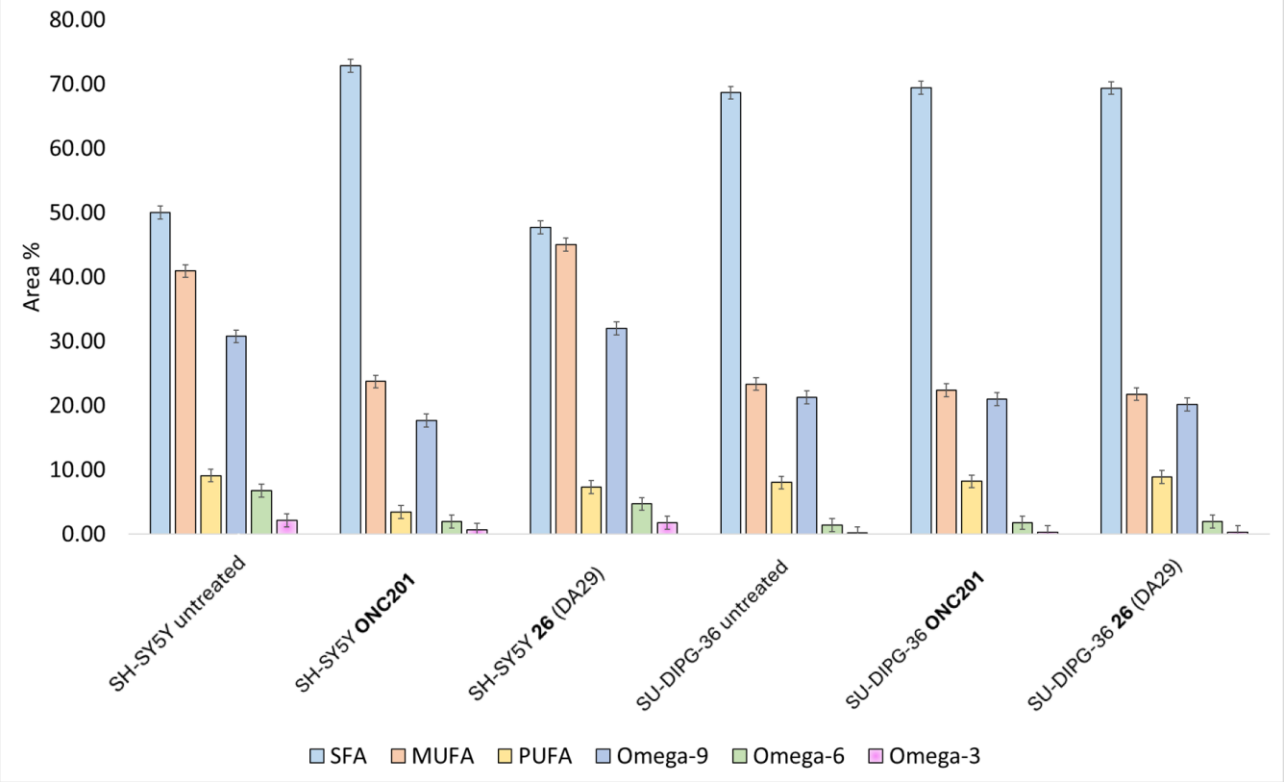

Figure 45. Effect of **ONC201** and **26** (DA29) on the lipid content of SFA, MUFA, PUFA, omega-9, omega-6, and omega-3 classes, in SH-SY5Y and SU-DIPG-36 cell lines. For each identified species, the error bars indicate the standard deviation.

The untargeted HPLC-MS/MS analysis identified 45 lipid species in SH-SY5Y and 51 in SU-DIPG-36 cells (Appendix Tables S3, S4). Lipids were separated according to polarity and eluted by

increasing partition number (PN) calculated using the equation PN = CN-2DB, where CN and DB are the carbon and double bond numbers, respectively. The chromatogram was divided into three regions: very polar lipids (LPLs), medium-polar lipids (PLs and SMs), and non-polar lipids (TGs), eluted in the PN range 42-52.

The complete list of molecules, with retention time (t_R), detected ions, class, PN, CN, and DB values, is given in Appendix Tables S3, S4. TGs were mainly detected as ammonium and sodium adducts, while PLs appeared as protonated ions. Relative quantification was performed for choline-containing lipids (LPCs, PCs and SMs) and TGs, assuming comparable MS response and recovery during extraction within each lipid class (Appendix Tables S3, S4). Differences in the relative abundance of choline-containing lipids and TGs were evaluated by two-tailed t test ($p < 0.05$) and are reported in Appendix Tables S5 and S6, and in Appendix Figure S2 and S3, respectively.

Treatment of SU-DIPG-36 cells with **ONC201** or **26** (DA29) showed similar effects on choline-containing lipids (LPCs) and TGs after 24 h. Almost all LPCs decreased significantly, except LPC 14:0 and 16:1, and most SMs were reduced, except SM 31:0 and SM 34:1. A comparable decrease of all LPCs was observed in SH-SY5Y cells for both drugs (Appendix Table S5). This effect may reflect impaired mitochondrial function, since low LPC levels reduce glycerol phosphate dehydrogenase (GPDH) activity[174], or could represent a defense mechanism against ROS induced by *h*ClpP activation[175].

For TGs, a significant decrease was observed in species with PN 50 and 52 (TG 52:1, TG 54:2, TG 56:3, TG 54:1) and TG 54:3 (PN 48), while TGs with lower PN (42-48) increased, except TG 52:5, in SU-DIPG-36 cells treated with both compounds. This pattern correlates with previous findings of increased C16 fatty acids (e.g., palmitic acid, C16:0) and decreased long-chain fatty acids in SU-DIPG-36 cells treated with similar drugs[2]. A similar, though less pronounced, trend was also seen in SH-SY5Y cells (Appendix Table S6). This behavior could be caused by the inhibition of the very-

long-chain fatty acids elongase (ELOVLs) enzymes, responsible for the elongation of shorter chain fatty acids, following the disruption of the mitochondrial function caused by the treatment[176].

Chapter 3. Conclusion

Through a stepwise rational design strategy, we optimized the piperazine scaffold to enhance interactions within the *h*ClpP hydrophobic allosteric pocket. While piperazine bearing an exocyclic carboxyl markedly reduced activity, incorporation of an endocyclic carboxyl in the 2-oxopiperazine scaffold restored the critical interaction with Q107 and, when combined with electron-withdrawing substituents on both benzyl arms, compound **26** (DA29) was identified as the most potent *h*ClpP activator known to date (EC_{50} = 0.85 ± 0.14 μM; 95% activation), with negligible activity on dopamine D2-like receptors.

High-resolution X-ray crystallography revealed that **26** (DA29) binds in the *h*ClpP H pocket with a characteristic pincer topology, forming a network of hydrogen bonds with Q107, Y118, and S108 and engaging in π-π and anion-π interactions with aromatic residues. These features induce axial pore expansion and displacement of the ClpX co-chaperone, hallmarks of *h*ClpP hyperactivation.

The initial hypotheses for the rational design of piperazines, supported by biological results, were then compared by identifying the actual interactions of **26** (DA29) through its crystallographic structure. The aminic nitrogen atom of **26** (DA29) establishes H-bonding with the hydroxyl of tyrosine (Y118) as in THPPDs. The side chain of glutamine (Q107) participates in an extensive network of hydrogen bonds, forming, with the amide carboxyl function of **26** (DA29), a water-mediated bridge in which the amide backbone of leucine (L104) also participates, confirming once again the structural overlap with THPPDs. The interaction of the second carboxyl function of THPPDs with glutamic acid (E82), which further stabilizes the bond, is also observed in **26** (DA29). In this case, however, an anion-π interaction is observed with the phenyl ring substituted with the *p*-CF_3, an interaction made possible by the trifluoromethyl, thanks to its strong electron-withdrawing effect that deactivates the phenyl. This underlines the importance of substituents EWGs in the piperazines, confirming the structural overlap between the different derivatives (Figure 18).

Consistently, CETSA confirmed intracellular target engagement, while biochemical analyses demonstrated ClpX degradation, loss of OXPHOS subunits and TFAM, mtDNA depletion, and impaired mitoribosome assembly, culminating in defective mitochondrial translation.

Functionally, **26** (DA29) exhibited potent cytotoxicity, with greater efficacy in SU-DIPG-36 than SU-DIPG-50 cell lines, and retained activity in patient-derived organoids, achieving effects comparable to **ONC201**. Importantly, permeability assays in static and dynamic Caco-2 systems demonstrated favorable basolateral transport and reduced efflux compared to **ONC201**, supporting its potential for CNS delivery. Finally, lipidomic profiling revealed consistent remodeling of LPCs and TGs, corroborating mitochondrial dysfunction and suggesting metabolic signatures as biomarkers of *h*ClpP hyperactivation.

Together, these findings establish **26** (DA29) as a new generation of *h*ClpP activator with optimized potency, selectivity, and pharmacokinetic properties. By dismantling mitochondrial proteostasis and bioenergetics, **26** (DA29) exerts robust anticancer activity in translational DIPG models, thereby providing a promising lead compound for therapeutic development in paediatric brain tumors and other *h*ClpP-dependent malignancies.

Chapter 4. Experimental Section

Chemistry. ^{1}H NMR and ^{13}C NMR spectra were recorded on a Bruker 600 MHz or AGILENT 500 MHz spectrometer and chemical shifts are reported in parts per million (δ), and the following abbreviations were used to explain the multiplicities: s = singlet, d = doublet, dt = doublet of triplet, t = triplet, td = triplet of doublet, q = quartet, m = multiplet, quin = quintuplet, sext = sextet, sep = septet, b = broad. FT-IR spectra were recorded on a Perkin-Elmer 681 spectrophotometer. GC analyses were performed on a HP 6890 model, Series II by using a HP1 column (methyl siloxane; 30 m x 0.32 mm x 0.25 μm film thickness). Analytical thin-layer chromatography (TLC) was carried out on pre-coated 0.25 mm thick plates of Kieselgel 60 F254; visualization was accomplished by UV light (254 nm). Column chromatography was accomplished by using silica gel 60 with a particle size distribution 40-63 μm and 230-400 ASTM. GC-MS analyses were performed on HP 5995C model. High-resolution mass spectrometry (HRMS) analyses were performed using a Bruker microTOF QII mass spectrometer equipped with an electrospray ion source (ESI). Reagents and solvents were purchased from Sigma-Aldrich (Sigma-Aldrich, St. Louis, MO, USA) and used without any further purification. Full characterization data have been reported for both the newly synthesized compounds and the known compounds. All spectral data are consistent with the reported values.

General synthesis of 1-2.

To a stirred suspension of piperazine (5.80 mmol) and K_2CO_3 (14.5 mmol) in CH_3CN (14 mL) was added the appropriate benzyl bromide (12.76 mmol). The reaction mixture was stirred at room temperature for 2 h. The reaction progress was monitored by TLC (CH_2Cl_2/MeOH = 9.8/0.2 as mobile phase). Then, the resulting solid was filtered and repeatedly washed with EtOAc. The organic filtrate was concentrated under reduced pression, and the resulting brown semisolid

underwent to chromatography on silica gel and CH_2Cl_2/MeOH = 9.8/0.2 as mobile phase for **1** and CH_2Cl_2/MeOH = 9.5/0.5 as the mobile phase for **2**.

1,4-Bis(4-chlorobenzyl)piperazine 1 (DA1). White solid, 25% yield. M.p. 136-138 °C. ^{1}H NMR (500 MHz, $CDCl_3$, δ): 7.29-7.22 (m, 8H, aromatic protons), 3.47 (s, 4H, 2Ph*CH*$_2$N), 2.46 (s, 8H, N*(CH*$_2$*)*$_2$N*(CH*$_2$*)*$_2$). ^{13}C NMR (125 MHz, $CDCl_3$, δ): 136.28, 132.48, 130.16, 128.07, 61.90, 52.65. GC−MS (70 eV) (*m/z*) (rel. int.) 335 (M^+, 2), 334 (8), 209 (33), 180 (5), 166 (6), 154 (21), 125 (100), 89 (14), 42 (6). HPLC: Rt = 14.023 min (mobile phase: CH_3CN/CH_3COONH_4 = 70/30; stationary phase: ZORBAX ECLIPSE Plus C18, analytical 4.6x250mm, 5 μm); rate = 1mL/min.

1,4-Bis(4-cyanobenzyl)piperazine 2 (DA4). White solid, 39% yield. M.p. 127-130 °C. ^{1}H NMR (500 MHz, $CDCl_3$, δ): 7.65 (s, 2H, aromatic protons), 7.56-7.53 (m, 4H, aromatic protons), 7.41 (t, 2H, *J* = 7.7 Hz, aromatic protons), 3.54 (s, 4H, 2NC*H*$_2$Ph), 2.49 (s, 8H, N*(CH*$_2$*)*$_2$N*(CH*$_2$*)*$_2$). ^{13}C NMR (125 MHz, $CDCl_3$, δ): 139.81, 133.36, 132.41, 130.85, 129.05, 118.89, 112.39, 61.89, 52.89. GC−MS (70 eV) (*m/z*) (rel. int.) 316 (M^+,10), 200 (34), 171 (13), 157 (16), 145 (52), 116 (100), 89 (21), 56 (9), 42 (12). HPLC: Rt = 5.058 min (mobile phase: CH_3CN/CH_3COONH_4 = 70/30; stationary phase: ZORBAX ECLIPSE Plus C18, analytical 4.6x250mm, 5 μm); rate = 1mL/min.

3-(Piperazin-1-ylmethyl)benzonitrile 3 (DA2). To a stirred suspension of piperazine (0.351 g; 4.08 mmol) and K_2CO_3 (0.169 g; 1.22 mmol) in CH_3CN (10 mL) was added the 3-(Bromomethyl)benzonitrile (0.200g; 1.02 mmol). The reaction mixture was stirred at room temperature for 2 h. The reaction progress was monitored by TLC (CH_2Cl_2/MeOH = 9.5/0.5 as mobile phase). Then, the resulting solid were filtered and repeatedly washed with EtOAc. The organic filtrate was concentrated under reduced pression, and the product was isolated by purification with chromatography on silica gel and CH_2Cl_2/MeOH = 9/1 as the mobile phase. White semisolid, 81% yield. ^{1}H NMR (500 MHz, DMSO, δ): 7.70-7.67 (m, 2H, aromatic protons), 7.63-7.59 (m, 1H, aromatic proton), 7.53-7.48 (m, 1H, aromatic proton), 3.45 (s, 2H, NCPhC*H*$_2$N), 2.66

(t, 4H, *J* = 4.8 Hz, 2NHC*H*$_2$), 2.32-2.18 (m, 4H, 2NC*H*$_2$). GC−MS (70 eV) (*m/z*) (rel. int.) 201 (M^+, 17), 159 (100), 116 (79), 89 (16), 56 (22), 42 (1).

1-(3-Cyanobenzyl)-4-(3-(trifluoromethyl)benzyl)piperazine 4 (DA7). To a stirred suspension of **3** (0.196 g; 0.98 mmol) and K_2CO_3 (0.175g; 1.27 mmol) in CH_3CN (5 mL) was added 3-(Trifluoromethyl)benzyl bromide (0.16 ml; 1.073 mmol). The reaction progress was monitored by TLC (EtOAc/hexane = 3/7 as mobile phase). Then, the resulting solid was filtered and repeatedly washed with EtOAc. The organic filtrate was concentrated under reduced pression, and the crude residue was purified through column chromatography (silica gel, EtOAc/hexane = 3/7 as mobile phase). Orange oil; 59% yield. ^{1}H NMR (500 MHz, $CDCl_3$, δ): 7.65 (s, 1H, aromatic proton), 7.59 (s, 1H, aromatic proton), 7.57-7.50 (m, 4H, aromatic protons), 7.42 (dd, 2H, J_1 = 9.15 Hz, J_2 = 7.75 Hz, aromatic protons), 3.58 (s, 2H, NC*H*$_2$PhCF$_3$), 3.54 (s, 2H, NC*H*$_2$PhCN), 2.51 (s, 8H, N*(CH$_2$)$_2$*N*(CH$_2$)$_2$*). ^{13}C NMR (125 MHz, $CDCl_3$, δ): 133.40, 132.46, 132.44, 130.87, 130.63 (q, *J* = 32 Hz), 129.06, 128.73, 125.72 (q, *J* = 3.2 Hz), 124.65 (q, *J* = 270.7 Hz), 124.09 (q, *J* = 3.5 Hz), 118.87, 112.40, 62.19, 61.85, 52.79. GC−MS (70 eV) (*m/z*) (rel. int.) 359 (M^+, 25), 243 (29), 200 (51), 188 (49), 159 (100), 145 (33), 116 (77), 89 (17),56 (11), 42 (16). HPLC Rt = 5.058 min (mobile phase: CH_3CN/CH_3COONH_4 70/30; stationary phase: ZORBAX ECLIPSE Plus C18, analytical 4.6x250mm, 5 μm); rate = 1mL/min.

General synthesis of 5-8. To a solution of piperazine (4.98 mmol) in absolute EtOH (3 mL), was added the appropriate benzoyl chloride (2.49 mmol), at 0 °C. The reaction mixture was stirred at room temperature, overnight. The reaction progress was monitored by TLC (CH_2Cl_2/MeOH = 9/1 as mobile phase). The solvent was evaporated under reduced pressure and to the residue was added CH_2Cl_2. The organic layer was washed with brine and was dried on anhydrous Na_2SO_4. The crude residue was purified by column chromatography (silica gel and CH_2Cl_2/MeOH = 9/1 as the mobile phase).

1-Benzoyl piperazine 5 (DA13). White solid, 19% yield. M.p. 62-65 ºC. ^{1}H NMR (300 MHz, $CDCl_3$, δ): 7.44-7.32 (m, 5H, aromatic protons), 4.69-4.27 (m, 8H, CON(CH_2)$_2$, NH(CH_2)$_2$). GC−MS (70 eV) (*m/z*) (rel. int.) 190 (M^+, 9), 160 (8), 134 (22), 122 (15), 105 (100), 85 (51), 77 (63), 69 (96), 56 (71), 51 (21), 42 (11).

3-(Piperazine-1-carbonyl)benzonitrile 6 (DA16). White solid, 3% yield. M.p. 164-167 °C. ^{1}H NMR (300 MHz, $CDCl_3$, δ): 7.73-7.66 (m, 2H, aromatic protons), 7.63 (dt, 1H, J_1 = 7.8 Hz, J_2 = 1.41 Hz, aromatic proton), 7.57-7.49 (m, 1H, aromatic proton), 3.74 (bs, 2H, CONCH_2), 3.36 (bs, 2H, CONCH_2), 3.01-2.71 (m, 4H, CH_2NHCH_2), 1.99 (s, 1H, N*H*). GC−MS (70 eV) (*m/z*) (rel. int.) 215 (M^+, 9), 185 (14), 130 (83), 102 (46), 85 (36), 75 (13), 69 (71), 56 (100), 42 (15).

1,4-Dibenzoylpiperazine 7 (DA12). White solid, 4% yield. M.p. 190-193 °C. ^{1}H NMR (300 MHz, $CDCl_3$, δ): 7.49-7.36 (m, 10H, aromatic protons), 3.63 (bs, 8H, N*(CH_2)$_2$*N*(CH_2)$_2$*). ^{13}C NMR (125 MHz, $CDCl_3$, δ): 170.64, 135.11, 130.08, 128.63, 127.04, 47.61, 42.35. GC−MS (70 eV) (*m/z*) (rel. int.) 294 (M^+, 3), 226 (9), 105 (100), 77 (39), 69 (11), 51 (8). HPLC Rt = 3.010 min (mobile phase: CH_3CN/ H_2O 70/30; stationary phase: ZORBAX ECLIPSE Plus C18, analytical 4.6x250mm, 5 μm); rate = 1mL/min.

3,3'-(Piperazine-1,4-dicarbonyl)dibenzonitrile 8 (DA15). White solid, 22% yield. M.p. 212-215 °C. ^{1}H NMR (500 MHz, DMSO, δ): 8.01-7.86 (m, 4H, aromatic protons), 7.81-7.72 (m, 2H, aromatic protons), 7.70-7.59 (m, 2H, aromatic protons), 3.82-3.56 (m, 4H, 2CONCH_2), 3.49-3.26 (m, 4H, 2CONCH_2CH_2). ^{13}C NMR (125 MHz, DMSO, δ): 167.69, 137.28, 137.26, 133.79, 132.21, 132.19, 131.05, 130.32, 118.70, 112.11, 47.42, 47.08, 42.19, 42.76. GC−MS (70 eV) (*m/z*) (rel. int.) 344 (M^+, 0.7), 130 (100), 102 (46), 69 (12), 56 (17), 42 (3).

1-(3-Cyanobenzoyl)-4-(4-chlorobenzoyl)piperazine 9 (DA17). To a solution of **6** (0.175 g; 0.81 mmol) in absolute EtOH (3 mL) was added 4-chlorobenzoyl chloride (0.214 g, 1.22 mmol), at 0 °C. The reaction mixture was stirred at room temperature, overnight. The reaction progress was monitored by TLC (EtOAc/hexane = 8/2 as mobile phase). The solvent was evaporated under

reduced pressure and to the residue was added CH_2Cl_2. The organic layer was washed with brine and was dried on anhydrous Na_2SO_4. The solvent was evaporated under reduced pressure. The product was isolated by column chromatography (silica gel and EtOAc/hexane = 8/2 as the mobile phase). White solid, 43% yield. M.p. 169-172 °C. ^{1}H NMR (300 MHz, $CDCl_3$, δ): 7.74 (dt, 1H, J_1 = 7.5 Hz, J_2 = 1.4 Hz, aromatic proton), 7.72-7.69 (m, 1H, aromatic proton), 7.65 (dt, 1H, J_1 = 7.8 Hz, J_2 = 1.4 Hz, aromatic proton), 7.57 (t, 1H, J = 7.68 Hz, aromatic proton), 7.45-7.33 (m, 4H, aromatic protons), 3.64 (bs, 8H, CON(CH_2CH_2)$_2$NCO). ^{13}C NMR (125 MHz, $CDCl_3$, δ): 169.59, 168.17, 136.43, 136.33, 133.57, 133.15, 131.31, 130.75, 129.70, 128.99, 128.64, 117.73, 113.19, 47.53, 42.53. GC−MS (70 eV) (*m/z*) (rel. int.) 355 (2), 354 (3), 353 (M^+, 5), 214 (11), 141 (34), 140 (8), 139 (100), 130 (75), 11 (32), 102 (31), 69 (35), 56 (18), 42 (6). HPLC Rt = 3.236 min (mobile phase: CH_3CN/CH_3COONH_4 70/30; stationary phase: ZORBAX ECLIPSE Plus C18, analytical 4.6x250mm, 5 μm); rate = 1mL/min.

General synthesis of 10-16.

A suspension of 2-oxopiperazine (0.99 mmol) and NaH (1.49 mmol) in anhydrous DMF (3 mL) was stirred at 0 °C for 30 minutes. After this time, the appropriate substituted-benzyl bromide (1.19 mmol) was added to the reaction mixture, and the reaction was heated to 90 °C for 16 h. The reaction mixture was cooled to room temperature, and it was concentrated under reduced pressure. EtOAc was added to residue and the solution was washed with brine. The organic layer was dried on anhydrous Na_2SO_4, and the solvent was evaporated under reduced pressure. The resulting crude mixture underwent column chromatography on silica gel to give 10−16.

3,3'-((2-Oxopiperazine-1,4-diyl)bis(methylene))dibenzonitrile 10 (DA9). Orange oil; 38% yield. ^{1}H NMR (500 MHz, CD_3OD, δ): 7.71 (s, 1H, aromatic proton), 7.68-7.57 (m, 5H, aromatic protons), 7.51 (dt, 2H, J_1 = 7.7 Hz, J_2 = 2.7 Hz, aromatic protons), 4.63 (s, 2H, NCPhCH_2NCO), 3.65 (s, 2H, NCPhCH_2NCH_2), 3.33 (t, 2H, J = 5.35 Hz, CONCH_2CH_2N), 3.23 (s, 2H, NCOCH_2N), 2.72 (t, 2H, J = 5.55 Hz, NCH_2CH_2NCO). ^{13}C NMR (125 MHz, CD_3OD, δ): 167.97, 138.89, 138.38, 133.53,

132.38, 132.28, 131.19, 131.05, 131.02, 129.51, 129.28, 59.93, 56.37, 48.65, 48.55, 46.24. HRMS (ESI) *m/z*: calc. for $[C_{18}H_{18}Br_2N_2O + H]^+$: 436.9840; ESI-MS-MS: 436.9840, 410.9855, 212.0059, 168.9639, 90.0462. ESI-MS *m/z*: $[C_{20}H_{18}N_4O + Na]^+$: 353.1374; ESI-MS-MS: 353.1378, 170.9956, 139.0394, 121.0367, 76.9972. ESI-MS *m/z*: $[C_{20}H_{18}N_4O-H]^-$, 329.1424. ESI-MS-MS: 329.1417, 143.0622, 116.0510, 70.0302. The compound was purified through column chromatography (silica gel, CH_2Cl_2/MeOH = 9.0/0.2 as the mobile phase).

1,4-Bis(3-(Trifluoromethyl)benzyl)piperazin-2-one 11 (DA24). Orange oil; 37% yield. ^{1}H NMR (300 MHz, $CDCl_3$, δ): 7.63-7.40 (m, 8H, aromatic protons), 4.65 (s, 2H, $CF_3PhC\mathit{H_2}NCO$), 3.62 (s, 2H, $CF_3PhC\mathit{H_2}NCH_2$), 3.31-3.19 (m, 4H, $NCOC\mathit{H_2}N$, $CONC\mathit{H_2}CH_2N$), 2.68 (t, 2H, *J* = 5.2 Hz, $NC\mathit{H_2}CH_2NCO$). ^{13}C NMR (125 MHz, CD_3OD, δ): 167.24, 157.91, 137.78, 137.26, 132.75, 131.57, 131.56, 131.42, 131.41, 130.81, 130.73, 130.63, 130.56, 130.48, 130.38, 130.30, 129.36, 129.33, 129.21, 129.05, 128.95, 125.55 (q, *J* = 3.85 Hz), 125.24, 125.19, 124.64, 124.62, 124.55, 124,54, 124.38, 124.37, 124.36, 124.33, 124.29, 124.27, 124.07 (q, *J* = 3.85 Hz), 123.09, 123.04, 60.13, 55.86, 48.71, 48.61, 45.66. GC−MS (70 eV) (*m/z*) (rel. int.) 417 (3), 416 (M^+, 12), 388 (5), 387 (22), 258 (9), 257 (64), 160 (9), 159 (100), 141 (6), 140 (3), 139 (2), 109 (15), 42 (20). HPLC Rt = 7.937 min (mobile phase: CH_3CN/CH_3COONH_4 70/30; stationary phase: ZORBAX ECLIPSE Plus C18, analytical 4.6x250mm, 5 μm); rate = 1mL/min. The product was isolated by column chromatography (silica gel and EtOAc/hexane = 7/3 as the mobile phase)

1,4-Bis(2-fluorobenzyl)piperazin-2-one 12 (DA32). Orange semisolid; 22% yield. ^{1}H NMR (500 MHz, CD_3OD, δ): 7.55-7.39 (m, 1H, aromatic protons), 7.37-7.22 (m, 3H, aromatic protons), 7.16 (t, 1H, *J* = 7.5 Hz, aromatic proton), 7.11 (td, 1H, J_1 = 7.5 Hz, J_2 = 0.9 Hz aromatic proton), 7.09-7.00 (m, 2H, aromatic protons), 4.65 (s, 2H, $FPhC\mathit{H_2}NCO$), 3.81 (s, 2H, $FPhC\mathit{H_2}NCH_2$), 3.53-3.26 (m, 4H, $NCOC\mathit{H_2}N$, $CONC\mathit{H_2}CH_2N$), 2.97-2.72 (m, 2H, $CONCH_2C\mathit{H_2}N$). ^{13}C NMR (125 MHz, $CDCl_3$, δ): 161.36 (d, *J* = 245.8 Hz), 161.11 (d, *J* = 2 44.8 Hz), 130.73 (d, *J* = 3.9 Hz), 129.46 (d, *J* = 8.3 Hz), 124.53 (d, *J* = 3.5 Hz), 115.59 (d, *J* = 21.9 Hz), 115.32 (d, *J* = 21.7 Hz), 53.66, 53.63,

48.80, 43.04, 43.01. GC−MS (70 eV) (*m/z*) (rel. int.) 317(2), 316 (M^+, 12), 288 (4), 287 (18), 208 (6),207 (49), 110 (8), 109 (100), 107 (2), 83 (11), 42 (11). HPLC Rt = 4.515 min (mobile phase: CH_3CN/CH_3COONH_4 70/30; stationary phase: ZORBAX ECLIPSE Plus C18, analytical 4.6x250mm, 5 μm); rate = 1mL/min. The product was isolated by column chromatography (silica gel and EtOAc/hexane = 1/1 as the mobile phase)

1,4-Bis(4-fluorobenzyl)piperazin-2-one 13 (DA36). White solid, 40% yield. M.p. 133-137 °C. ^{1}H NMR (500 MHz, $CDCl_3$, δ): 7.29-7.19 (m, 4H, aromatic protons), 7.04-6.97 (m, 4H, aromatic protons), 4.55 (s, 2H, PhCH_2NCO), 3.51 (s, 2H, PhCH_2NCH_2), 3.24-3.17 (m, 4H, NCOCH_2N, CONCH_2CH_2N), 2.62 (t, 2H, J = 5.45 Hz, CONCH_2CH_2N). ^{13}C NMR (125 MHz, $CDCl_3$, δ): 166.85, 161.24 (d, J = 244.5 Hz), 132.32 (d, J = 3.2 Hz), 130.57 (d, J = 7.9 Hz), 129.89 (d, J = 8.1 Hz), 115.51 (d, J = 21.5 Hz), 115.29 (d, J = 21.2 Hz), 60.97, 57.24, 49.15, 48.78, 45.87. GC−MS (70 eV) (*m/z*) (rel. int.) 316 (M^+, 12), 287 (11), 207 (30), 109 (100), 83 (9), 42 (7). HPLC Rt = 4.660 min (mobile phase: CH_3CN/H_2O 70/30; stationary phase: ZORBAX ECLIPSE Plus C18, analytical 4.6x250mm, 5 μm); rate = 1mL/min. The product was isolated by column chromatography (silica gel and EtOAc/hexane = 1/1 as the mobile phase)

1,4-Bis(2-bromobenzyl)piperazin-2-one hydrochloride 14 (DA33). White solid, 6% yield. M.p. 221-225 °C. ^{1}H NMR (500 MHz, CD_3OD, δ): 7.77 (dd, 1H, J_1 = 8.05 Hz, J_2 = 1.15 Hz, aromatic proton), 7.74 (dd, 1H, J_1 = 7.65 Hz, J_2 = 1.65 Hz, aromatic proton), 7.64-7.60 (m, 1H, aromatic proton), 7.52 (td, 1H, J_1 = 7.55 Hz, J_2 = 1.25 Hz, aromatic proton), 7.43 (td, 1H, J_1 = 7.9 Hz, J_2 = 1.7 Hz, aromatic proton), 7.40-7.34 (m, 2H, aromatic protons), 7.27-7.20 (m, 1H, aromatic proton), 4.79 (s, 2H, BrPhCH_2NCO), 4.65 (s, 2H, BrPhCH_2NCH_2CH_2), 4.08 (s, 2H, NCOCH_2N), 3.72 (t, 2H, J = 5.3 Hz, CONCH_2CH_2N), 3.61 (t, 2H, J = 5.8 Hz, CONCH_2CH_2N). ^{13}C NMR (125 MHz, CD_3OD, δ): 161.81, 134.07, 133.59, 133.13, 132.81, 132.02, 129.39, 129.18, 128.75, 128.42, 127.78, 125.57, 123.06, 59.29, 52.61, 49.49, 42.86. HRMS (ESI) *m/z*: calc. for [$C_{18}H_{18}Br_2N_2O$ + H]$^+$: 436.9840; ESI-MS-MS: 436.9840, 410.9855, 212.0059, 168.9639, 90.0462. ESI-MS m/z:

$[C_{18}H_{18}Br_2N_2O + Na]^+$: 460.9645; ESI-MS-MS: 460.9612, 406.2976, 308.9732, 253.0129, 170.9620, 91.0534. HPLC Rt = 4.392 min (mobile phase: CH_3CN/CH_3COONH_4 90/10; stationary phase: ZORBAX ECLIPSE Plus C18, analytical 4.6x250mm, 5 μm); rate = 1mL/min. The product was crystallized by hot/cold CH_3OH.

1,4-Bis(4-bromobenzyl)piperazin-2-one 15 (DA35). Orange oil; 16% yield. ^1H NMR (500 MHz, $CDCl_3$, δ): 7.44 (dd, 4H, J_1 = 8.3 Hz, J_2 = 1.5 Hz, aromatic protons), 7.18 (d, 2H, J = 8.3 Hz, aromatic protons), 7.13 (d, 2H, J = 8.3 Hz, aromatic protons), 4.53 (s, 2H, BrPhCH_2NCO), 3.50 (s, 2H, BrPhCH_2NCH$_2$), 3.22 (s, 2H, NCOCH_2N), 3.19 (t, 2H, J = 5.4 Hz, CONCH_2CH$_2$N), 2.61 (t, 2H, J = 5.35 Hz, CONCH$_2$CH_2N). ^{13}C NMR (125 MHz, $CDCl_3$, δ): 166.82, 135.56, 131.78, 131.59, 129.91, 130.64, 61.01, 57.27, 49.14, 48.92, 45.96. GC−MS (70 eV) (m/z) (rel. int.) 439(4),438 (M^+, 2), 437 (9), 410 (4), 409 (1),408 (6), 269 (39),268 (5), 267 (41),172 (8), 171 (97), 170 (8), 169 (100), 91 (8), 90 (45), 89 (30), 63 (5), 42 (25). HPLC Rt = 5.670 min (mobile phase: CH_3CN/H_2O 70/30; stationary phase: ZORBAX ECLIPSE Plus C18, analytical 4.6x250mm, 5 μm); rate = 1mL/min. The product was isolated by column chromatography (silica gel and EtOAc/hexane = 1/1 as the mobile phase).

1,4-Bis(4-chlorobenzyl)piperazin-2-one 16 (DA53). White solid, 21% yield. M.p 134-137 ºC. ^1H NMR (500 MHz, $CDCl_3$, δ): 7.46-7.35 (m, 4H, aromatic protons), 7.28-7.22 (m, 4H, aromatic protons), 4.84 (s, 4H, 2ClPhCH_2N), 3.46 (s, 4H, NCOCH_2, NCH$_2$CH$_2$), 2.17 (s, 2H, NCH$_2$CH_2). ^{13}C NMR (125 MHz, $CDCl_3$, δ): 157.49, 133.84, 132.98, 130.69, 129.74, 129.49, 127.47, 47.92, 44.02, 30.96, 29.69. HRMS (ESI) *m/z*: calc. for ESI-MS *m/z*: $[C_{18}H_{18}Cl_2N_2O + Na]^+$: 371.2749; ESI-MS-MS: 371.2749, 342.1111, 265.1137, 212.4230, 185.0124, 76.9972, 62.9828. HPLC Rt =4.178 min (fase mobile: H_2O/CH_3CN 30:70; fase stazionaria: ZORBAX ECLIPSE Plus C18, analytical 4.6x250mm, 5-Micron); flusso = 1mL/min. The product was isolated by column chromatography (silica gel and EtOAc/hexane = 6/4 as the mobile phase).

General synthesis 17-20. A mixture of 2-oxopiperazine (0.99 mmol) in anhydrous DMF (3 mL), $NaHCO_3$ (1.19 mmol), and the appropriate substituted-benzyl bromide (1.19 mmol) was stirred at 100 °C for 16 h. The reaction mixture was cooled to room temperature, and the solvent was removed under reduced pressure. CH_2Cl_2 was added to the reaction crude, and the solution was washed with brine. The organic layer was dried on anhydrous Na2SO4, and the solvent was evaporated under reduced pressure. The products were isolated by column chromatography (silica gel and EtOAc/MeOH = 9.8/0.2 as the mobile phase).

3-((3-Oxopiperazin-1-yl)methyl)benzonitrile 17 (DA10). White solid, 56% yield. M.p. 148-151°C. ^{1}H NMR (300 MHz, $CDCl_3$, δ): 7.65 (m, 1H, aromatic proton), 7.59-7.53 (m, 2H, aromatic protons), 7.44 (dd, 1H, J_1 = 8.01 Hz, J_2 = 7 Hz, aromatic proton), 6.69 (bs, 1H, NH), 3.60 (s, 2H, NCPhCH_2N), 3.41-3.32 (m, 2H, CONHCH_2CH$_2$N), 3.13 (s, 2H, HNCOCH_2N), 2.65 (t, 2H, J = 5.52 Hz, CONHCH$_2$CH_2N). HRMS (ESI) *m/z*: calc. for ESI-MS *m/z*: $[C_{12}H_{13}N_3O + Na]^+$: 238.0955; ESI-MS-MS: 238.0954, 201.6492, 183.1700, 149.0149, 100.1089, 76.9968, 62.9809. ESI-MS m/z: $[C_{12}H_{13}N_3O-H]^-$, 214.0995. ESI-MS-MS: 214.0992, 141.0459, 116.0513, 102.0352, 58.0300.

4-(4-Nitrobenzyl)piperazin-2-one 18 (DA22). White solid, 53% yield. M.p. 152-155 °C. ^{1}H NMR (300 MHz, $CDCl_3$, δ): 8.24-8.18 (m, 1H, aromatic proton), 8.18-8.08 (m, 1H, aromatic proton), 7.66-7.52 (m, 2H, aromatic protons), 6.78 (bs, 1H, NH), 3.68 (s, 2H, NO$_2$PhCH_2N), 3.41-3.34 (m, 2H, CONHCH_2CH$_2$N), 3.16 (s, 2H, NHCOCH_2), 2.68 (t, 2H, J = 5.5 Hz, CONHCH$_2$CH_2N). GC−MS (70 eV) (*m/z*) (rel. int.) 235 (M^+, 16), 206 (15), 165 (33), 136 (64), 99 (100), 90 (42), 42 (66).

4-(3-(Trifluoromethyl)benzyl)piperazin-2-one 19 (DA46). White solid, 46% yield. M.p. 88-90 °C. ^{1}H NMR (300 MHz, $CDCl_3$, δ): 7.63-7.39 (m, 4H, aromatic protons), 6.74 (bs, 1H, NH), 4.56 (s, 2H, CF_3PhCH_2N), 3.20-3.18 (m, 4H, COCH_2N, CONHCH_2CH$_2$N), 2.67 (t, 2H, J = 5.2 Hz, CONHCH$_2$CH_2N).

4-(4-(Trifluoromethyl)benzyl)piperazin-2-one (20) (DA40). White solid, 58% yield. M.p. 119-122 °C. ^{1}H NMR (500 MHz, $CDCl_3$, δ): 7.58 (d, 2H, *J* = 8 Hz, aromatic protons), 7.45 (d, 2H, *J* = 8 Hz, aromatic protons), 7.26 (bs, NH), 3.63 (s, 2H, CF_3PhCH_2N), 3.40-3.31 (m, 2H, $CONHCH_2CH_2$), 3.16 (s, 2H, $COCH_2N$), 2.64 (t, 2H, *J* = 5.4 Hz, $CONHCH_2CH_2N$). GC−MS (70 eV) (*m/z*) (rel. int.) 259 (M^+, 43), 229 (20), 188 (30), 159 (100), 99 (68), 42 (41).

General synthesis of 21-27. To suspension of NaH (60% dispersion in oil, 0.8 mmol) in anhydrous DMF (1 mL), was added dropwise a solution of **17**-**20** (0.4 mmol) in anhydrous DMF (2 mL), at 0 °C. The reaction mixture is left stirring at 0 °C for 30 minutes. The appropriate benzyl bromide (0.47 mmol) was added at the suspension and the reaction was left, under stirring, at 100 °C, overnight. The reaction mixture was cooled to room temperature and H_2O and EtOAc were added. The organic phase was washed with brine (x3) and dried over anhydrous Na_2SO_4. The solvent was evaporated under reduced pressure to give **21**−**27**.

4-(3-Cyanobenzyl)-1-(4-chlorobenzyl)piperazin-2-one 21 (DA11). White solid, 43% yield. M.p. 109-111 °C. ^{1}H NMR (500 MHz, $CDCl_3$, δ): 7.64 (s, 1H, aromatic proton), 7.58-7.55 (m, 2H, aromatic protons), 7.43 (t, 1H, *J* = 7.7 Hz, aromatic proton), 7.31-7.19 (m, 4H, aromatic protons), 4.56 (s, 2H, $ClPhCH_2NCO$), 3.58 (s, 2H, $NCPhCH_2N$), 3.25-3.22 (m, 4H, $CONCH_2CH_2N$, $NCOCH_2N$), 2.65 (t, 2H, *J* = 5.1 Hz, NCH_2CH_2NCO). ^{13}C NMR (125 MHz, $CDCl_3$, δ): 166.51, 138.49, 134.95, 133.49, 133.24, 132.30, 131.33, 129.58, 129.34, 128.86, 118.63, 112.69, 60.83, 57.19, 49.37, 48.90, 45.89. GC−MS (70 eV) (*m/z*) (rel. int.) 339 (M^+, 11), 310 (12), 223 (42), 125 (100), 116 (91), 89 (32), 63 (5), 42 (42). HPLC Rt = 4.557 min (mobile phase: CH_3CN/H_2O 70/30; stationary phase: ZORBAX ECLIPSE Plus C18, analytical 4.6x250mm, 5 μm); rate = 1mL/min. The product was isolated by column chromatography (silica gel and EtOAc/hexane = 8.5/1.5 as the mobile phase).

4-(3-Cyanobenzyl)-1-(4-(trifluoromethyl)benzyl)piperazin-2-one 22 (DA14). Green pale oil; 31% yield. ^{1}H NMR (500 MHz, $CDCl_3$, δ): 7.64 (s, 1H, aromatic proton), 7.62-7.53 (m, 3H,

aromatic protons), 7.49 (s, 1H, aromatic proton), 7.48-7.45 (m, 2H, aromatic protons), 7.44 (t, 1H, *J* = 7.65 Hz, aromatic proton), 4.65 (s, 2H, CF_3PhCH_2NCO), 3.61 (s, 2H, $CNPhCH_2N$), 3.32-3.19 (m, 4H, $NCOCH_2N$, $CONCH_2CH_2N$), 2.69 (t, 2H, *J* = 5.15 Hz, NCH_2CH_2NCO). ^{13}C NMR (125 MHz, $CDCl_3$, δ): 166.61, 137.47, 133.27, 132.32, 131.48, 131.47, 131.38, 130.04 (q, *J* = 32.1 Hz), 129.37, 129.31, 124.77 (q, *J* = 3.8 Hz), 124.55 (q, *J* = 3.7 Hz), 123.94 (q, *J* = 270.8 Hz), 118.59, 112.72, 60.80, 49.34, 49.18, 46.05. GC−MS (70 eV) (*m/z*) (rel. int.) 374 (4), 373 (M^+, 17), 354 (5), 344 (31), 257 (100), 214 (8), 200 (6), 159 (82), 116 (99), 89 (22), 42 (42). HPLC Rt = 4.736 min (mobile phase: CH_3CN/H_2O 70/30; stationary phase: ZORBAX ECLIPSE Plus C18, analytical 4.6x250mm, 5 μm); rate = 1mL/min. The product was isolated by column chromatography (silica gel and EtOAc/hexane = 9/1 as the mobile phase).

3-((4-(4-Fluorobenzyl)-3-oxopiperazin-1-yl)methyl)benzonitrile 23 (DA25)**.** Yellow oil; 35% yield. ^1H NMR (500 MHz, $CDCl_3$, δ): 7.62 (s, 1H, aromatic proton), 7.58-7.52 (m, 2H, aromatic protons), 7.43 (t, 1H, *J* = 7.7 Hz, aromatic proton), 7.25-7.20 (m, 2H, aromatic protons), 7.03-6.97 (m, 2H, aromatic protons), 4.55 (s, 2H, $FPhCH_2NCO$), 3.57 (s, 2H, $CNPhCH_2N$), 3.26-3.18 (m, 4H, $NCOCH_2N$, $CONCH_2CH_2N$), 2.64 (t, 2H, *J* = 5.7 Hz, $CONCH_2CH_2N$). ^{13}C NMR (125 MHz, $CDCl_3$, δ): 166.65, 162.27 (d, *J* = 244.65 Hz), 138.62, 133.23, 132.27, 131.26, 129.90 (d, *J* = 8.05 Hz), 129.33, 129.32, 118.65, 115.56 (d, *J* = 21.35 Hz), 112.65, 60.82, 57.23, 49.36, 48.85, 45.87. GC−MS (70 eV) (*m/z*) (rel. int.) 323 (M^+, 10), 294 (11), 207 (38), 116 (61), 109 (100), 89 (16), 42 (29). HPLC Rt = 3.823 min (mobile phase: CH_3CN/H_2O 70/30; stationary phase: ZORBAX ECLIPSE Plus C18, analytical 4.6x250mm, 5 μm); rate = 1mL/min. The product was isolated by column chromatography (silica gel and EtOAc/hexane = 9/1 as the mobile phase).

4-(3-Cyanobenzyl)-1-(3,4-dichlorobenzyl)piperazin-2-one 24 (DA26). Orange oil; 98% yield. ^1H NMR (300 MHz, CDCl3, δ): 7.66-7.62 (m, 1H, aromatic proton),7.61-7.53 (m, 2H, aromatic protons), 7.48-7.39 (m, 2H, aromatic protons),7.36 (d, 1H, *J* = 2.01 Hz, aromatic proton), 7.12 (dd, 1H, J_1 = 8.22 Hz, J_2 = 3.0 Hz, aromatic proton), 4.54 (s, 2H, $bisClPhCH_2NCO$), 3.59 (s, 2H,

CNPhC*H*$_2$NCH$_2$), 3.29-3.19 (m, 4H, NCOC*H*$_2$N, CONC*H*$_2$CH$_2$N), 2.67 (t, 2H, *J* = 5.37 Hz, NC*H*$_2$CH$_2$NCO). ^{13}C NMR (125 MHz, $CDCl_3$, δ): 166.41, 137.18, 136.67, 133.33, 132.78, 132.39, 131.82, 131.45, 130.73, 130.06, 129.41, 127.56, 118.57, 112.75, 60.75, 56.99, 49.27, 48.63, 45.97. GC−MS (70 eV) (*m/z*) (rel. int.) 393 (M^+, 11), 364 (24), 258 (14), 257 (100), 159 (89), 136 (64), 90 (46), 89 (22), 42 (53). HPLC Rt = 5.616 min (mobile phase: CH_3CN/CH_3COONH_4 70/30; stationary phase: ZORBAX ECLIPSE Plus C18, analytical 4.6x250mm, 5 μm); rate = 1mL/min. The product was isolated by column chromatography (silica gel and EtOAc/MeOH = 9.8/0.2 as the mobile phase).

4-(3-Nitrobenzyl)-1-(3-(trifluoromethyl)benzyl)piperazin-2-one 25 (DA23). Orange oil; 60% yield. ^{1}H NMR (300 MHz, $CDCl_3$, δ): 8.24-8.10 (m, 2H, aromatic protons), 7.67 (d, 1H, *J* = 7.6 Hz, aromatic proton), 7.59-7.44 (m, 5H, aromatic protons), 4.66 (s, 2H, CF_3PhC*H*$_2$NCO), 3.67 (s, 2H, NO_2PhC*H*$_2$N), 3.31-3.22 (m, 4H, NCOC*H*$_2$N, CONC*H*$_2$CH$_2$N), 2.70 (t, 2H, *J* = 5.6 Hz, NC*H*$_2$CH$_2$NCO). ^{13}C NMR (125 MHz, $CDCl_3$, δ): 166.84, 148.40, 139.25, 137.54, 134.90, 131.48, 131.47, 130.96 (q, *J* = 32.1 Hz), 129.49, 129.31, 124.74 (q, *J* = 3.68 Hz), 124.51 (q, *J* = 3.7 Hz), 123.62, 123.97 (q, *J* = 271 Hz), 122.66, 60.79, 57.19, 49.41, 49.16, 46.18. GC−MS (70 eV) (*m/z*) (rel. int.) 393 (M^+, 11), 364 (24), 258 (14), 257 (100), 159 (89), 136 (64), 90 (46), 89 (22), 42 (53). HPLC Rt = 5.385 min (mobile phase: CH_3CN/H_2O 70/30; stationary phase: ZORBAX ECLIPSE Plus C18, analytical 4.6x250mm, 5 μm); rate = 1mL/min. The product was isolated by column chromatography (silica gel and CH_2Cl_2/EtOAc = 9/1 as the mobile phase).

4-(3-(Trifluoromethyl)benzyl)-1-(4-(trifluoromethyl)benzyl)piperazin-2-one 26(DA29). Orange oil; 25% yield. ^{1}H NMR (300 MHz, $CDCl_3$, δ): 7.65-7.42 (m, 6H, aromatic protons), 7.38 (d, 2H, *J* = 8.13 Hz, aromatic protons), 4.65 (s, 2H, CF_3PhC*H*$_2$NCO), 3.62 (s, 2H, CF_3PhC*H*$_2$N), 3.31-3.19 (m, 4H, NCOC*H*$_2$N, CONC*H*$_2$CH$_2$N), 2.67 (t, 2H, *J* = 5.43 Hz, NC*H*$_2$CH$_2$NCO). ^{13}C NMR (125 MHz, $CDCl_3$, δ): 157.31, 140.33, 136.38, 132.62, 131.73, 131.02 (q, *J* = 32.63 Hz), 129.96 (q, *J* = 32.3 Hz), 129.62, 129.17, 128.59, 128.49, 128.32, 125.99, 125.97, 125.95, 125.92,

125.85, 125.83, 125.79, 125.68 (q, *J* = 3.7 Hz), 125.18, 125.15, 125.12, 124.98, 124.95, 124.92, 124.84, 124 (q, J = 270.56 Hz), 123.94 (q, J = 270.96 Hz), 61.00, 50.35, 49.22, 49.11, 49.73. GC−MS (70 eV) *(m/z*) (rel. int.) 416 (M^+, 11), 387 (18), 257 (62), 200 (6), 159 (100), 109 (16), 42 (17). HPLC Rt = 4.777 min (mobile phase: CH_3CN/H_2O 70/30; stationary phase: ZORBAX ECLIPSE Plus C18, analytical 4.6x250mm, 5 μm); rate = 1mL/min. The product was isolated by column chromatography (silica gel and EtOAc/hexane = 7/3 as the mobile phase).

1-(3-Bromo-4-fluorobenzyl)-4-(4-(trifluoromethyl)benzyl)piperazin-2-one 27 (DA42). Light brown solid, 42% yield. M.p. 83-86. ^{1}H NMR (500 MHz, CD_3OD, δ): 7.63 (d, 2H, *J* = 8.2 Hz, aromatic protons), 7.59-7.51 (m, 3H, aromatic protons), 7.14 (dd, 1H, J_1 = 9.5 Hz, J_2 = 1.7 Hz, aromatic proton), 7.03 (dd, 1H, J_1 =8.2 Hz, J_2 = 1.7 Hz, aromatic proton), 4.57 (s, 2H, Br,FPhCH_2NCO), 3.68 (s, 2H, CF_3PhCH_2N), 3.34-3.31 (m, 2H, CONC$H_2$$CH_2$N), 3.23 (s, 2H, NCOC$H_2$N), 2.72 (t, 2H, *J* = 5.6 Hz, NC$H_2$$CH_2$NCO). ^{13}C NMR (125 MHz, CD_3OD, δ): 167.91, 159.03 (d, *J* = 245.3 Hz), 141.51, 138.87 (d, *J* = 6.6 Hz), 129.38 (q, *J* = 32 Hz), 128.33, 124.96 (q, *J* = 3.7 Hz), 124.83 (d, *J* = 3.4 Hz), 124.26 (q, *J* = 269.7 Hz), 115.66 (q, *J* = 22.7 Hz), 107.18 (d, *J* = 20.9 Hz), 60.27, 56.41, 48.69, 46.09. GC−MS (70 eV) (*m/z*) (rel. int.) 446 (2), 445 (M^+, 10), 444 (2), 443 (10), 418 (2), 417 (10), 416 (2), 415 (11), 288 (6), 287 (48), 286 (7), 285 (50), 189 (44), 188 (5), 187 (47), 160 (9), 159 (100), 109 (22), 108 (17), 107 (11), 42 (28). HPLC Rt = 4.893 min (mobile phase: CH_3CN/H_2O 70/30; stationary phase: ZORBAX ECLIPSE Plus C18, analytical 4.6x250mm, 5 μm); rate = 1mL/min. The product was isolated by column chromatography (silica gel and EtOAc/MeOH = 9.8/0.2 as the mobile phase).

General synthesis of 32-33. A stirred suspension of 2,5-piperazinedione (0.876 mmol) and NaH (1.927 mmol) in anhydrous DMF (3 mL) was left at 0 °C for 30 minutes. After this time was added at room temperature the appropriate substituted benzyl bromide (1.199 mmol) and the reaction were stirring for 16h at room temperature. To the reaction mixture was added H_2O and was concentrated

under reduced pressure. EtOAc was added to the residue, and the solution was washed with a saturated solution of NH_4Cl and with brine. The organic layer was dried on anhydrous Na2SO4, and the solvent was evaporated under reduced pressure. The resulting oil underwent column chromatography on silica gel to give 33 and 34.

1,4-Dibenzylpiperazine-2,5-dione 33(DA28). White solid, 58% yield. M.p. 176-180 °C. ^{1}H NMR (500 MHz, $CDCl_3$, δ): 7.37-7.29 (m, 6H, aromatic protons), 7.29-7.24 (m, 4H, aromatic protons), 4.58 (s, 4H, 2PhC*H*$_2$NCO), 3.93 (s, 4H, 2NCOC*H*$_2$NCO). ^{13}C NMR (125 MHz, $CDCl_3$, δ): 163.25, 134.92, 128.94, 128.54, 128.21, 49.29, 49.21. GC−MS (70 eV) (*m/z*) (rel. int.) 294 (M^+, 19), 203 (1), 175 (4), 118 (6), 106 (6), 91 (100), 65 (11), 42 (5). HPLC Rt = 4.085 min (mobile phase: CH_3CN/H_2O 70/30; stationary phase: ZORBAX ECLIPSE Plus C18, analytical 4.6x250mm, 5 μm); rate = 1mL/min. The product was isolated by column chromatography (silica gel and EtOAc/hexane = 6/4 as the mobile phase).

1,4-Bis(3-(trifluoromethyl)benzyl)piperazine-2,5-dione 34 (DA34). White solid, 30% yield. M.p. 133-137 °C. ^{1}H NMR (500 MHz, $CDCl_3$, δ): 7.61-7.57 (m, 2H, aromatic protons), 7.53 (s, 2H, aromatic protons), 7.51-7.46 (m, 4H, aromatic protons), 4.64 (s, 4H, 2PhC*H*$_2$NCO), 3.97 (s, 4H, 2CONC*H*$_2$CON). ^{13}C NMR (125 MHz, $CDCl_3$, δ): 163.15, 135.96, 131.79, 131.42 (q, *J* = 32.3 Hz), 129.57, 125.20 (sextet, *J* = 3.7 Hz), 123.76 (q, *J* = 271 Hz), 49.32, 48.99. GC−MS (70 eV) (*m/z*) (rel. int.) 416 (M^+, 11), 387 (18), 257 (62), 200 (6), 159 (100), 109 (16), 42 (17). HPLC Rt = 4.111min (mobile phase: CH_3CN/H_2O 70/30; stationary phase: ZORBAX ECLIPSE Plus C18, analytical 4.6x250mm, 5 μm); rate = 1mL/min. The product was isolated by column chromatography (silica gel and EtOAc/hexane = 6/4 as the mobile phase).

Synthesis of 31 (DA45).

Tert-butyl 3-oxopiperazine-1-carboxylate 28 (DA41). To a suspension of 2-oxopiperazine (0.200 g; 2 mmol) in anhydrous CH_2Cl_2 (5 mL), is added a solution of Di-*tert*-butyl dicarbonate (0.479 g; 2.2 mmol) in anhydrous CH_2Cl_2 (5 mL), dropwise at 0ºC. The mixture was stirred for 3 h at room

temperature. The organic layer was washed with brine. The organic extracts were dried over anhydrous Na_2SO_4, and the solvent evaporated under reduced pressure to give the compound **28**. White solid, 86% yield. M.p. 164-168 °C[177]. ^{1}H NMR (300 MHz, $CDCl_3$, δ): 6.41 (br s, 1H, N*H*CO), 4.10 (s, 2H, NHCOC*H*$_2$N), 3.64 (t, 2H, *J* = 5 Hz, NCH$_2$C*H*$_2$NBoc), 3.35-3.44 (m, 2H, J = 5 Hz, NC*H*$_2$CH$_2$NBoc), 1.48 (s, 9H, C(C*H*$_3$)$_3$). HRMS (ESI) *m/z*: calc. for ESI-MS *m/z*: $[C_9H_{16}N_2O_3+Na]^+$: 223.1081; ESI-MS-MS: 223.1054, 187.6279, 167.0421, 128.9449, 95.0572, 76.9985, 62.9815. ESI-MS m/z: $[C_9H_{16}N_2O_3-H]^-$, 199.1083. ESI-MS-MS: 199.1082, 99.0566, 70.0300, 57.0345.

Tert-butyl 3-oxo-4-(4-(trifluoromethyl)benzyl)piperazine-1-carboxylate 29 (DA43). To a suspension of NaH, (60% dispersion in mineral oil, 0.048 g; 2 mmol) in anhydrous DMF (1 mL), was added a solution of **28** (0.200 g; 1 mmol) in anhydrous DMF (2.5 mL) at 0ºC. The mixture was stirring for 30 min at the same temperature. Then, 4-(trifluoromethyl)benzyl bromide (0.286 g; 1.2 mmol) was added, and the mixture was left stirring at 100 ºC, overnight. After cooling, to the reaction mixture was added H_2O and was concentrated under reduced pressure. EtOAc was added to the residue, and the solution was washed with brine. The organic extracts were dried over anhydrous Na_2SO_4, and the solvent evaporated under reduced pressure. The product was isolated by column chromatography (silica gel and EtOAc/hexane = 6/4 as the mobile phase). Yellow solid, 53% yield. M.p.142-144 °C. ^{1}H NMR (500 MHz, $CDCl_3$, δ): 7.59 (d, 2H, *J* = 8.2 Hz, aromatic protons), 7.38 (d, 2H, *J* = 8.15 Hz, aromatic protons), 4.67 (s, 2H, CF_3PhC*H*$_2$N), 4.17 (s, 2H, NCOC*H*$_2$N), 3.61 (t, 2H, *J* = 5.3 Hz, PhNC*H*$_2$CH$_2$N), 3.27 (t, 2H, *J* = 5.1 Hz, NC*H*$_2$CH$_2$NCO), 1.46 (s, 9H, C(C*H*$_3$)$_3$). HRMS (ESI) *m/z*: calc. for ESI-MS m/z: $[C_{17}H_{21}F_3N_2O_3+Na]^+$: 381.1406; ESI-MS-MS: 381.1405, 325.0776, 281.0870, 254.1047, 76.9973.

1-(4-(Trifluoromethyl)benzyl)piperazin-2-one 30 (DA44). An excess of CF_3CO_2H (2.81 mmol, 0.5 ml) was added to a solution of **29** in CH_2Cl_2 (3 mL). The reaction mixture was left stirring for 5h at room temperature. The solvent was concentrated under reduced pressure, and the product was

used in the next step without any further purification. Yellow solid; quantitative yield. M.p. 126-130 °C. ^{1}H NMR (500 MHz, $CDCl_3$, δ): 7.59 (d, 2H, *J* = 7.9 Hz, aromatic protons), 7.36 (d, 2H, *J* = 7.9 Hz, aromatic protons), 4.66 (s, 2H, CF_3PhCH_2N), 3.92 (s, 2H, $NCOCH_2NH$), 3.51 (t, 2H, *J* = 5.1 Hz, $CONCH_2CH_2NH$), 3.39 (t, 2H, *J* = 5.45Hz, $HNCH_2CH_2N$). GC−MS (70 eV) (*m/z*) (rel. int.) 258 (M^+, 54), 188 (35), 159 (100), 109 (22), 99 (33), 56 (23), 42 (29).

4-(2-(3,4-Dichlorophenyl)acetyl)-1-(4-(trifluoromethyl)benzyl)piperazin-2-one 31 (DA45). To a solution of **29** (0.100 g; 0.39 mmol) in CH_2Cl_2 (3 mL) was added, dropwise, a solution of 3,4-dichlorophenylacetyl chloride in CH_2Cl_2 (2 mL) at 0 ºC. The mixture was left stirring at room temperature, overnight. After this time, the solvent was concentrated under reduced pressure. The crude product was purified by fractional crystallization of hot/cold diethyl ether. The product **31** was obtained as a white solid, 53% yield. M.p.159-162 ºC. ^{1}H NMR (500 MHz, DMSO, δ): 7.74-7.66 (m, 2H, aromatic protons), 7.53 (t, 1H, *J* = 8.7 Hz, aromatic proton), 7.49-7.41 (m, 3H, aromatic protons), 7.19 (d, 2H, *J* = 8.25 Hz, aromatic protons), 4.62 (s, 2H, CF_3PhCH_2NCO), 4.28 (s, 1H, NCOC*H*HN), 4.11 (s, 1H, NCOCH*H*N), 3.80-3.74 (m, 3H, bisClCH_2CO, CONC*H*HCH_2NCH_2), 3.68 (t, 1H, *J* = 4.9 Hz, CONCH*H*CH_2NCH_2), 3.31-3.28 (m, 1H, $CONCH_2CHHNCH_2$), 3.26 (t, 1H, *J* = 5 Hz, $CONCH_2CH$*HCH*$_2$). ^{13}C NMR (125 MHz, DMSO, δ): 168.70, 165.70, 142.22, 137.27, 131.02, 131.97, 130.63, 130.49, 130.39, 129.53, 128.78, 128.71, 128.48, 128.23, 125.90, 125.88, 125.85, 125.78, 123.62, 46.33, 45.87, 42.66, 38.38, 38.22. HRMS (ESI) *m/z*: calc. for ESI-MS *m/z*: $[C_{20}H_{17}Cl_2F_3N_2O_2+Na]^+$: 467.0526; ESI-MS-MS: 467.0524, 435.2174, 374,9542, 326.2443, 185.0144, 104.9924, 76.9978. ESI-MS *m/z*: $[C_{20}H_{17}Cl_2F_3N_2O_2+Cl]^-$, 479.0302. ESI-MS-MS:479.0316, 443.0513, 283.0695, 257.0893, 184.9588, 158.9774, 82.0310. HPLC Rt = 4.509 min (mobile phase: CH_3CN/H_2O 70/30; stationary phase: ZORBAX ECLIPSE Plus C18, analytical 4.6x250mm, 5 μm); rate = 1mL/min.

General synthesis of 36-37. To a stirred suspension of 1-acetylpiperazine (2.34 mmol) and K_2CO_3 (3.04 mmol) in CH_3CN (14 mL) was added the appropriate benzyl bromide (2.57 mmol). The

reaction mixture was stirred at room temperature for 3 h. The reaction progress was monitored by TLC (CH_2Cl_2/MeOH = 9.5/0.5 as mobile phase). Then, the resulting solid was filtered and repeatedly washed with EtOAc. The organic filtrate was concentrated under reduced pression, and the resulting oil underwent to chromatography on silica gel and CH_2Cl_2/MeOH = 9.5/05 as mobile phase.

1-(4-(4-Chlorobenzyl)piperazin-1-yl)ethan-1-one 36 (DA5). Orange oil; 57% yield. ^{1}H NMR (300 MHz, $CDCl_3$, δ): 7.34-7.20 (m, 4H, aromatic protons), 3.62 (t, 2H, *J* = 5. Hz, CONC*H*$_2$), 3.49 (s, 2H, ClPhC*H*$_2$N), 3.45 (t, 2H, *J* = 5.2 Hz, CONC*H*$_2$), 2.52-2.31 (m, 4H, C*H*$_2$NC*H*$_2$), 2.07 (s, 3H, C*H*$_3$CO). GC−MS (70 eV) (*m/z*) (rel. int.) 252 (M^+, 7), 180 (33), 168 (26), 125 (100), 85 (30), 56 (13), 42 (19).

3-((4-Acetylpiperazin-1-yl)methyl)benzonitrile 37 (DA6). Orange oil; 55% yield. ^{1}H NMR (300 MHz, $CDCl_3$, δ): 7.66 (m, 1H, aromatic proton), 7.61-7.51 (m, 2H, aromatic protons), 7.43 (t, 1H, *J* = 7.7 Hz, aromatic proton), 3.63 (t, 2H, *J* = 5 Hz, CONC*H*$_2$), 3.54 (s, 2H, CNPhC*H*$_2$N), 3.47 (t, 2H, J = 5.1 Hz, CONC*H*$_2$), 2.52-2.30 (m, 4H, C*H*$_2$NC*H*$_2$), 2.08 (s, 3H, C*H*$_3$CO). GC−MS (70 eV) (*m/z*) (rel. int.) 243 (M^+, 6), 200 (10), 171 (81), 159 (39), 116 (100), 89 (22), 56 (23), 42 (27).

BIOLOGICAL SECTION

Expression of *h*ClpP-His6 recombinant protein. The recombinant protein was expressed in *E. coli* BL21-Codon Plus (DE3)-RIL cells. A single colony was picked and inoculated into 10 ml of LB broth containing 0.1 mg/ml ampicillin, in a 50 ml Falcon tube. The culture was grown overnight at 37 °C with shaking. The next day, 2.5 ml of the overnight culture was transferred into 250 ml of LB broth containing ampicillin, in a 1-liter flask, and grown at 37° C with shaking until the OD_{600} was 0.5–0.6 (approximately 2 hours). Expression was induced by adding IPTG to a final concentration of 0.5 mM, and the culture was grown at 22 °C for 22 hours with vigorous shaking.

Cells were harvested by centrifugation at 6000xg, 15 min, at + 4 °C. To remove culture medium, pellets were rinsed with cold PBS 1x. Briefly, pellets were resuspended in a small volume of PBS1x by pipetting up/down with a 10 ml disposable pipette and centrifuged as before. Tubes were always kept on ice. Finally, the tube was thoroughly drained by placing it upside down on the bench, fast freeze in liquid nitrogen, and stored at -80°C.

Extraction and purification of *h*ClpP recombinant protein. Bacterial pellets from a 250 ml induced culture were resuspended in 20 ml of Lysis/binding buffer (25 mM Tris/HCl pH 7,8, 150 mM NaCl, 10% glycerol) containing 5 mM imidazole, by pipetting up/down. The mixture was added with 1 ml of freshly prepared 20 mg/ml lysozime in 10 mM Tris/HCl pH 8.0 and incubated on ice for 30 min with occasional swirling. Cells were lysed by sonicating in ice/water with the Vibracell Sonics (large probe), 30 sec pulse, 30 sec pause, amplitude 40%, for total 60 min until the suspension became limpid. The lysate was clarified by ultracentrifugation at 100,000 x g, then the supernatant was filtered through a 0.45 nitrocellulose filter.

Affinity purification (Immobilized Metal Ion Affinity Chromatography, IMAC) of hClpP-His6 recombinant protein. All the chromatography steps were performed in the cold room. Protein purification was achieved by immobilized metal ion affinity chromatography (IMAC) using Ni-NTA prepacked column (GE). The lysate was applied on a 1-ml or 5-ml prepacked column equilibrated with 10 column volumes (50 ml) of Lysis/binding buffer containing 5 mM imidazole. Loading was made at a flow rate of 0.15 ml/min. The flow-through was discarded. The resin was washed with 10 column volumes of Lysis/binding buffer containing 5 mM imidazole at a flow rate of 0.3 ml/min. For the first chromatography with 1-ml prepacked column, we did a first elution with 5 ml of Lysis/binding buffer containing 30 mM imidazole at a flow rate of 0.2 ml/min to remove loosely bound protein and we collected ten 0.5ml fractions of the efluent to monitor by western blotting the strength of hClpP-6xHis binding to the resin in the presence of 30 mM imidazole. Human hClpP- 6xHis was eluted using 5 column volumes (5 ml) of Lysis/binding buffer containing

300 mM imidazole at a flow rate of 0.2 ml/min; ten 0.5 ml fractions were collected. The protein usually elutes between the fourth and fifth fraction, peaking in the fourth. For the second chromatography with 1-ml prepacked column, we performed a first elution with 5 ml of Lysis/binding buffer containing 100 mM imidazole at a flow rate of 0.2 ml/min and we collected ten 0.5ml fractions of the eluent. Human hClpP-6xHis was eluted using 5 column volumes (5 ml) of Lysis/binding buffer containing 300 mM imidazole at a flow rate of 0.2 ml/min; ten 0.5 ml fractions were collected. The protein usually elutes between the third and fifth fraction, peaking in the fourth. For the third chromatography with 5-ml prepacked columns, we performed a first elution with 25 ml of Lysis/binding buffer containing 50 mM imidazole at a flow rate of 0.2 ml/min and we collected twenty-five 1ml fractions of the eluent. Having assessed that the protein did not elute at this imidazole concentration, we no longer collected fractions of the eluent. Human *h*ClpP-6xHis was eluted using 5 column volumes (25 ml) of Lysis/binding buffer containing 300 mM imidazole at a flow rate of 0.2 ml/min; twenty-five 1 ml fractions were collected. The protein usually elutes between the seven and ten fractions, peaking in the eight. After elution, the column was regenerated in the cold room by washing with 10 column volumes of 1M imidazole solution, followed by equilibration with 10 column volumes of Lysis/binding buffer containing 5 mM imidazole. After that, the column, stored in the cold room, was ready for a new purification.

***h*ClpP + DA29 crystallization and structural refinement.** *h*ClpP was incubated at 10 mg/mL in a stoichiometric ratio of 1:3 with **26** (DA29) dissolved in DMSO. This solution was then mixed 1:1 with crystallization solution (0.2 M $MgCl_2$, 25%w/v PEG 3350, 0.1 M BIS-TRIS pH 5.5, on plates for sitting drop vapour diffusion crystallization at room temperature. The resulting crystals were frozen in liquid nitrogen using the crystallization solution supplemented with an additional 20% glycerol as cryo-protectant. Diffraction data was collected with 0.979338 Å wavelength X-rays at the National Synchrotron Light Source II at Brookhaven National Laboratory (Upton, New York,

USA) Beamline 17-ID-2. Diffraction data was indexed, integrated, and scaled using autoPROC 1.0.5[178] Molecular replacement was performed in Phenix Phaser[179]. The search model was a structure of *h*ClpP bound to ONC201 (PDBID: 6DL7). The ONC201 molecules were removed from the PDB prior to molecular replacement. Subsequent model building and refinements were performed in Coot[180] and Phenix[181] and involved the optimization of atomic coordinates, B-factor, and occupancy. Clear difference density for DA29 was found in the electron density maps and was confirmed by calculating a composite omit map. The final structure has good geometry, with 96% of residues in Ramachandran favoured regions and no Ramachandran outliers.

***h*ClpP activity test**. FITC-casein assay was performed to assess the potency of the proteolytic activity of *h*ClpP. In a black, flatbottom, 96-well plate, purified 2 μM *h*ClpP in assay buffer (AB) (50 mM *N*-(2-hydroxyethyl)piperazine-*N*′-ethanesulfonic acid (HEPES), pH 7.5, 300mMKCl, 1mMDTT, 15% v/v glycerol; AB) preincubated at 37 °C for 15 min was added to 5 μL of the tested compounds in dimethyl sulfoxide (DMSO) at different concentrations (1-100 μM)and incubated for 15 min at 37 °C under shaking. As a control, three wells were filled with 5 μL of DMSO. The kinetic measurement was started after adding 2 μM fluorogenic FITC-casein (Merck, C3777), used as the enzyme substrate. The FITC fluorescence from the hydrolyzed FITC-casein was recorded over 60 min at 37 °C on a TecanInfinite M200 Pro (λ_{ex} = 485 nm, λ_{em} = 535 nm, gain: 60). The slope in the linear range between 480 and 1200 s was determined and plotted against time. The EC_{50} for each tested compound was calculated using GraphPad Prism 7.05. Results are reported as the mean of two independent experiments performed in triplicate.

Cellular Thermal Shift Assay. Caco-2 cells were preincubated for 1 h with compounds solubilized in DMSO at a final concentration of 20 μM or DMSO alone as control experiment at the concentration of 0.04%. 100 μL of treated cells was aliquoted into polymerase chain reaction (PCR)

tubes (Qiagen) and heated in a SensoQuest 96-well Thermal Cycler (Diatech Pharmacogenetics) at the indicated temperature range for 3 min. Immediately following heating, the aliquots were equilibrated to room temperature (3 min). Subsequently, the cells were rapidly frozen in liquid nitrogen to extract their contents and immediately centrifuged at 14,000 rpm for 20 min at 4 °C to separate soluble from insoluble fragments. The supernatant was carefully aspirated and subjected to Western blotting under reducing conditions. The soluble fractions were solubilized in 2× Laemmli and separated onto 10% Tris-Glycine-SDS minigels (Bio-Rad) and then transferred onto 0.2 μm nitrocellulose membranes using the Trans-Blot Turbo Transfer System (Bio-Rad). Membranes were blocked for 1 h at room temperature with blocking buffer (5% non-fat dry milk, 0.1% Tween-20 in Tris-buffered saline, TBS). The membranes were probed with anti-hClpP polyclonal primary antibody (Product #PA5-52722, Thermo Fisher) at a dilution of 1:1000 at 4 °C overnight, diluted in 5% bovine serum albumin in TBST. After incubation time, membranes were washed ×3 with TBST and incubated with a secondary peroxidase antibody (1:3000 antirabbit) for 1 h at room temperature. After repeated washing, the membranes were treated with the Clarity Western ECL substrate (Bio-Rad) according to the manufacturers instructions, and the blot was visualized by iBright FL1000 Imaging Systems (Thermo Fisher Scientific).

Cell Cultures. Patient-derived DIPG cell cultures (SU-DIPG-36, SU-DIPG-50) were kindly provided by Prof. Michelle Monje of Institutional Review Board (Stanford University and Prof. Javad Nazarian). The cells were cultured as a monolayer in media that was changed once a week at 37 °C in 5% CO_2 by using Tumor Stem Media composed by a 1:1 ratio of DMEM/F12 (Invitrogen)/Neurobasal (-A) (Invitrogen), B27 (-A) (LifeTechnologies, Milan, Italy), 20 ng/mL human basic fibroblast growth factor (Life Technologies), 20 ng/mL recombinant human epidermal growth factor (Life Technologies), 10 ng/mL platelet-derived growth factor-AA, 10 ng/mL platelet-derived growth factor-BB (Life Technologies), and 20 ng/mL heparin (StemCell Technologies, Milan, Italy).19 Caco-2 cells were grown in Dulbeccos high-glucose modified Eagle medium,

composed of 10% fetal bovine serum, 2 mM glutamine, 100 U/mL penicillin, and 0.1 mg/mL streptomycin (all components purchased from Euroclone, Milan, Italy).

Cytotoxic Assay. The cytotoxicity assay was conducted seeding cells at a density of 10,000 cells/well for 24 h in a 96-well plate (Corning, NY, USA) and incubated overnight at 37 °C in a 5% CO_2 atmosphere. Subsequently, the culture medium was replaced with 100 μL of fresh medium containing dilutions of drug ranging from 1 to 100 μM and incubated at 37 °C for 72 h. Drug-solvent DMSO was added to each control to evaluate a possible solvent cytotoxicity. After the incubation time with each compound, CCK-8 (10 μL) was added to each well, and after 3-4 h of incubation at 37 °C, the absorbance values at λ = 450 nm were determined on the Tecan Infinite 200 microplate reader Tecan Infinite 200. IC_{50} values were obtained by using GraphPad Prism software.

Drug Transport Experiments. The experiment started with the preparation of the Caco-2 monolayer, which occurred by seeding the cells (20,000/well) in Millicell plates (Millipore, Milan, Italy). Its growth was followed for 21 days by changing the medium occasionally and measuring its transepithelial electrical resistance daily using an epithelial voltohmmeter (Millicell-ERS) until at least 1000W was reached. After 21 days, the plate was washed twice with Hanks balanced salt solution (HBSS) (Invitrogen). After the second wash, the wells were filled with buffer, and the plate was kept at 37 °C for 30 min. After the incubation time, the HBSS buffer was replaced with the solutions of the compounds to be tested at a concentration equal to 10^{-4} M. The plates were placed in an incubator at 37 °C for 2 h. The apparent permeability (Papp) was calculated in units of nm/s. The calcein-AM assay[182] revealed that **26** (DA29) shows only a weak interaction with P-gp (EC_{50} = 71 μM), indicating that it is poorly retained in cells[88,91]. Its limited effect on P-gp efflux suggests minimal transporter-mediated restriction, consistent with its low intracellular accumulation.

Dynamic Permeability Assay Using Caco-2 Cells in the LiveBox2 Bioreactor System. LiveFlow® peristaltic pump was purchased from IVTech Srl (IVTech Srl., Massarosa, LU, Italy) together with the LiveBox2 (LB2) bioreactor. The LiveBox2 is composed of three parts: an apical

chamber, with an inlet, an outlet and a wet volume of 1 mL; a basal chamber, with an inlet and an outlet tube and a wet volume of 1.5 mL and a membrane holder, which is placed between the two chambers. The two chambers are made in polydimethylsiloxane (PDMS; Sylgard 184, Dow Corning, Silverstar, Italy), a bio- compatible silicone polymer, and they set up two independent fluidic circuits, respectively. Each circuit is connected to a pump and a mixing chamber, which serves as a media reservoir and for oxygenation. The holder is composed of two annuli, which snugly holds a polyethylene terephthalate (PET) semi-permeable membrane (pore size: 0.45 μm; 2×10^6 pores/cm^2; ipCELLCULTURE, it4ip, Louvain-la-Neuve, Belgium) and it is placed between the two chambers.

After all the components were sterilized and the LiveBox2 was assembled under a laminar flow hood, the membrane was treated with a 0.01% solution of Poly-L-Lysine (Sciencell Research Laboratories 0413, Catalog No.NC9951372) for 1h at 37 °C. Then, the membrane was washed two times with sterile water.

Caco-2 cells were seeded with a density of $5x10^4$ cells/cm^2 onto the membrane in the LB2. The media was changed every three days, and the cells were used for experiments after 8 days from seeding. To precondition the cell monolayer to dynamic conditions, the LB2 was connected to the peristaltic pump LiveFlow, using a laminar flow of 100 μL/min and the entire system was placed in the cell culture incubator at 37℃ with 5% CO_2. After 24 hours, both apical and basal circuits were emptied out and media in the mixing chambers was rapidly replaced with fresh media for the basal circuit and with media containing compound for the apical circuit. The flow rate was increased to 150 μL/min, which according to the manufacturer should provide an average shear stress of around 6×10^{-4} Pa on the membrane, which is within the physiological range.

When the circuits are filled, media samples of 100 μL were withdrawn from upper circuit at various time points (0, 1, 2, 4, 6 h) and analyzed using HPLC performed on an Agilent 1260 Infinity instrument equipped with a 1260 DAD VL + detector.

The analysis was conducted in isocratic conditions by using acetonitrile H_2O = 50:50 (THX6) as a mobile phase at a constant flow rate of 1 mL/min (injection volume: 50 µL). The stationary phase was constituted by a Zorbax Eclipse Plus C18 column, 250 × 4.6 mm Agilent® (Santa Clara, CA, USA). UV detection was made at λ = 230 nm.

ROS production in SU-DIPG-36 cells. Flow cytometry analysis was performed to determine the intracellular production of ROS as reported[183]. Briefly, SU-DIPG-36 cells were seeded at a density of 500.000 cells per dish; after 24 hours, cells were treated with the investigated compounds at the selected concentrations. After the above mentioned timepoints SU-DIPG-36 cells were washed with warm DPBS and subsequently incubated with DCFH-DA 1mM for 60 minutes at 37 °C and 5% CO_2, protected from light. The cells were then washed with warm buffer, detached and centrifuged as described above, before being resuspended for assay run in the flow cytometer.

Immunoblotting analyses. Whole-cell extracts were obtained by solubilization in lysis buffer [50 mM Tris-HCl, pH 7.4; 150 mM NaCl; 1 mM EDTA; 1% Triton X-100; cOmplete™ Protease Inhibitor Cocktail (Roche)], followed by incubation at 4 °C for 30 min. Extracts were cleared by 15 min centrifugation at 12,000× g. Whole cell proteins (20-40 µg) were fractionated onto 12% Tris-Glycine-SDS minigels. Immunodetection was carried out by following primary antibodies: anti-ClpX (Abcam), anti-ClpP (Abcam), anti-total OXPHOS cocktail (Abcam), anti-TFAM (Cell Signaling Technology), anti-mS29 (Life Technology), anti-uL13 (ProteinTech), anti-VDAC1 (ProteinTech), and anti-β-actin (Sigma-Aldrich). Chemiluminescent detection was performed using Clarity Western ECL substrate (Bio-Rad), and signals were revealed by the ChemiDoc MP Imaging System (Bio-Rad).

Relative quantitation of mtDNA level. Mitochondrial DNA relative quantification was performed as described in Bruni et al.[184]. Melting curve analysis was performed to ensure the amplification specificity; the relative quantification was carried out according to the Pfaffl mathematical model[185].

Mitoribosomal subunits and ClpXP complex assembly analysis. Isokinetic sucrose gradient analyses were performed as described in Loguercio Polosa et al.[186]. Briefly, whole-cell extracts (1 mg) were loaded onto a 10-30% (v/v) sucrose gradient and subjected to centrifugation in an Optima L-100K ultracentrifuge (Beckman Coulter) using the SW 40Ti rotor at 100,000× g for 2 h and 15 min at 4 °C. For each experiment, eleven fractions were collected and analyzed by immunoblotting.

Establishment of PDT-O. Fresh biopsy samples used for PDT-O development were obtained from Hospices Civils de Lyon Biobank (CRB-HCL, BB-0033-00046) in the context of patient diagnosis, with all necessary regulatory approvals and informed consents for all patients. PDT-O models were established and cultured as previously described[162]. Briefly, minced tissues were digested at 37 °C with gentle vortex for 30-90 min. PDT-O were then established in 96-well plates using appropriate culture medium[19]. Medium was changed twice a week and PDT-O were split every 1 to 2 weeks when reaching a diameter of 800-1000 µm

Chemosensitivity profiling of PDT-O. For dose-response experiments, PDT-O were dissociated and seeded at 4000 cells/well in 96-well black ULA plates (Corning, cat. no. 4515). After 4 days, fully formed PDT-O were treated with serial dilutions of **26** (DA29) and ONC201 for 72 h. Cell viability was then measured using the CellTiter-Glo® 3D Cell Viability Assay (Promega, cat. no. G9683), in accordance with the manufacturer's instructions, and normalized with untreated (vehicle) negative control wells as 100% viability. Luminescence acquisitions were performed on a Spark® microplate reader (Tecan) with a 400-ms exposition and auto-attenuation. Data were obtained from two independent experiments performed in three technical replicates per condition. Dose-response curves were obtained using Prism 8.0.2 (GraphPad).

Radioligand binding experiments *h*D_2R and *h*D_3R. HEK293 cells stably expressing human D_{2L}R or D_3R were grown in a 50:50 mix of DMEM and Ham's F12 culture media, supplemented with 20 mM HEPES, 2 mM L-glutamine, 0.1 mM non-essential amino acids, 1X antibiotic/antimycotic, 10% heat-inactivated fetal bovine serum, and 200 µg/mL hygromycin (Life Technologies, Grand

Island, NY) and kept in an incubator at 37 °C and 5% CO_2. Upon reaching 80−90% confluence, cells were harvested using premixed Earle's balanced salt solution with 5 mM EDTA (Life Technologies) and centrifuged at 3,000 rpm for 10 min at 21°C. The supernatant was removed, and the pellet was resuspended in 10 mL hypotonic lysis buffer (5 mM $MgCl_2$, 5 mM Tris, pH 7.4 at 4 °C) and centrifuged at 18,000 rpm (~21,000g) for 20 min at 4 °C. The pellet was then resuspended in binding buffer. Bradford protein assay (Bio-Rad, Hercules, CA) was used to determine the protein concentration. Membranes were diluted to 500 μg/mL, in fresh EBSS binding buffer made from 8.7 g/L Earle's Balanced Salts without phenol red (US Biological, Salem, MA), 2.2 g/L sodium bicarbonate, pH to 7.4, and stored in a -80 °C freezer for later use. On the test day, each test compound was diluted into half-log serial dilutions using the 30% dimethyl sulfoxide (DMSO) vehicle. Membranes were diluted in fresh binding buffer (100-200 μg/mL) and radioligand competition experiments were conducted in 96-well plates containing 300 μL fresh binding buffer, 50 μL of the diluted test compound, 100 μL of membranes (10−20 μg/well total protein for both $hD_{2L}R$ and hD_3R), and 50 μL of radioligand diluted in binding buffer ([^{3}H]-*N*-methylspiperone: 0.4 nM final concentration for all the hD_2-like receptor subtypes; Novandi Chemistry AB, Södertälje, Sweden). Aliquots of radioligands solution were also quantified accurately in each experiment replicate, to determine how much radioactivity was added, taking in account the experimentally determined counter efficiency. Nonspecific binding was determined using 10 μM (+)-butaclamol (Sigma-Aldrich, St. Louis, MO), and total binding was determined with the 30% DMSO vehicle (3% final concentration). All compound dilutions were tested in triplicate, and the reaction incubated for 60 min at RT. The reaction was terminated by filtration through PerkinElmer Uni-Filter-96 GF/C, presoaked for the incubation time in 0.5% polyethylenimine (PEI), using a Revvity Unifilter-96 Cell Harvester (Revvity, Waltham, MA, USA). The filters were washed thrice with 3 mL (3 times ~1 mL/well) of ice-cold binding buffer. Revvity MicroScint-20 Scintillation Cocktail (65 μL) was added to each well, and filters were counted using a PerkinElmer MicroBeta Microplate Counter (Revvity, Waltham, MA, USA). IC_{50} values for each compound were determined from

dose−response curves, and K_i values were calculated using the Cheng−Prusoff equation. K_d values were determined via separate [^{3}H]-NMSP saturation binding experiments (K_d for D_2R = 0.320 ± 0.0618 nM; K_d for D_3R = 0.262 ± 0.0296 nM). When a complete inhibition could not be achieved at the highest tested concentrations, K_i values have been extrapolated by constraining the bottom of the dose−response curves (=0% residual specific binding) in the nonlinear regression analysis. These analyses were performed using GraphPad Prism 10.5 for Macintosh (GraphPad Software, San Diego, CA, USA). All results were rounded to the third significant figure. K_i values were determined from at least three independent experiments and are reported as the mean ± standard error of the mean (SEM). Compounds reported as "not active" displayed <50% inhibition, at the highest tested concentration of 10 mM, in a single experiment performed in triplicate.

Computational Studies. Computational studies were performed using FLAP (v2.2.2) in structure-based virtual screening mode. Molecular Interaction Fields (MIFs) were calculated with the GRID algorithm on the crystal structure of *h*ClpP in complex with **ZK53** (PDBID: 8HGK, 1.90 Å). Docking validation was conducted with AutoDock Vina (via UCSF Chimera) using grid boxes defined from the FLAP-identified pocket and visualized with PyMOL[187–189].

Lipidomic analyses. Total lipids of the cell lines untreated and treated with ONC201 and 26 (DA29) were extracted by using the protocol reported in our previous research studies[2]. The chloroform extract containing lipid substances was analyzed by using GC and HPLC analytical techniques for an exhaustive characterization expressed in terms of fatty acids and intact lipids. For GC analyses, lipid extracts were derivatized and analyzed by GC-MS and GC-FID as reported in Miciaccia et al.[2]. With respect to HPLC-MS/MS investigation, the lipid extract was reconstituted by using a volume of 500 µL of isopropanol and sonicated for 10 min. The analysis was performed on a Shimadzu Ultra High-Performance Liquid Chromatograph Nexera X-2 system (Shimadzu), including two LC-30 AD dual-plunger parallel-flow pumps, a DGU-20A5R degasser, a CTO-20AC column oven and a SIL-30AC auto-sampler. The UHPLC system was coupled to a LCMS-8060 triple quadrupole

mass spectrometer equipped with ESI interface (Shimadzu). Mobile phases were: (A) 20 mM ammonium formate and (B) 2-propanol/acetonitrile/20 mM ammonium formate (60:36:4 *v/v/v*) with 0.1% formic acid. The gradient program was: 0-6 min, 80-100% B (held for 16 min). The flow rate was 0.4 mL min^{-1}; the column used was an Ascentis Express C18, 100 × 2.1 mm, 2.7 µm dp (Merck Life Science, Darmstadt, Germany), the oven was set at 40 °C and the injection volume was 5 µL. MS and MS/MS acquisitions were performed using ESI source in positive (+) ionization mode, with the following parameters: interface temperature, 450 °C; CDL temperature, 250 °C; heat block temperature, 200 °C; nebulizing gas flow (N_2), 3 L min^{-1}; drying gas flow (N_2), 5 L min^{-1}; acquisition range, 350-1250 *m/z*.

Additional MS/MS experiments were optimized through the injection of single PL standards, as previously reported[190]. Data acquisition and processing was handled by the LabSolution ver. 5.95 software (Shimadzu Europa, Duisburg, Germany). The LIPID MAPS Structure Database (LMSD) was employed for compound identification (available at https://www.lipidmaps.org/data/structure/) by searching the following ion type: $[M+H]^+$ and $[M+Na]^+$ for LPC/PC/SM, and $[M+NH4]^+$ for TG. Data scedasticity was evaluated by using a two tailed F test (P values < 0.05 were considered as heteroscedastic). Statistically significant differences were evaluated by using a two tailed t test (P values < 0.05 were considered statistically significant). Statistical analysis was performed by using Excel 365 (Microsoft).

References

1. Perrone, M. G. *et al.* Diffuse Intrinsic Pontine Glioma (DIPG): Breakthrough and Clinical Perspective. *Curr. Med. Chem.* **28**, 3287–3317 (2021).
2. Miciaccia, M. *et al.* ONC201-Derived Tetrahydropyridopyrimidindiones as Powerful ClpP Protease Activators to Tackle Diffuse Midline Glioma. *J. Med. Chem.* **68**, 5190–5210 (2025).
3. Hargrave, D., Bartels, U. & Bouffet, E. Diffuse brainstem glioma in children: critical review of clinical trials. *Lancet Oncol.* **7**, 241–248 (2006).
4. Duffner, P. K., Cohen, M. E. & Freeman, A. I. Pediatric brain tumors: An overview. *CA. Cancer J. Clin.* **35**, 287–301 (1985).
5. Mandorino, M. *et al.* Pediatric Diffuse Midline Glioma H3K27-Altered: From Developmental Origins to Therapeutic Challenges. *Cancers* **16**, (2024).
6. Damodharan, S., Lara-Velazquez, M., Williamsen, B. C., Helgager, J. & Dey, M. Diffuse Intrinsic Pontine Glioma: Molecular Landscape, Evolving Treatment Strategies and Emerging Clinical Trials. *J. Pers. Med.* **12**, (2022).
7. Sison, J. *et al.* Palliative Care Options for a Young Adult Patient with a Diffuse Intrinsic Pontine Glioma. *Cureus* https://doi.org/10.7759/cureus.1580 (2017) doi:10.7759/cureus.1580.
8. Albright, A. L., Guthkelch, A. N., Packer, R. J., Price, R. A. & Rourke, L. B. Prognostic factors in pediatric brain-stem gliomas. *J. Neurosurg.* **65**, 751–755 (1986).
9. Fisher, P. G. *et al.* A clinicopathologic reappraisal of brain stem tumor classification: Identification of pilocytic astrocytoma and fibrillary astrocytoma as distinct entities. *Cancer* **89**, 1569–1576 (2000).
10. El-Khouly, F. E. *et al.* Diagnostics and treatment of diffuse intrinsic pontine glioma: where do we stand? *J. Neurooncol.* **145**, 177–184 (2019).
11. Monje, M. & Fisher, P. G. Neurological complications following treatment of children with brain tumors. *J. Pediatr. Rehabil. Med.* **4**, 31–36 (2011).

12. Donaldson, S. S., Laningham, F. & Fisher, P. G. Advances Toward an Understanding of Brainstem Gliomas. *J. Clin. Oncol.* **24**, 1266–1272 (2006).

13. Yoshimura, J., Onda, K., Tanaka, R. & Takahashi, H. Clinicopathological Study of Diffuse Type Brainstem Gliomas: Analysis of 40 Autopsy Cases. *Neurol. Med. Chir. (Tokyo)* **43**, 375–382 (2003).

14. Vanan, M. I. & Eisenstat, D. D. DIPG in Children – What Can We Learn from the Past? *Front. Oncol.* **5**, (2015).

15. Maitra, A. *et al.* Decoding Gene Expression Changes in Cerebral Tumors: Before and After Radiotherapy. *Med. Res. Rev.* **45**, 1651–1661 (2025).

16. Taylor, K. R. *et al.* Recurrent activating ACVR1 mutations in diffuse intrinsic pontine glioma. *Nat. Genet.* **46**, 457–461 (2014).

17. Buczkowicz, P. *et al.* Genomic analysis of diffuse intrinsic pontine gliomas identifies three molecular subgroups and recurrent activating ACVR1 mutations. *Nat. Genet.* **46**, 451–456 (2014).

18. Fontebasso, A. M. *et al.* Recurrent somatic mutations in ACVR1 in pediatric midline high-grade astrocytoma. *Nat. Genet.* **46**, 462–466 (2014).

19. the St. Jude Children's Research Hospital–Washington University Pediatric Cancer Genome Project. The genomic landscape of diffuse intrinsic pontine glioma and pediatric non-brainstem high-grade glioma. *Nat. Genet.* **46**, 444–450 (2014).

20. Mackay, A. *et al.* Integrated Molecular Meta-Analysis of 1,000 Pediatric High-Grade and Diffuse Intrinsic Pontine Glioma. *Cancer Cell* **32**, 520-537.e5 (2017).

21. Ren, M. & Van Nocker, S. In silico analysis of histone H3 gene expression during human brain development. *Int. J. Dev. Biol.* **60**, 167–173 (2016).

22. Castel, D. *et al.* Histone H3F3A and HIST1H3B K27M mutations define two subgroups of diffuse intrinsic pontine gliomas with different prognosis and phenotypes. *Acta Neuropathol. (Berl.)* **130**, 815–827 (2015).

23. Castel, D. *et al.* Transcriptomic and epigenetic profiling of 'diffuse midline gliomas, H3 K27M-mutant' discriminate two subgroups based on the type of histone H3 mutated and not supratentorial or infratentorial location. *Acta Neuropathol. Commun.* **6**, 117 (2018).

24. Nagaraja, S. *et al.* Histone Variant and Cell Context Determine H3K27M Reprogramming of the Enhancer Landscape and Oncogenic State. *Mol. Cell* **76**, 965-980.e12 (2019).

25. Rojo De La Vega, M., Chapman, E. & Zhang, D. D. NRF2 and the Hallmarks of Cancer. *Cancer Cell* **34**, 21–43 (2018).

26. Sedykh, I. *et al.* Zebrafish Rfx4 controls dorsal and ventral midline formation in the neural tube. *Dev. Dyn.* **247**, 650–659 (2018).

27. Piunti, A. *et al.* Therapeutic targeting of polycomb and BET bromodomain proteins in diffuse intrinsic pontine gliomas. *Nat. Med.* **23**, 493–500 (2017).

28. Justin, N. *et al.* Structural basis of oncogenic histone H3K27M inhibition of human polycomb repressive complex 2. *Nat. Commun.* **7**, 11316 (2016).

29. Diehl, K. L. *et al.* PRC2 engages a bivalent H3K27M-H3K27me3 dinucleosome inhibitor. *Proc. Natl. Acad. Sci.* **116**, 22152–22157 (2019).

30. Stafford, J. M. *et al.* Multiple modes of PRC2 inhibition elicit global chromatin alterations in H3K27M pediatric glioma. *Sci. Adv.* **4**, eaau5935 (2018).

31. Harutyunyan, A. S. *et al.* H3K27M induces defective chromatin spread of PRC2-mediated repressive H3K27me2/me3 and is essential for glioma tumorigenesis. *Nat. Commun.* **10**, 1262 (2019).

32. Venneti, S. *et al.* Evaluation of H istone 3 Lysine 27 Trimethylation (H3K27ME3) and Enhancer of Zest 2 (EZH 2) in Pediatric Glial and Glioneuronal Tumors Shows Decreased H3K27ME3 in *H3F3A* K27M Mutant Glioblastomas. *Brain Pathol.* **23**, 558–564 (2013).

33. Funato, K., Major, T., Lewis, P. W., Allis, C. D. & Tabar, V. Use of human embryonic stem cells to model pediatric gliomas with H3.3K27M histone mutation. *Science* **346**, 1529–1533 (2014).

34. Jain, S. U. *et al.* PFA ependymoma-associated protein EZHIP inhibits PRC2 activity through a H3 K27M-like mechanism. *Nat. Commun.* **10**, 2146 (2019).

35. Viebahn, C. Epithelio-Mesenchymal Transformation during Formation of the Mesoderm in the Mammalian Embryo. *Cells Tissues Organs* **154**, 79–97 (1995).

36. Duband, J.-L. Diversity in the molecular and cellular strategies of epithelium-to-mesenchyme transitions: Insights from the neural crest. *Cell Adhes. Migr.* **4**, 458–482 (2010).

37. Zou, S., Zhang, D., Xu, Z., Wen, X. & Zhang, Y. JMJD3 promotes the epithelial-mesenchymal transition and migration of glioma cells via the CXCL12/CXCR4 axis. *Oncol. Lett.* https://doi.org/10.3892/ol.2019.10972 (2019) doi:10.3892/ol.2019.10972.

38. Sanders, L. M. *et al.* Identification of a differentiation stall in epithelial mesenchymal transition in histone H3–mutant diffuse midline glioma. *GigaScience* **9**, giaa136 (2020).

39. Lulla, R. R., Saratsis, A. M. & Hashizume, R. Mutations in chromatin machinery and pediatric high-grade glioma. *Sci. Adv.* **2**, e1501354 (2016).

40. Calver, A. R. *et al.* Oligodendrocyte Population Dynamics and the Role of PDGF In Vivo. *Neuron* **20**, 869–882 (1998).

41. Iliakis, G. *et al.* Mechanisms of DNA double strand break repair and chromosome aberration formation. *Cytogenet. Genome Res.* **104**, 14–20 (2004).

42. Snyder, A. R. & Morgan, W. F. Gene expression profiling after irradiation: Clues to understanding acute and persistent responses? *Cancer Metastasis Rev.* **23**, 259–268 (2004).

43. Vulcani-Freitas, T. M. *et al.* ASPM gene expression in medulloblastoma. *Childs Nerv. Syst.* **27**, 71–74 (2011).

44. Northcott, P. A. *et al.* Medulloblastoma Comprises Four Distinct Molecular Variants. *J. Clin. Oncol.* **29**, 1408–1414 (2011).

45. Joki, T. *et al.* Assessment of Alterations in Gene Expression in Recurrent Malignant Glioma after Radiotherapy Using Complementary Deoxyribonucleic Acid Microarrays. *Neurosurgery* **48**, 195–202 (2001).

46. Li, S. *et al.* Identification of a gene signature associated with radiotherapy and prognosis in gliomas. *Oncotarget* **8**, 88974–88987 (2017).

47. Zhao, X., Li, C., Liu, L., Zou, H. & Li, K. Identification of Aberrantly Expressed Genes in Murine Glioblastoma During Radiotherapy via Bioinformatic Data Mining. *OncoTargets Ther.* **Volume 13**, 3839–3851 (2020).

48. Raviraj, R., Nagaraja, S. S., Selvakumar, I., Mohan, S. & Nagarajan, D. The epigenetics of brain tumors and its modulation during radiation: A review. *Life Sci.* **256**, 117974 (2020).

49. Matsko, M. V. *et al.* MORPHOLOGIC AND MOLECULAR FEATURES OF PRIMARY GLIOBLASTOMA IN PATIENTS SURVIVING MORE THAN 3 YEARS. *Sib. J. Oncol.* **18**, 34–44 (2019).

50. Wick, W. *et al.* Temozolomide chemotherapy alone versus radiotherapy alone for malignant astrocytoma in the elderly: the NOA-08 randomised, phase 3 trial. *Lancet Oncol.* **13**, 707–715 (2012).

51. Malmström, A. *et al.* Temozolomide versus standard 6-week radiotherapy versus hypofractionated radiotherapy in patients older than 60 years with glioblastoma: the Nordic randomised, phase 3 trial. *Lancet Oncol.* **13**, 916–926 (2012).

52. Hansen, R. J., Ludeman, S. M., Paikoff, S. J., Pegg, A. E. & Dolan, M. E. Role of MGMT in protecting against cyclophosphamide-induced toxicity in cells and animals. *DNA Repair* **6**, 1145–1154 (2007).

53. Gilbertson, R. J. *et al.* ERBB1 is amplified and overexpressed in high-grade diffusely infiltrative pediatric brain stem glioma. *Clin. Cancer Res. Off. J. Am. Assoc. Cancer Res.* **9**, 3620–3624 (2003).

54. Li, G. *et al.* Expression of epidermal growth factor variant III (EGFRvIII) in pediatric diffuse intrinsic pontine gliomas. *J. Neurooncol.* **108**, 395–402 (2012).

55. Adorno, J. O. *et al.* DIPG-51. ACVR1 MUTATIONS PROMOTE TUMOR GROWTH IN MODELS OF DIFFUSE INTRINSIC PONTINE GLIOMA. *Neuro-Oncol.* **22**, iii296–iii297 (2020).

56. Carvalho, D. M. *et al.* Repurposing Vandetanib plus Everolimus for the Treatment of *ACVR1* -Mutant Diffuse Intrinsic Pontine Glioma. *Cancer Discov.* **12**, 416–431 (2022).

57. Massimino, M. *et al.* Correction to: Results of nimotuzumab and vinorelbine, radiation and re-irradiation for diffuse pontine glioma in childhood. *J. Neurooncol.* **138**, 679–680 (2018).

58. Del Baldo, G. *et al.* Targeted therapy for pediatric diffuse intrinsic pontine glioma: a single-center experience. *Ther. Adv. Med. Oncol.* **14**, 17588359221113693 (2022).

59. Zhao, G. *et al.* Reversal of cancer gene expression identifies repurposed drugs for diffuse intrinsic pontine glioma. *Acta Neuropathol. Commun.* **10**, 150 (2022).

60. Nazha, B., Inal, C. & Owonikoko, T. K. Disialoganglioside GD2 Expression in Solid Tumors and Role as a Target for Cancer Therapy. *Front. Oncol.* **10**, 1000 (2020).

61. Mount, C. W. *et al.* Potent antitumor efficacy of anti-GD2 CAR T cells in H3-K27M+ diffuse midline gliomas. *Nat. Med.* **24**, 572–579 (2018).

62. Majzner, R. G. *et al.* GD2-CAR T cell therapy for H3K27M-mutated diffuse midline gliomas. *Nature* **603**, 934–941 (2022).

63. Srikanthan, D. *et al.* Diffuse intrinsic pontine glioma: current insights and future directions. *Chin. Neurosurg. J.* **7**, 6 (2021).

64. Truffaux, N. *et al.* Preclinical evaluation of dasatinib alone and in combination with cabozantinib for the treatment of diffuse intrinsic pontine glioma. *Neuro-Oncol.* **17**, 953–964 (2015).

65. Geoerger, B. *et al.* Innovative Therapies for Children with Cancer pediatric phase I study of erlotinib in brainstem glioma and relapsing/refractory brain tumors. *Neuro-Oncol.* **13**, 109–118 (2011).

66. Massimino, M., Bode, U., Biassoni, V. & Fleischhack, G. Nimotuzumab for pediatric diffuse intrinsic pontine gliomas. *Expert Opin. Biol. Ther.* **11**, 247–256 (2011).

67. for the Children's Oncology Group *et al.* IDH1 mutations are common in malignant gliomas arising in adolescents: a report from the Children's Oncology Group. *Childs Nerv. Syst.* **27**, 87–94 (2011).

68. Hashizume, R. *et al.* Pharmacologic inhibition of histone demethylation as a therapy for pediatric brainstem glioma. *Nat. Med.* **20**, 1394–1396 (2014).

69. Bagcchi, S. Panobinostat active against diffuse intrinsic pontine glioma. *Lancet Oncol.* **16**, e267 (2015).

70. Mohammad, F. *et al.* EZH2 is a potential therapeutic target for H3K27M-mutant pediatric gliomas. *Nat. Med.* **23**, 483–492 (2017).

71. Pardridge, W. M. Blood–brain barrier delivery. *Drug Discov. Today* **12**, 54–61 (2007).

72. Chen, Y. & Liu, L. Modern methods for delivery of drugs across the blood–brain barrier. *Adv. Drug Deliv. Rev.* **64**, 640–665 (2012).

73. Malakoutikhah, M., Teixidó, M. & Giralt, E. Shuttle-Mediated Drug Delivery to the Brain. *Angew. Chem. Int. Ed.* **50**, 7998–8014 (2011).

74. Daneman, R. & Prat, A. The Blood–Brain Barrier. *Cold Spring Harb. Perspect. Biol.* **7**, a020412 (2015).

75. Abbott, N. J., Patabendige, A. A. K., Dolman, D. E. M., Yusof, S. R. & Begley, D. J. Structure and function of the blood–brain barrier. *Neurobiol. Dis.* **37**, 13–25 (2010).

76. Peyrl, A. *et al.* Safety of Ommaya reservoirs in children with brain tumors: a 20-year experience with 5472 intraventricular drug administrations in 98 patients. *J. Neurooncol.* **120**, 139–145 (2014).

77. Cohen-Pfeffer, J. L. *et al.* Intracerebroventricular Delivery as a Safe, Long-Term Route of Drug Administration. *Pediatr. Neurol.* **67**, 23–35 (2017).

78. Mead, P. A., Safdieh, J. E., Nizza, P., Tuma, S. & Sepkowitz, K. A. Ommaya reservoir infections: A 16-year retrospective analysis. *J. Infect.* **68**, 225–230 (2014).

79. Szychot, E. *et al.* Clinical experience of convection-enhanced delivery (CED) of carboplatin and sodium valproate into the pons for the treatment of diffuse intrinsic pontine glioma (DIPG) in children and young adults after radiotherapy. *Int. J. Clin. Oncol.* **26**, 647–658 (2021).

80. E. Konofagou, E. *et al.* Ultrasound-Induced Blood-Brain Barrier Opening. *Curr. Pharm. Biotechnol.* **13**, 1332–1345 (2012).

81. Lynn, J. G., Zwemer, R. L., Chick, A. J. & Miller, A. E. A NEW METHOD FOR THE GENERATION AND USE OF FOCUSED ULTRASOUND IN EXPERIMENTAL BIOLOGY. *J. Gen. Physiol.* **26**, 179–193 (1942).

82. Baek, H., Pahk, K. J. & Kim, H. A review of low-intensity focused ultrasound for neuromodulation. *Biomed. Eng. Lett.* **7**, 135–142 (2017).

83. Stride, E. *et al.* Microbubble Agents: New Directions. *Ultrasound Med. Biol.* **46**, 1326–1343 (2020).

84. Song, K.-H., Harvey, B. K. & Borden, M. A. State-of-the-art of microbubble-assisted blood-brain barrier disruption. *Theranostics* **8**, 4393–4408 (2018).

85. Helfield, B. L., Chen, X., Qin, B., Watkins, S. C. & Villanueva, F. S. Mechanistic Insight into Sonoporation with Ultrasound-Stimulated Polymer Microbubbles. *Ultrasound Med. Biol.* **43**, 2678–2689 (2017).

86. Lentacker, I., De Cock, I., Deckers, R., De Smedt, S. C. & Moonen, C. T. W. Understanding ultrasound induced sonoporation: Definitions and underlying mechanisms. *Adv. Drug Deliv. Rev.* **72**, 49–64 (2014).

87. Hynynen, K., McDannold, N., Vykhodtseva, N. & Jolesz, F. A. Noninvasive MR Imaging–guided Focal Opening of the Blood-Brain Barrier in Rabbits. *Radiology* **220**, 640–646 (2001).

88. Filieri, S. *et al.* Can Focused Ultrasound Overcome the Failure of Chemotherapy in Treating Pediatric Diffuse Intrinsic Pontine Glioma Due to a Blood–Brain Barrier Obstacle? *Pharmaceuticals* **18**, 525 (2025).

89. Kline-Schoder, A. R. *et al.* Characterization of the responses of brain macrophages to focused ultrasound-mediated blood–brain barrier opening. *Nat. Biomed. Eng.* **8**, 650–663 (2023).

90. Martinez, P. *et al.* MRI-guided focused ultrasound blood–brain barrier opening increases drug delivery and efficacy in a diffuse midline glioma mouse model. *Neuro-Oncol. Adv.* **5**, vdad111 (2023).

91. Antonacci, M. *et al.* KATP Channel Inhibitors Reduce Cell Proliferation Through Upregulation of H3K27ac in Diffuse Intrinsic Pontine Glioma: A Functional Expression Investigation. *Cancers* **17**, 358 (2025).

92. Alli, S. *et al.* Brainstem blood brain barrier disruption using focused ultrasound: A demonstration of feasibility and enhanced doxorubicin delivery. *J. Controlled Release* **281**, 29–41 (2018).

93. ’T Hart, E. *et al.* Radiosensitisation by olaparib through focused ultrasound delivery in a diffuse midline glioma model. *J. Controlled Release* **357**, 287–298 (2023).

94. Woldegerima, A. *et al.* DIPG-73. FOCUSED ULTRASOUND FOR TREATMENT OF CHILDREN DIAGNOSED WITH DIFFUSE MIDLINE GLIOMAS. *Neuro-Oncol.* **26**, 0–0 (2024).

95. Madhukar, N. S. *et al.* A Bayesian machine learning approach for drug target identification using diverse data types. *Nat. Commun.* **10**, 5221 (2019).

96. Allen, J. E. *et al.* Dual Inactivation of Akt and ERK by TIC10 Signals Foxo3a Nuclear Translocation, TRAIL Gene Induction, and Potent Antitumor Effects. *Sci. Transl. Med.* **5**, (2013).

97. Refaat, A., Abd-Rabou, A. & Reda, A. TRAIL combinations: The new 'trail' for cancer therapy (Review). *Oncol. Lett.* **7**, 1327–1332 (2014).

98. Dai, X. *et al.* Targeting TNF-related apoptosis-inducing ligand (TRAIL) receptor by natural products as a potential therapeutic approach for cancer therapy. *Exp. Biol. Med.* **240**, 760–773 (2015).

99. Allen, J. E. *et al.* Discovery and clinical introduction of first-in-class imipridone ONC201. *Oncotarget* **7**, 74380–74392 (2016).

100. Kline, C. L. B. *et al.* ONC201 kills solid tumor cells by triggering an integrated stress response dependent on ATF4 activation by specific eIF2α kinases. *Sci. Signal.* **9**, (2016).

101. Greer, Y. E. *et al.* ONC201 kills breast cancer cells *in vitro* by targeting mitochondria. *Oncotarget* **9**, 18454–18479 (2018).

102. Ralff, M. D. *et al.* ONC201 Demonstrates Antitumor Effects in Both Triple-Negative and Non–Triple-Negative Breast Cancers through TRAIL-Dependent and TRAIL-Independent Mechanisms. *Mol. Cancer Ther.* **16**, 1290–1298 (2017).

103. Ishizawa, J. *et al.* ATF4 induction through an atypical integrated stress response to ONC201 triggers p53-independent apoptosis in hematological malignancies. *Sci. Signal.* **9**, (2016).

104. Yuan, X. *et al.* ONC201 activates ER stress to inhibit the growth of triple-negative breast cancer cells. *Oncotarget* **8**, 21626–21638 (2017).

105. Cao, Z. *et al.* AKT and ERK dual inhibitors: The way forward? *Cancer Lett.* **459**, 30–40 (2019).

106. Nho, R. S. FoxO3a and disease progression. *World J. Biol. Chem.* **5**, 346 (2014).

107. Wang, X., Hu, S. & Liu, L. Phosphorylation and acetylation modifications of FOXO3a: Independently or synergistically? *Oncol. Lett.* **13**, 2867–2872 (2017).

108. Yang, W., Dolloff, N. G. & El-Deiry, W. S. ERK and MDM2 prey on FOXO3a. *Nat. Cell Biol.* **10**, 125–126 (2008).

109. Beretta, G. L., Corno, C., Zaffaroni, N. & Perego, P. Role of FoxO Proteins in Cellular Response to Antitumor Agents. *Cancers* **11**, 90 (2019).

110. Eisenhofer, G. *et al.* Biochemical Diagnosis of Pheochromocytoma: How to Distinguish True- from False-Positive Test Results. *J. Clin. Endocrinol. Metab.* **88**, 2656–2666 (2003).

111. Versteeg, D. H. G., Van Der Gugten, J., De Jong, W. & Palkovits, M. Regional concentrations of noradrenaline and dopamine in rat brain. *Brain Res.* **113**, 563–574 (1976).

112. Missale, C., Nash, S. R., Robinson, S. W., Jaber, M. & Caron, M. G. Dopamine Receptors: From Structure to Function. *Physiol. Rev.* **78**, 189–225 (1998).

113. Kline, C. L. B. *et al.* Role of Dopamine Receptors in the Anticancer Activity of ONC201. *Neoplasia* **20**, 80–91 (2018).

114. Prabhu, V. V. *et al.* ONC201 and imipridones: Anti-cancer compounds with clinical efficacy. *Neoplasia* **22**, 725–744 (2020).

115. Madhukar, N. S. *et al.* A New Big-Data Paradigm for Target Identification and Drug Discovery. Preprint at https://doi.org/10.1101/134973 (2017).

116. Cheng, H.-W. *et al.* Identification of thioridazine, an antipsychotic drug, as an antiglioblastoma and anticancer stem cell agent using public gene expression data. *Cell Death Dis.* **6**, e1753–e1753 (2015).

117. Ishizawa, J. *et al.* Mitochondrial ClpP-Mediated Proteolysis Induces Selective Cancer Cell Lethality. *Cancer Cell* **35**, 721-737.e9 (2019).

118. Wang, S. & Dougan, D. A. The Direct Molecular Target for Imipridone ONC201 Is Finally Established. *Cancer Cell* **35**, 707–708 (2019).

119. Graves, P. R. *et al.* Mitochondrial Protease ClpP is a Target for the Anticancer Compounds ONC201 and Related Analogues. *ACS Chem. Biol.* **14**, 1020–1029 (2019).

120. Wang, P. *et al.* Aberrant human ClpP activation disturbs mitochondrial proteome homeostasis to suppress pancreatic ductal adenocarcinoma. *Cell Chem. Biol.* **29**, 1396-1408.e8 (2022).

121. Choi, S.-E. *et al.* Mitochondrial protease ClpP supplementation ameliorates diet-induced NASH in mice. *J. Hepatol.* **77**, 735–747 (2022).

122. Cao, J. *et al.* ONC206 targeting ClpP induces mitochondrial dysfunction and protective autophagy in hepatocellular carcinoma cells. *Neoplasia* **55**, 101015 (2024).

123. Chattopadhyay, C. *et al.* Imipridones inhibit tumor growth and improve survival in an orthotopic liver metastasis mouse model of human uveal melanoma. Preprint at https://doi.org/10.1101/2024.01.12.575058 (2024).

124. Nishigaki, R. *et al.* Proteomic identification of differentially-expressed genes in human gastric carcinomas. *PROTEOMICS* **5**, 3205–3213 (2005).

125. Parker, C. S. *et al.* ONC201/TIC10 plus TLY012 anti-cancer effects via apoptosis inhibitor downregulation, stimulation of integrated stress response and death receptor DR5 in gastric adenocarcinoma. *Am. J. Cancer Res.* **13**, 6290–6312 (2023).

126. Schirizzi, A. *et al.* The multiple combination of Paclitaxel, Ramucirumab and Elacridar reverses the paclitaxel-mediated resistance in gastric cancer cell lines. *Front. Oncol.* **13**, 1129832 (2023).

127. Zhang, J. *et al.* IMP075 targeting ClpP for colon cancer therapy in vivo and in vitro. *Biochem. Pharmacol.* **204**, 115232 (2022).

128. Zhang, J. *et al.* Discovery of a Novel Series of *Homo sapiens* Caseinolytic Protease P Agonists for Colorectal Adenocarcinoma Treatment via ATF3-Dependent Integrated Stress Response. *J. Med. Chem.* **67**, 2812–2836 (2024).

129. Zhou, L.-L. *et al.* Selective activator of human ClpP triggers cell cycle arrest to inhibit lung squamous cell carcinoma. *Nat. Commun.* **14**, 7069 (2023).

130. Wang, J., Hartling, J. A. & Flanagan, J. M. The Structure of ClpP at 2.3 Å Resolution Suggests a Model for ATP-Dependent Proteolysis. *Cell* **91**, 447–456 (1997).

131. Lee, B.-G. *et al.* Structures of ClpP in complex with acyldepsipeptide antibiotics reveal its activation mechanism. *Nat. Struct. Mol. Biol.* **17**, 471–478 (2010).

132. Vedadi, M. *et al.* Genome-scale protein expression and structural biology of Plasmodium falciparum and related Apicomplexan organisms. *Mol. Biochem. Parasitol.* **151**, 100–110 (2007).

133. Gersch, M., List, A., Groll, M. & Sieber, S. A. Insights into Structural Network Responsible for Oligomerization and Activity of Bacterial Virulence Regulator Caseinolytic Protease P (ClpP) Protein. *J. Biol. Chem.* **287**, 9484–9494 (2012).

134. Joshi, S. A., Hersch, G. L., Baker, T. A. & Sauer, R. T. Communication between ClpX and ClpP during substrate processing and degradation. *Nat. Struct. Mol. Biol.* **11**, 404–411 (2004).

135. Gribun, A. *et al.* The ClpP Double Ring Tetradecameric Protease Exhibits Plastic Ring-Ring Interactions, and the N Termini of Its Subunits Form Flexible Loops That Are Essential for ClpXP and ClpAP Complex Formation. *J. Biol. Chem.* **280**, 16185–16196 (2005).

136. Zeiler, E. *et al.* Structural and functional insights into caseinolytic proteases reveal an unprecedented regulation principle of their catalytic triad. *Proc. Natl. Acad. Sci.* **110**, 11302–11307 (2013).

137. Goncalves, M. M. *et al.* Mechanism of allosteric activation in human mitochondrial ClpP protease. *Proc. Natl. Acad. Sci.* **122**, e2419881122 (2025).

138. Li, D. H. S. *et al.* Acyldepsipeptide Antibiotics Induce the Formation of a Structured Axial Channel in ClpP: A Model for the ClpX/ClpA-Bound State of ClpP. *Chem. Biol.* **17**, 959–969 (2010).

139. Bewley, M. C., Graziano, V., Griffin, K. & Flanagan, J. M. The asymmetry in the mature amino-terminus of ClpP facilitates a local symmetry match in ClpAP and ClpXP complexes. *J. Struct. Biol.* **153**, 113–128 (2006).

140. Szyk, A. & Maurizi, M. R. Crystal structure at 1.9Å of E. coli ClpP with a peptide covalently bound at the active site. *J. Struct. Biol.* **156**, 165–174 (2006).

141. Kim, D. Y. & Kim, K. K. The Structural Basis for the Activation and Peptide Recognition of Bacterial ClpP. *J. Mol. Biol.* **379**, 760–771 (2008).

142. Lee, B.-G., Kim, M. K. & Song, H. K. Structural insights into the conformational diversity of ClpP from Bacillus subtilis. *Mol. Cells* **32**, 589–595 (2011).

143. Kang, S. G., Maurizi, M. R., Thompson, M., Mueser, T. & Ahvazi, B. Crystallography and mutagenesis point to an essential role for the N-terminus of human mitochondrial ClpP. *J. Struct. Biol.* **148**, 338–352 (2004).

144. Zhang, J. *et al.* Structural Switching of Staphylococcus aureus Clp Protease. *J. Biol. Chem.* **286**, 37590–37601 (2011).

145. Geiger, S. R., Böttcher, T., Sieber, S. A. & Cramer, P. A Conformational Switch Underlies ClpP Protease Function. *Angew. Chem. Int. Ed.* **50**, 5749–5752 (2011).

146. Sprangers, R., Gribun, A., Hwang, P. M., Houry, W. A. & Kay, L. E. Quantitative NMR spectroscopy of supramolecular complexes: Dynamic side pores in ClpP are important for product release. *Proc. Natl. Acad. Sci.* **102**, 16678–16683 (2005).

147. Kimber, M. S. *et al.* Structural and Theoretical Studies Indicate that the Cylindrical Protease ClpP Samples Extended and Compact Conformations. *Structure* **18**, 798–808 (2010).

148. Ingvarsson, H. *et al.* Insights into the inter-ring plasticity of caseinolytic proteases from the X-ray structure of *Mycobacterium tuberculosis* ClpP1. *Acta Crystallogr. D Biol. Crystallogr.* **63**, 249–259 (2007).

149. El Bakkouri, M. *et al.* The Clp Chaperones and Proteases of the Human Malaria Parasite Plasmodium falciparum. *J. Mol. Biol.* **404**, 456–477 (2010).

150. Ye, F. *et al.* Helix Unfolding/Refolding Characterizes the Functional Dynamics of Staphylococcus aureus Clp Protease. *J. Biol. Chem.* **288**, 17643–17653 (2013).

151. Kang, S. G., Dimitrova, M. N., Ortega, J., Ginsburg, A. & Maurizi, M. R. Human Mitochondrial ClpP Is a Stable Heptamer That Assembles into a Tetradecamer in the Presence of ClpX. *J. Biol. Chem.* **280**, 35424–35432 (2005).

152. Kang, S. G. *et al.* Functional Proteolytic Complexes of the Human Mitochondrial ATP-dependent Protease, hClpXP. *J. Biol. Chem.* **277**, 21095–21102 (2002).

153. Armenise, D. *et al.* Mitochondrial Protease ClpP: Cancer Marker and Drug Target. *Pharmaceuticals* **18**, 1443 (2025).

154. Mabanglo, M. F. *et al.* Potent ClpP agonists with anticancer properties bind with improved structural complementarity and alter the mitochondrial N-terminome. *Structure* **31**, 185-200.e10 (2023).

155. Huang, J. *et al.* Discovery of a Novel Series of Imipridone Compounds as *Homo sapiens* Caseinolytic Protease P Agonists with Potent Antitumor Activities In Vitro and In Vivo. *J. Med. Chem.* **65**, 7629–7655 (2022).

156. Xiang, X. *et al.* Rational Design of a Novel Class of Human ClpP Agonists through a Ring-Opening Strategy with Enhanced Antileukemia Activity. *J. Med. Chem.* **67**, 6769–6792 (2024).

157. Wong, K. S. *et al.* Acyldepsipeptide Analogs Dysregulate Human Mitochondrial ClpP Protease Activity and Cause Apoptotic Cell Death. *Cell Chem. Biol.* **25**, 1017-1030.e9 (2018).

158. Stahl, M. *et al.* Selective Activation of Human Caseinolytic Protease P (ClpP). *Angew. Chem. Int. Ed.* **57**, 14602–14607 (2018).

159. Zhang, R. *et al.* Assessment of the structure-activity relationship and antileukemic activity of diacylpyramide compounds as human ClpP agonists. *Eur. J. Med. Chem.* **258**, 115577 (2023).

160. Wei, B. *et al.* Anti-infective therapy using species-specific activators of Staphylococcus aureus ClpP. *Nat. Commun.* **13**, 6909 (2022).

161. Mabanglo, M. F. *et al.* ClpP protease activation results from the reorganization of the electrostatic interaction networks at the entrance pores. *Commun. Biol.* **2**, 410 (2019).

162. Deligne, C. *et al.* Establishing a living biobank of pediatric high-grade glioma and ependymoma suitable for cancer pharmacology. *Neuro-Oncol.* **27**, 1325–1340 (2025).

163. Daina, A., Michielin, O. & Zoete, V. SwissADME: a free web tool to evaluate pharmacokinetics, drug-likeness and medicinal chemistry friendliness of small molecules. *Sci. Rep.* **7**, 42717 (2017).

164. Costa, J. *et al.* Investigating Curcumin/Intestinal Epithelium Interaction in a Millifluidic Bioreactor. *Bioengineering* **7**, 100 (2020).

165. Colombo, R., Paolillo, M. & Papetti, A. A Dynamic In Vitro Model for Testing Intestinal Absorption of Different Vegetable Food Secondary Metabolites. *Appl. Sci.* **13**, 5033 (2023).

166. Giusti, S. *et al.* A novel dual-flow bioreactor simulates increased fluorescein permeability in epithelial tissue barriers. *Biotechnol. J.* **9**, 1175–1184 (2014).

167. Criddle, D. N. *et al.* Menadione-induced Reactive Oxygen Species Generation via Redox Cycling Promotes Apoptosis of Murine Pancreatic Acinar Cells. *J. Biol. Chem.* **281**, 40485–40492 (2006).

168. Ripstein, Z. A., Vahidi, S., Houry, W. A., Rubinstein, J. L. & Kay, L. E. A processive rotary mechanism couples substrate unfolding and proteolysis in the ClpXP degradation machinery. *eLife* **9**, e52158 (2020).

169. Ferrarini, I., Louie, A., Zhou, L. & El-Deiry, W. S. ONC212 is a Novel Mitocan Acting Synergistically with Glycolysis Inhibition in Pancreatic Cancer. *Mol. Cancer Ther.* **20**, 1572–1583 (2021).

170. Mabanglo, M. F., Bhandari, V. & Houry, W. A. Substrates and interactors of the ClpP protease in the mitochondria. *Curr. Opin. Chem. Biol.* **66**, 102078 (2022).

171. Koludarova, L. & Battersby, B. J. Mitochondrial protein synthesis quality control. *Hum. Mol. Genet.* **33**, R53–R60 (2024).

172. Richter, U. *et al.* Mitochondrial stress response triggered by defects in protein synthesis quality control. *Life Sci. Alliance* **2**, e201800219 (2019).

173. Fennell, E. M. J. *et al.* Multi-omics analyses reveal ClpP activators disrupt essential mitochondrial pathways in triple-negative breast cancer. *Front. Pharmacol.* **14**, 1136317 (2023).

174. Kalous, M., Rauchová, H. & Drahota, Z. The effect of lysophosphatidylcholine on the activity of various mitochondrial enzymes. *Biochim. Biophys. Acta BBA - Bioenerg.* **1098**, 167–171 (1992).

175. Tang, R. *et al.* Design, Synthesis, and Biological Evaluation of Novel Activators of Human Caseinolytic Protease P with a Pyrazololactam Scaffold. *J. Med. Chem.* **68**, 9984–10007 (2025).

176. Matsuda, E. *et al.* Inhibition of ELOVL6 activity impairs mitochondrial respiratory function and inhibits tumor progression in FGFR3-mutated bladder cancer cells. *Biochim. Biophys. Acta BBA - Mol. Basis Dis.* **1871**, 168023 (2025).

177. Cai, Z. R. *et al.* Phosphonate analogs of hiv integrase inhibitor compounds. (2008).

178. Vonrhein, C. *et al.* Data processing and analysis with the *autoPROC* toolbox. *Acta Crystallogr. D Biol. Crystallogr.* **67**, 293–302 (2011).

179. McCoy, A. J. *et al. Phaser* crystallographic software. *J. Appl. Crystallogr.* **40**, 658–674 (2007).

180. Adams, P. D. *et al. PHENIX* : a comprehensive Python-based system for macromolecular structure solution. *Acta Crystallogr. D Biol. Crystallogr.* **66**, 213–221 (2010).

181. Emsley, P., Lohkamp, B., Scott, W. G. & Cowtan, K. Features and development of *Coot*. *Acta Crystallogr. D Biol. Crystallogr.* **66**, 486–501 (2010).

182. Miciaccia, M. *et al.* Harmaline to Human Mitochondrial Caseinolytic Serine Protease Activation for Pediatric Diffuse Intrinsic Pontine Glioma Treatment. *Pharmaceuticals* **17**, 135 (2024).

183. Sandin-Mazzondo, L. *et al.* 4,5-Diazafluorene derivatives and their silver(I) complexes: Synthesis and biological evaluation as antiproliferative agents. *Eur. J. Med. Chem.* **292**, 117680 (2025).

184. Bruni, F., Proctor-Kent, Y., Lightowlers, R. N. & Chrzanowska-Lightowlers, Z. M. Messenger RNA delivery to mitoribosomes – hints from a bacterial toxin. *FEBS J.* **288**, 437–451 (2021).

185. Pfaffl, M. W. A new mathematical model for relative quantification in real-time RT-PCR. *Nucleic Acids Res.* **29**, 45e–445 (2001).

186. Loguercio Polosa, P., Capriglia, F. & Bruni, F. Molecular Investigation of Mitochondrial RNA19 Role in the Pathogenesis of MELAS Disease. *Life* **13**, 1863 (2023).

187. Carosati, E., Sciabola, S. & Cruciani, G. Hydrogen Bonding Interactions of Covalently Bonded Fluorine Atoms: From Crystallographic Data to a New Angular Function in the GRID Force Field. *J. Med. Chem.* **47**, 5114–5125 (2004).

188. Perrone, M. G. *et al.* An attempt to chemically state the cross-talk between monomers of COX homodimers by double/hybrid inhibitors mofezolac-spacer-mofezolac and mofezolac-spacer-arachidonic acid. *Eur. J. Med. Chem.* **209**, 112919 (2021).

189. Goodford, P. J. A computational procedure for determining energetically favorable binding sites on biologically important macromolecules. *J. Med. Chem.* **28**, 849–857 (1985).

190. Stincone, P. *et al.* Listeria monocytogenes exposed to antimicrobial peptides displays differential regulation of lipids and proteins associated to stress response. *Cell. Mol. Life Sci.* **79**, 263 (2022).

Centro Nazionale di Ricerca HPC, Big data e Quantum Computing contrassegnato dal codice identificativo CN000000013, CUP H93C22000450007

Un ringraziamento a Next Generation EU: iniziativa PNRR, Missione 4, Componente 2, Investimento 1.4 "Potenziamento strutture di ricerca e creazione di "campioni nazionali" di R&S su alcune Key enabling technologies" DD MUR N. 3138 del 16/12/2021 finanziato dall'Unione europea – Next Generation EU, tematica CN1 "Simulazioni, calcolo e analisi dei dati ad alte prestazioni" per il finanziamento.

APPENDIX

1. **Table S1.** Radioligand Binding Data for *h*D2R and *h*D3R.
2. **Table S2.** List of fatty acids detected in SH-SY5Y and SU-DIPG-36 cell lines untreated and treated with **ONC201** and **26** (DA29).
3. **Table S3.** List of lysophosphocholine (LPC), phoshocholine (PC), and sphingomyelin (SM) detected in SH-SY5Y and SU-DIPG-36 cell lines untreated and treated with **ONC201** and **26** (DA29).
4. **Table S4.** List of triglycerides (TGs) detected in SH-SY5Y and SU-DIPG-36 cell lines untreated and treated with **ONC201** and **26** (DA29).
5. **Table S5.** Choline-containing lipids identified in the SU-DIPG-36 and SH-SY5Y cell lines.
6. **Table S6.** Triacylglycerols (TG) identified in SU-DIP-G36 and SH-SY5Y cell lines.
7. **Figure S1**. FLAP analysis and Molecular docking with AutoDock Vina of **26** (DA29) and **ZK53** (PDB code: 8HGK)
8. **Figure S2**. Histograms relative to the percentage content of choline-containing lipids (LPCs, PCs and SMs).
9. **Figure S3**. Histograms relative to the percentage content of TGs.

1. **Supplementary Table S1**

Competition *vs* [^{3}H]-*N*-Methylspiperone		
Compound	***h*D$_2$R pKi ± SEM**	***h*D$_3$R pKi ± SEM**
9 (DA17)	<5	<5
11 (DA24)	<5	<5
12 (DA32)	<5	<5
14 (DA33)	<5	<5
15 (DA35)	<5	<5
16 (DA53)	<5	<5
26 (DA29)	<5	<5
27 (DA42)	<5	<5
31 (DA45)	<5	<5
33 (DA28)	<5	<5
34 (DA34)	<5	<5

Table S1. Radioligand Binding Data for *h*D2R and *h*D3R. Radioligand competition binding assays performed on HEK293 cells stably expressing *h*D$_2$R and *h*D$_3$R in the presence of [^{3}H]-*N*-Methylspiperone. Equilibrium dissociation constants (K_i) were derived from IC_{50} values using the Cheng−Prusoff equation. pKi = -$\log_{10}$(Ki). pKi <5 represents <50% inhibition at the highest tested concentration of 10 μM.

4. Supplementary Table S2

FAMEs	MS Sim %	LRI exp	LRI ref	SU-DIPG-36			SH-SY5Y		
				UNT	**ONC 201**	**26** (DA29)	UNT	**ONC 201**	**26** (DA29)
C14:0	94	1398	1400	1.40 ± 0.02	1.26 ± 0.03	1.87 ± 0.11	1.29 ± 0.01	2.10 ± 0.08	2.00 ± 0.06
C15:0	90	1500	1502	0.23 ± 0.00	0.28 ± 0.01	0.38 ± 0.04	0.21 ± 0.01	0.29 ± 0.02	0.33 ± 0.00
C16:0	95	1600	1600	28.69 ± 0.04	44.92 ± 0.34	28.37 ± 0.16	41.32 ± 0.12	41.62 ± 0.70	41.32 ± 0.10
C16:1ω9	89	1604	1603	0.72 ± 0.01	0.63 ± 0.04	1.29 ± 0.06	1.07 ± 0.07	2.39 ± 0.05	1.85 ± 0.16
C16:1ω7	90	1614	1609	3.36 ± 0.02	1.59 ± 0.03	3.19 ± 0.13	0.71 ± 0.02	1.08 ± 0.02	1.05 ± 0.02
C17:0	90	1694	1702	0.31 ± 0.03	0.22 ± 0.01	0.34 ± 0.12	0.14 ± 0.02	0.13 ± 0.02	0.16 ± 0.01
C17:1ω7	90	1707	1713	0.47 ± 0.02	0.49 ± 0.01	0.47 ± 0.12	*nd*	*nd*	*nd*
C18:0	95	1800	1800	18.01 ± 0.03	25.23 ± 0.09	15.97 ± 0.08	25.01 ± 0.08	24.85 ± 0.20	25.10 ± 0.15
C18:1ω9-(E)	92	1801	1800	*nd*	*nd*	*nd*	2.53 ± 0.13	1.99 ± 0.09	2.09 ± 0.09
C18:1ω9-(Z)	95	1807	1810	28.85 ± 0.18	15.83 ± 0.04	28.88 ± 0.19	12.78 ± 0.22	11.67 ± 0.16	11.32 ± 0.06
C18:1ω7	95	1815	1820	5.00 ± 0.03	3.88 ± 0.05	8.23 ± 0.05	3.21 ± 0.01	3.25 ± 0.17	3.23 ± 0.00
C18:1ω6	89	1826	1826	0.41 ± 0.01	*tr*	0.32 ± 0.01	0.37 ± 0.00	0.19 ± 0.01	0.21 ± 0.00
C18:2ω6	91	1840	1848	2.46 ± 0.05	0.65 ± 0.00	1.41 ± 0.00	0.26 ± 0.03	0.39 ± 0.00	0.40 ± 0.02
9,10-methylene C18:0	87	1906	1911	0.22 ± 0.00	0.06 ± 0.01	0.06 ± 0.01	nd	*nd*	*nd*
C20:0	86	2000	2000	0.43 ± 0.01	0.45 ± 0.05	0.33 ± 0.03	0.30 ± 0.01	0.25 ± 0.01	0.27 ± 0.02
C20:1ω11	86	2006	2004	*nd*	*nd*	*nd*	0.34 ± 0.00	0.23 ± 0.03	0.19 ± 0.01
C20:1ω9	89	2010	2008	*nd*	*nd*	*nd*	0.38 ± 0.00	0.65 ± 0.03	0.71 ± 0.02
C20:1ω7	94	2014	2015	1.55 ± 0.01	0.92 ± 0.03	1.98 ± 0.02	1.04 ± 0.01	0.53 ± 0.02	0.66 ± 0.01
C20:3ω9	85	2026	2028	0.62 ± 0.01	0.82 ± 0.04	1.17 ± 0.03	3.30 ± 0.03	3.50 ± 0.14	3.49 ± 0.02
C20:2ω9*	-	2035	-	*nd*	*nd*	*nd*	0.43 ± 0.02	0.49 ± 0.01	0.35 ± 0.01
C20:2ω7*	-	2051	-	*nd*	*nd*	*nd*	0.43 ± 0.02	0.53 ± 0.04	0.61 ± 0.03
C20:4ω6	91	2063	2065	2.84 ± 0.05	0.93 ± 0.01	2.10 ± 0.05	0.37 ± 0.01	0.63 ± 0.05	0.77 ± 0.04
C20:3ω6	91	2071	2069	0.49 ± 0.02	0.23 ± 0.00	0.51 ± 0.02	0.12 ± 0.01	0.17 ± 0.01	0.15 ± 0.01
C20:5ω3	90	2117	2122	0.24 ± 0.00	*tr*	0.22 ± 0.02	*nd*	*nd*	*nd*
C22:0	91	2199	2200	0.23 ± 0.00	0.31 ± 0.04	0.14 ± 0.04	0.23 ± 0.00	0.08 ± 0.01	0.06 ± 0.00
C22:1ω11	86	2203	2207	*nd*	*nd*	*nd*	0.10 ± 0.01	0.10 ± 0.02	0.08 ± 0.00
C22:1ω9	88	2215	2211	0.30 ± 0.01	0.22 ± 0.02	0.37 ± 0.05	0.29 ± 0.03	0.17 ± 0.02	0.16 ± 0.01
C22:3	-	2246	-	*nd*	*nd*	*nd*	2.70 ± 0.01	1.85 ± 0.11	2.37 ± 0.03
C22:5ω6	85	2273	2274	0.18 ± 0.00	*nd*	0.08 ± 0.01	0.10 ± 0.00	0.09 ± 0.04	0.12 ± 0.01
C22:4ω6	89	2282	2286	0.37 ± 0.00	0.13 ± 0.01	0.28 ± 0.01	0.14 ± 0.00	0.28 ± 0.04	0.32 ± 0.02
C22:6ω3	94	2325	2335	1.41 ± 0.08	0.50 ± 0.03	1.10 ± 0.02	*nd*	*nd*	*nd*
C22:5ω3	90	2339	2338	0.49 ± 0.04	0.14 ± 0.01	0.44 ± 0.01	0.15 ± 0.00	0.26 ± 0.02	0.31 ± 0.00
C24:0	90	2399	2400	0.46 ± 0.05	0.14 ± 0.01	0.22 ± 0.01	0.16 ± 0.00	0.12 ± 0.01	0.11 ± 0.01
C24:1ω9	88	2416	2414	0.26 ± 0.01	0.15 ± 0.01	0.29 ± 0.01	0.50 ± 0.03	0.12 ± 0.00	0.20 ± 0.01
TOT				100	100	100	100	100	100
SFA				49.99 ± 0.07	72.87 ± 0.27	47.69 ± 0.06	68.65 ± 0.16	69.44 ± 0.76	69.36 ± 0.07
MUFA				40.92 ± 0.16	23.73 ± 0.19	45.01 ± 0.10	23.33 ± 0.17	22.36 ± 0.46	21.76 ± 0.08
PUFA				9.10 ± 0.23	3.41 ± 0.08	7.30 ± 0.07	8.01 ± 0.04	8.19 ± 0.31	8.88 ± 0.04
ω-9				30.74 ± 0.20	17.65 ± 0.13	32.00 ± 0.20	21.28 ± 0.24	20.98 ± 0.36	20.17 ± 0.28
ω-6				6.75 ± 0.14	1.94 ± 0.02	4.68 ± 0.05	1.37 ± 0.01	1.75 ± 0.02	1.96 ± 0.03
ω-3				2.14 ± 0.12	0.64 ± 0.04	1.77 ± 0.02	0.15 ± 0.00	0.26 ± 0.02	0.31 ± 0.00

Note: *nd*, not detected; *tr*, trace level; compounds *, tentative identification.

Table S2. List of fatty acids detected in SH-SY5Y and SU-DIPG-36 cell lines untreated and treated with **ONC201** and **26** (DA29). Identification parameters: mass spectral similarity (MS sim.); experimental linear retention index (LRI exp.); reference linear retention index (LRI ref.). FAMEs amounts were expressed in area % (GC-FID area normalized) ± standard deviation. Fatty acids were also grouped in chemical class as follows: SFA: saturated fatty acid; MUFA: monounsaturated fatty acid; PUFA: polyunsaturated fatty acid; ω-9: omega-9; ω-6: omega-6; ω-3: omega-3. UN= Untreated.

5. Supplementary Table S3

RT (min)	*m/z*	Ion Type	Class	CN:DB	PN	SU-DIPG-36			SH-SY5Y		
						UNT	**ONC 201**	**26** (DA29)	UNT	**ONC 201**	**26** (DA29)
0,83	468,4	[M+H]+	LPC	14:0	14	0.25 ± 0.02	0.46 ± 0.03	*nd*	0.82 ± 0.05	0.33 ± 0.01	0.78 ± 0.04
0,83	494,4	[M+H]+	LPC	16:1	14	0.41 ± 0.02	0.39 ± 0.01	0.66 ± 0.03	1.43 ± 0.07	0.55 ± 0.00	0.60 ± 0.02
1,03	496,4	[M+H]+	LPC	16:0	16	1.47 ± 0.15	1.09 ± 0.02	0.74 ± 0.03	2.32 ± 0.13	0.97 ± 0.02	1.00 ± 0.05
1,03	522,4	[M+H]+	LPC	18:1	16	1.92 ± 0.04	1.00 ± 0.04	0.61 ± 0.02	4.23 ± 0.10	2.09 ± 0.01	2.02 ± 0.12
1,41	524,5	[M+H]+	LPC	18:0	18	1.75 ± 0.05	1.25 ± 0.02	1.22 ± 0.07	1.56 ± 0.01	0.07 ± 0.02	0.97 ± 0.08
1,41	550,6	[M+H]+	LPC	20:1	18	0.50 ± 0.04	0.22 ± 0.002	0.21 ± 0.007	0.52 ± 0.04	0.29 ± 0.00	0.22 ± 0.013
2,6	657,6	[M+H]+	SM	29:0;O2	29	0.49 ± 0.04	*nd*	*nd*	*nd*	*nd*	*nd*
2,6	663,6	[M+H]+	SM	31:0;O2	30	0.09 ± 0.01	0.58 ± 0.02	0.71 ± 0.05	*nd*	*nd*	*nd*
3,13	776,6	[M+Na]+	PC	34:4	26	0.18 ± 0.02	0.28 ± 0.003	0.12 ± 0.007	0.49 ± 0.06	0.30 ± 0.02	0.27 ± 0.005
3,34	685,7	[M+H]+	SM	33:3;O2	27	3.38 ± 0.08	0.57 ± 0.06	0.35 ± 0.02	0.94 ± 0.04	0.78 ± 0.03	0.90 ± 0.07
3,51	687,7	[M+H]+	SM	33:2;O2	29	3.36 ± 0.14	*nd*	*nd*	*nd*	*nd*	*nd*
3,51	703,7	[M+H]+	SM	34:1;O2	32	0.70 ± 0.04	3.48 ± 0.02	4.21 ± 0.17	0.24 ± 0.02	4.44 ± 0.10	4.57 ± 0.22
3,73	678,6	[M+H]+	PC	28:0	28	2.01 ± 0.04	1.82 ± 0.04	1.80 ± 0.01	2.53 ± 0.28	0.76 ± 0.02	0.70 ± 0.02
3,97	704,6	[M+H]+	PC	30:1	28	4.43 ± 0.40	4.43 ± 0.02	5.22 ± 0.11	1.26 ± 0.06	1.36 ± 0.04	1.23 ± 0.10
4,13	730,7	[M+H]+	PC	32:2	28	4.46 ± 0.19	5.60 ± 0.06	5.35 ± 0.07	*nd*	*nd*	*nd*
4,13	756,6	[M+H]+	PC	34:3	28	0.32 ± 0.02	2.68 ± 0.02	2.29 ± 0.05	*nd*	*nd*	*nd*
4,62	706,6	[M+H]+	PC	30:0	30	4.37 ± 0.12	3.38 ± 0.14	3.38 ± 0.06	4.86 ± 0.23	4.10 ± 0.16	4.30 ± 0.15
4,76	732,6	[M+H]+	PC	32:1	30	10.16 ± 0.13	8.22 ± 0.09	10.17 ± 0.64	10.59 ± 0.82	10.58 ± 0.47	10.16 ± 0.13
4,76	758,8	[M+H]+	PC	34:2	30	8.84 ± 0.29	8.10 ± 0.01	8.77 ± 0.37	8.37 ± 0.40	9.32 ± 0.33	9.71 ± 0.01
5,04	784,7	[M+H]+	PC	36:3	30	1.55 ± 0.03	6.88 ± 0.10	6.26 ± 0.20	4.45 ± 0.22	4.71 ± 0.07	5.78 ± 0.27
5,26	810,7	[M+H]+	PC	38:4	30	3.21 ± 0.17	3.38 ± 0.10	2.67 ± 0.03	0.77 ± 0.02	2.01 ± 0.05	1.42 ± 0.09
5,26	836,7	[M+H]+	PC	40:5	30	0.37 ± 0.01	1.10 ± 0.01	0.43 ± 0.03	*nd*	*nd*	*nd*
5,42	734,6	[M+H]+	PC	32:0	32	2.77 ± 0.11	2.69 ± 0.05	3.09 ± 0.04	2.30 ± 0.22	1.92 ± 0.03	2.16 ± 0.11
5,42	760,6	[M+H]+	PC	34:1	32	8.08 ± 0.05	7.61 ± 0.12	8.70 ± 0.21	13.52 ± 0.71	13.13 ± 0.58	12.87 ± 0.48
5,42	786,7	[M+H]+	PC	36:2	32	11.20 ± 0.36	7.19 ± 0.31	8.07 ± 0.33	13.35 ± 0.82	10.90 ± 0.17	11.26 ± 0.49
6,39	720,7	[M+H]+	PC	31:0	31	1.21 ± 0.07	1.93 ± 0.13	1.40 ± 0.09	2.04 ± 0.10	1.68 ± 0.01	2.64 ± 0.18
6,39	746,7	[M+H]+	PC	33:1	31	4.38 ± 0.18	6.04 ± 0.06	5.86 ± 0.20	6.30 ± 0.10	9.23 ± 0.16	7.68 ± 0.36
6,39	762,6	[M+H]+	PC	34:0	34	1.69 ± 0.19	2.38 ± 0.03	6.38 ± 0.28	1.27 ± 0.02	0.94 ± 0.03	1.03 ± 0.04
6,39	788,7	[M+H]+	PC	36:1	34	8.08 ± 0.53	6.34 ± 0.06	3.09 ± 0.28	10.17 ± 0.62	9.16 ± 0.25	8.55 ± 0.24
6,39	814,7	[M+H]+	PC	38:2	34	1.60 ± 0.08	3.72 ± 0.09	1.38 ± 0.01	1.81 ± 0.25	4.22 ± 0.03	4.55 ± 0.03
7,22	774,6	[M+H]+	PC	35:1	33	0.80 ± 0.04	1.73 ± 0.08	1.18 ± 0.01	*nd*	*nd*	*nd*
7,22	813,8	[M+H]+	SM	42:2;O2	38	4.91 ± 0.37	4.44 ± 0.01	3.90 ± 0.05	2.63 ± 0.14	2.96 ± 0.06	3.06 ± 0.02
7,62	816,7	[M+H]+	PC	38:1	36	0.40 ± 0.05	0.37 ± 0.03	0.54 ± 0.03	0.46 ± 0.04	1.00 ± 0.01	0.98 ± 0.01
7,62	842,7	[M+H]+	PC	40:2	36	*nd*	*nd*	*nd*	0.79 ± 0.05	0.53 ± 0.00	0.54 ± 0.01

Note: *nd*, not detected.

Table S3. List of lysophosphocholine (LPC), phoshocholine (PC), and sphingomyelin (SM) detected in SH-SY5Y and SU-DIPG-36 cell lines untreated and treated with **ONC201** and **26** (DA29). Abbreviations: RT (min), retention time; *m/z*, mass/charge ratio; CN:DB, carbon number and double bond; PN: partition number. Lipid amounts were expressed in area % ± standard deviation. UNT=Untreated.

6. Supplementary Table S4

RT (min)	*m/z*	Ion Type	Class	CN:DB	PN	SU-DIPG-36			SH-SY5Y		
						UNT	**ONC 201**	**26**	UNT	**ONC 201**	**26**
9.67	844.6	$[M+NH4]^+$	TG	50:4	42	0.41 ± 0.01	1.49 ± 0.05	1.06 ± 0.09	1.10 ± 0.09	0.60 ± 0.00	0.59 ± 0.01
9.67	870.7	$[M+NH4]^+$	TG	52:5	42	0.09 ± 0.00	- ± -	- ± -	1.04 ± 0.02	- ± -	- ± -
9.97	794.8	$[M+NH4]^+$	TG	46:1	44	2.27 ± 0.16	5.24 ± 0.33	4.67 ± 0.34	1.78 ± 0.09	3.49 ± 0.04	3.31 ± 0.02
9.97	820.8	$[M+NH4]^+$	TG	48:2	44	2.15 ± 0.37	7.21 ± 0.33	8.82 ± 0.41	2.21 ± 0.11	5.43 ± 0.17	4.50 ± 0.07
9.97	846.8	$[M+NH4]^+$	TG	50:3	44	1.94 ± 0.23	5.20 ± 0.11	6.41 ± 0.05	1.12 ± 0.06	2.67 ± 0.05	2.05 ± 0.07
9.97	872.9	$[M+NH4]^+$	TG	52:4	44	0.73 ± 0.07	3.28 ± 0.16	1.91 ± 0.16	0.77 ± 0.06	1.26 ± 0.02	1.29 ± 0.05
11.00	796.9	$[M+NH4]^+$	TG	46:0	46	1.90 ± 0.13	2.87 ± 0.09	1.97 ± 0.16	2.34 ± 0.20	1.62 ± 0.04	1.91 ± 0.03
11.00	822.9	$[M+NH4]^+$	TG	48:1	46	5.68 ± 0.53	6.40 ± 0.08	7.02 ± 0.17	6.56 ± 0.39	6.86 ± 0.09	6.87 ± 0.19
11.00	848.9	$[M+NH4]^+$	TG	50:2	46	5.67 ± 0.53	8.87 ± 0.13	8.64 ± 0.38	8.49 ± 0.68	9.85 ± 0.02	10.39 ± 0.42
11.00	874.9	$[M+NH4]^+$	TG	52:3	46	1.40 ± 0.13	9.26 ± 0.23	8.55 ± 0.31	5.73 ± 0.21	6.52 ± 0.08	6.95 ± 0.40
11.00	900.7	$[M+NH4]^+$	TG	54:4	46	0.94 ± 0.13	3.91 ± 0.19	4.14 ± 0.25	1.76 ± 0.04	1.60 ± 0.06	2.13 ± 0.07
12.25	850.9	$[M+NH4]^+$	TG	50:1	48	4.45 ± 0.54	6.24 ± 0.11	7.45 ± 0.11	12.30 ± 0.12	10.01 ± 0.14	9.43 ± 0.15
12.25	876.9	$[M+NH4]^+$	TG	52:2	48	11.13 ± 0.33	13.64 ± 0.05	13.75 ± 0.24	15.78 ± 0.76	14.04 ± 0.05	13.90 ± 0.11
12.25	902.9	$[M+NH4]^+$	TG	54:3	48	19.37 ± 1.14	12.33 ± 0.62	13.78 ± 0.54	11.64 ± 0.51	12.30 ± 0.79	11.59 ± 0.19
13.99	878.9	$[M+NH4]^+$	TG	52:1	50	13.49 ± 0.62	3.84 ± 0.11	3.50 ± 0.17	10.76 ± 0.58	8.20 ± 0.22	8.04 ± 0.59
13.99	904.8	$[M+NH4]^+$	TG	54:2	50	17.60 ± 0.93	6.19 ± 0.17	5.19 ± 0.10	9.88 ± 0.35	8.95 ± 0.28	10.41 ± 0.66
13.99	930.9	$[M+NH4]^+$	TG	56:3	50	7.17 ± 0.36	2.56 ± 0.08	1.95 ± 0.11	2.92 ± 0.05	3.89 ± 0.03	4.07 ± 0.17
15.14	906.8	$[M+NH4]^+$	TG	54:1	52	3.62 ± 0.29	1.48 ± 0.02	1.19 ± 0.09	3.82 ± 0.07	2.71 ± 0.04	2.58 ± 0.11

Table S4. List of triglycerides (TGs) detected in SH-SY5Y and SU-DIPG-36 cell lines untreated and treated with **ONC201** and **26** (DA29). Abbreviations: RT (min), retention time; *m/z*, mass/charge ratio; CN:DB, carbon number and double bond; PN: partition number. Lipid amounts were expressed in area % ± standard deviation. UNT= Untreated.

7. Supplementary Table S5

	SU-DIPG-36		SH-SY5Y	
Lipid	**ONC201**	**26** (DA29)	**ONC201**	**26** (DA29)
LPC 14:0	↑	↓	↓	*ns*
LPC 16:1	*ns*	↑	↓	↓
LPC 16:0	↓	↓	↓	↓
LPC 18:1	↓	↓	↓	↓
LPC 18:0	↓	↓	↓	↓
LPC 20:1	↓	↓	↓	↓
SM 29:0;O2	↓	↓	*nd*	*nd*
SM 31:0;O2	↑	↑	*nd*	*nd*
PC 34:4	↑	*ns*	↓	↓
SM 33:3;O2	↓	↓	↓	*ns*
SM 33:2;O2	↓	↓	*nd*	*nd*
SM 34:1;O2	↑	↑	↑	↑
PC 28:0	↓	↓	↓	↓
PC 30:1	*ns*	↑	*ns*	*ns*
PC 32:2	↑	↑	*nd*	*nd*
PC 34:3	↑	↑	*nd*	*nd*
PC 30:0	↓	↓	↓	*ns*
PC 32:1	↓	*ns*	*ns*	*ns*
PC 34:2	↓	*ns*	↑	↑
PC 36:3	↑	↑	*ns*	↑
PC 38:4	*ns*	↓	↑	↑
PC 40:5	↑	↑	*nd*	*nd*
PC 32:0	*ns*	↑	*ns*	*ns*
PC 34:1	↓	↑	*ns*	*ns*
PC 36:2	↓	↓	↓	↓
PC 31:0	↑	↑	↓	↑
PC 33:1	↑	↑	↑	↑
PC 34:0	↑	↑	↓	↓
PC 36:1	↓	↓	*ns*	*ns*
PC 38:2	↑	*ns*	↑	↑
PC 35:1	↑	↑	*nd*	*nd*
SM 42:2;O2	*ns*	↓	↑	↑
PC 38:1	↑	↑	↑	↑
PC 40:2	*nd*	*nd*	↓	↓

Table S5. Choline-containing lipids identified in the SU-DIPG-36 and SH-SY5Y cell lines and their relative trends upon 24 h treatment with **ONC201** and **26** (DA29). Legend: ↑, significant increase; ↓, significant decrease; *ns*, not significant; *nd*, not detected.

8. Supplementary Table S6

	SU-DIPG-36		SH-SY5Y	
Lipid	**ONC201**	**26** (DA29)	**ONC201**	**26** (DA29)
TG 50:4	↑	↑	↓	↓
TG 52:5	↓	↓	↓	↓
TG 46:1	↑	↑	↑	↑
TG 48:2	↑	↑	↑	↑
TG 50:3	↑	↑	↑	↑
TG 52:4	↑	↑	↑	↑
TG 46:0	↑	*ns*	↓	*ns*
TG 48:1	*ns*	↑	*ns*	*ns*
TG 50:2	↑	↑	↑	↑
TG 52:3	↑	↑	↑	↑
TG 54:4	↑	↑	*ns*	*ns*
TG 50:1	↑	↑	↓	↓
TG 52:2	↑	↑	↓	↓
TG 54:3	↓	↓	*ns*	*ns*
TG 52:1	↓	↓	↓	↓
TG 54:2	↓	↓	↓	*ns*
TG 56:3	↓	↓	↑	↑
TG 54:1	↓	↓	↓	↓

Table S6. Triacylglycerols (TG) identified in SU-DIPG-36 and SH-SY5Y cell lines and their relative trends upon 24 h treatment with **ONC201** and **26** (DA29). Legend: ↑, significant increase; ↓, significant decrease; *ns*, not significant; *nd*, not detected.

9. Supplementary Figure S1

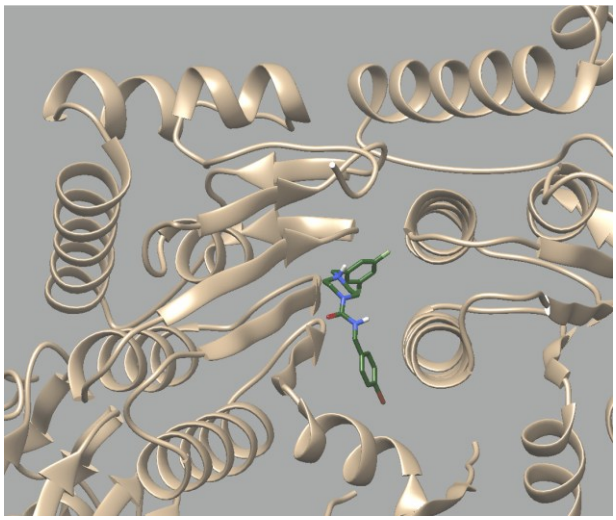

ZK53

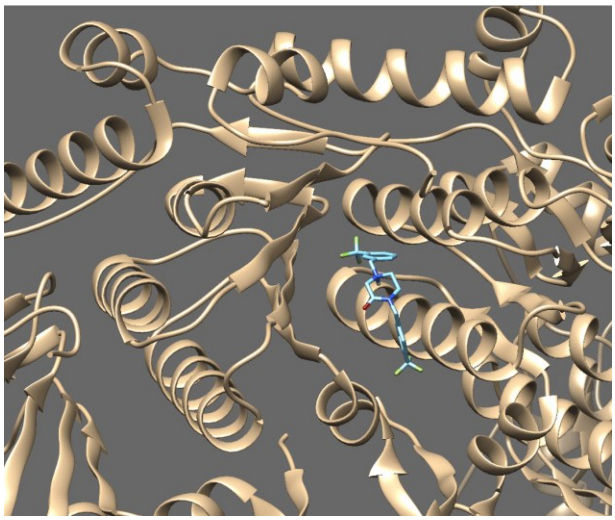

26 (DA29)

Candidate	Glob-Prod	Glob-Sum	Distance	H	N1	DRY	O
26 (DA29)	0.71519	2.66693	9.37175	0.975046	0	1.61296	0.22648
ZK53	0.568031	2.32319	8.3225	0.961466	0.1117	1.53997	0.214764

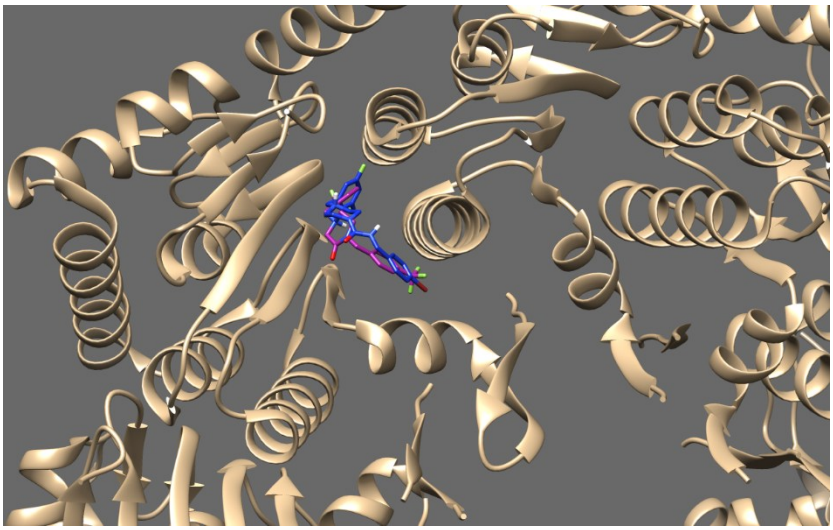

Alignment of the **ZK53** and **26** (DA29) poses with the best binding energy. **ZK53** is in bleu, **26** (DA29) is in purple.

FLAP analysis shows that **26** (DA29) achieves higher Glob-Prod and Glob-Sum scores than **ZK53**, reflecting a better field overlap. Both compounds share similar hydrogen-bonding contributions, but **26** (DA29) exhibits stronger hydrophobic interactions and slightly higher oxygen-based contributions, supporting its stronger binding profile. From the FLAP screening, **26** (DA29) occupies a lateral position within the pocket, comparable to **ZK53**. The 2D poses indicate highly similar interaction areas, with **26** (DA29) showing an increase in donor/acceptor hydrogen-bond regions. Both ligands interact with W146 and Y118 through π–π and CH–π contacts, while **26** (DA29) additionally engages V145 *via* hydrogen bonding. The two CF_3 groups of **26** (DA29) expand the interaction surface, enhancing binding (Data not shown).

Molecular docking with AutoDock Vina confirmed these findings: **26** (DA29) displayed a binding energy of −10.3 kcal/mol compared with −9.3 kcal/mol for **ZK53**, consistent with the stronger interaction profile predicted by FLAP. Computational studies were performed using FLAP (v2.2.2) in structure-based virtual screening mode. Molecular Interaction Fields (MIFs) were calculated with the GRID algorithm on the crystal structure of *h*ClpP in complex with **ZK53** (PDBID: 8HGK, 1.90 Å). Docking validation was conducted with AutoDock Vina (via UCSF Chimera) using grid boxes defined from the FLAP-identified pocket and visualized with PyMOL.

10. Supplementary Figure S2

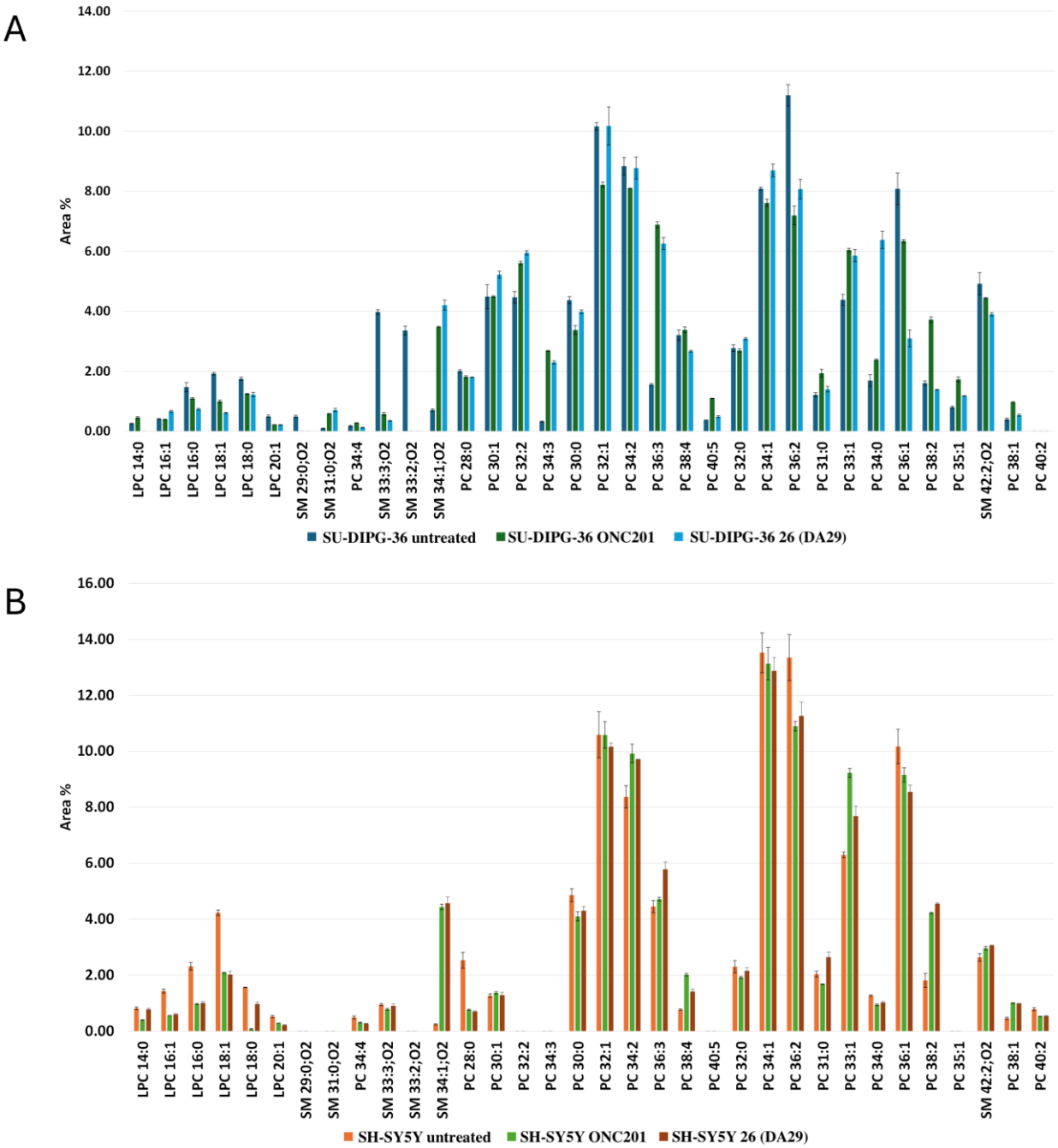

Figure S2. Histograms related to the percentage content of choline-containing lipids (LPCs, PCs and SMs), reported according to increasing retention time for SU-DIPG-36 (A) and SH-SY5Y (B) cells untreated and treated with **ONC201** and **26** (DA29). For each identified species, the error bars indicate the standard deviation.

11. Supplementary Figure S3

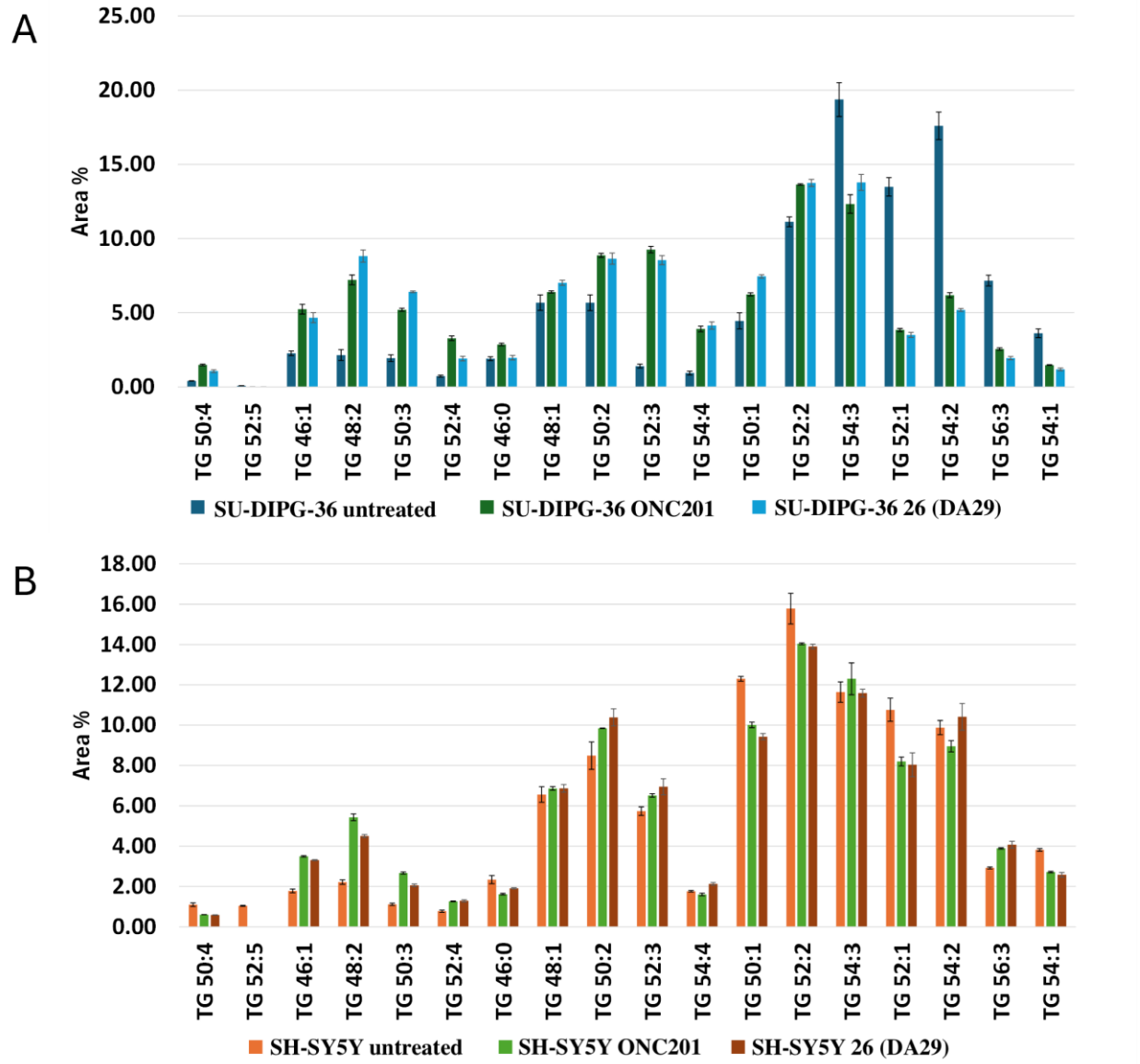

Figure S3. Histograms related to the percentage content of TGs, reported according to increasing retention time for SU-DIPG-36 (A) and SH-SY5Y (B) cells untreated and treated with **ONC201** and **26** (DA29). For each identified species, the error bars indicate the standard deviation.